

The Spectra of T Dwarfs I: Near-Infrared Data and Spectral Classification

Adam J. Burgasser¹, J. Davy Kirkpatrick², Michael E. Brown³, I. Neill Reid⁴, Adam Burrows⁵, James Liebert⁵, Keith Matthews¹, John E. Gizis², Conard C. Dahn⁶, David G. Monet⁶, Roc M. Cutri², and Michael F. Skrutskie⁷

ABSTRACT

We present near-infrared spectra for a sample of T dwarfs, including eleven new discoveries made using the Two Micron All Sky Survey. These objects are distinguished from warmer (L-type) brown dwarfs by the presence of methane absorption bands in the 1–2.5 μm spectral region. A first attempt at a near-infrared classification scheme for T dwarfs is made, based on the strengths of CH_4 and H_2O bands and the shapes of the 1.25, 1.6, and 2.1 μm flux peaks. Subtypes T1 V through T8 V are defined, and spectral indices useful for classification are presented. The subclasses appear to follow a decreasing T_{eff} scale, based on the evolution of CH_4 and H_2O bands and the properties of L and T dwarfs with known distances. However, we speculate that this scale is not linear with spectral type for cool dwarfs, due to the settling of dust layers below the photosphere and subsequent rapid evolution of spectral morphology around $T_{\text{eff}} \sim 1300\text{--}1500$ K. Similarities in near-infrared colors and continuity of spectral features suggest that the gap between the latest L dwarfs and earliest T dwarfs has been nearly bridged. This argument is strengthened by the possible role of CH_4 as a minor absorber shaping the K-band spectra of the latest L dwarfs. Finally, we discuss one peculiar T dwarf, 2MASS 0937+2931, which has very blue near-infrared colors ($J\text{--}K_s = -0.89 \pm 0.24$) due to suppression of the 2.1 μm peak. The feature is likely caused by enhanced collision-induced H_2 absorption in a high pressure or low metallicity photosphere.

¹Division of Physics, Mathematics, and Astronomy, M/S 103-33, California Institute of Technology, Pasadena, CA 91125; diver@its.caltech.edu, kym@caltech.edu

²Infrared Processing and Analysis Center, M/S 100-22, California Institute of Technology, Pasadena, CA 91125; davy@ipac.caltech.edu, gizis@ipac.caltech.edu, roc@ipac.caltech.edu

³Division of Geological and Planetary Sciences, M/S 105-21, California Institute of Technology, Pasadena, California 91125; mbrown@gps.caltech.edu

⁴Space Telescope Science Institute, 3700 San Martin Drive, Baltimore, MD 21218; inr@stsci.edu; also Dept. of Physics & Astronomy, University of Pennsylvania, 209 S. 33rd Street, Philadelphia, PA 19104-6396

⁵Steward Observatory, University of Arizona, Tucson, AZ 85721; burrows@jupiter.as.arizona.edu, liebert@as.arizona.edu

⁶U.S. Naval Observatory, P.O. Box 1149, Flagstaff, AZ 86002; dahn@nofs.navy.mil, dgm@nofs.navy.mil

⁷Five College Astronomy Department, Department of Physics and Astronomy, University of Massachusetts, Amherst, MA 01003; skrutski@north.astro.umass.edu

Subject headings: infrared: stars — stars: fundamental parameters — stars: low mass, brown dwarfs

1. Introduction

Classification is an important first step in the characterization of any astronomical population. It enables one to study the global properties of a group of similar objects and generalize to larger, and perhaps undetected, members. A fundamental attribute of astronomical classification is that it is based on observations; i.e., the way objects appear morphologically, photometrically, or spectroscopically. Stellar spectral classification has been in practice for nearly 150 years, and calibration of spectral classes to temperature and luminosity scales has provided crucial insight into the internal physics of stars, their history and evolution, and the properties of the Galaxy and extragalactic systems.

The stellar sequence of Morgan, Keenan, & Kellman (1943), the most widely accepted classification scheme, originates from the temperature-based sequence first used in the Henry Draper catalog (Pickering 1890), and luminosity discriminants initially identified by Maury & Pickering (1897). It extends the main sequence from hot O-type stars to cool M dwarfs, the latter of which until recently were the coolest and faintest stars known. With the advent of more sensitive optical and near-infrared detectors and large-scale surveys, including the Two Micron All Sky Survey (Skrutskie et al. 1997, hereafter 2MASS), the Sloan Digital Sky Survey (York et al. 2000, hereafter SDSS), and the Deep Near-Infrared Survey of the Southern Sky (Epchtein et al. 1997, hereafter DENIS), cooler stars and brown dwarfs have now been identified. As a result, two new spectral classes have been introduced, the L (Kirkpatrick et al. 1999; Martín et al. 1999) and T (Kirkpatrick et al. 1999) classes, which are extensions of the main stellar sequence into the brown dwarf regime.

The L spectral class is comprised of a mix of stars and brown dwarfs, characterized in the red optical (6300–10100 Å) by weakening bands of TiO and VO (dominant features in M dwarfs); strengthening bands of FeH, CrH, and H₂O; and strengthening lines of the alkali metals Na I, K I, Cs I, and Rb I (Kirkpatrick et al. 1999; Martín et al. 1999). The near-infrared spectra of these objects are similar to those of M dwarfs, dominated by H₂O and CO bands, but are redder ($1.3 \lesssim J-K_s \lesssim 2.1$), a characteristic attributed to warm photospheric dust (Tsuji, Ohnaka, & Aoki 1996a). L dwarfs cover an effective temperature (T_{eff}) range from 2000–2200 K down to ~ 1300 –1700 K (Kirkpatrick et al. 1999, 2000; Basri et al. 2000; Leggett et al. 2001), corresponding to luminosities $L \sim 4 \times 10^{-4}$ to $3 \times 10^{-5} L_{\odot}$ (Burrows et al. 1997). Well over one hundred of these objects have now been identified in the field (Delfosse et al. 1997; Ruiz, Leggett, & Allard 1997; Wolf et al. 1998; Kirkpatrick et al. 1999, 2000; Martín et al. 1999; Reid et al. 2000; Fan et al. 2000; Gizis et al. 2000), in stellar clusters (Martín et al. 1998; Zapatero Osorio et al. 1999, 2000), and as companions to nearby stars (Becklin & Zuckerman 1988; Rebolo et al. 1998; Goldman et al. 1999; Kirkpatrick et al. 2001a; Gizis, Kirkpatrick, & Wilson 2001a; Wilson et al. 2001b). Classification schemes for L dwarfs in the red optical have been defined by Kirkpatrick et al. (1999) and Martín et al. (1999).

The T spectral class is comprised of brown dwarfs that exhibit CH_4 absorption bands between 1.0 and 2.2 μm . The presence of these bands, broad H_2O features, and collision-induced (CIA) H_2 absorption radically alter the spectral energy distributions of T dwarfs, and near-infrared colors become increasingly blue ($J-K_s \sim 0$) as compared to L dwarfs. These distinctions led Kirkpatrick et al. (1999) to propose a second class, which at that time was solely occupied by the first unequivocal brown dwarf, Gliese 229B (Nakajima et al. 1995; Oppenheimer et al. 1995). Recently, a number of objects similar to Gliese 229B have been discovered by SDSS (Strauss et al. 1999; Tsvetanov et al. 2000; Leggett et al. 2000; Geballe et al. 2001b), 2MASS (Burgasser et al. 1999, 2000a,b), and the New Technology Telescope Deep Field (Cuby et al. 1999). These objects exhibit the same CH_4 and H_2O bands seen in Gliese 229B, but of differing strengths, suggesting that near-infrared spectra can be used to derive a T dwarf classification scheme (Burgasser et al. 1999; Leggett et al. 2000).

In this paper, we make a first attempt to define such a scheme based on the strengths of near-infrared CH_4 and H_2O absorption bands and colors, using spectral data obtained for newly discovered and previously known T dwarfs. In §2, we summarize our search for T dwarfs using the 2MASS database. In §3, we discuss near-infrared spectroscopy acquired for candidate and known T dwarfs, and describe features observed in these data. Eleven new T dwarfs identified in the 2MASS search are presented in §4, and a rough determination of the T dwarf space density from this search are compared to estimates from other samples. In §5, we use the near-infrared spectral data, along with data obtained from the literature, to establish a near-infrared classification scheme for T dwarfs. We also introduce a suite of spectral indices useful for subtyping. The properties of these T subclasses are discussed in §6, in which we speculate on the effective temperature scale of these objects based on their atmospheric evolution. The convergence of the L and T classes is addressed in §7, based in part on the increasing importance of CH_4 absorption in shaping the spectra of late-type L dwarfs, including the possible presence of weak CH_4 features in the K-band spectrum of the L7 V double DENIS 0205-1159AB (Delfosse et al. 1997). In §8, we analyze our only peculiar T dwarf, 2MASS 0937+2931, whose K-band flux is highly suppressed, possibly due to increased surface gravity or diminished metallicity. We summarize our results in §9.

2. The 2MASS T Dwarf Search

Since late 1998, we have been searching for T dwarfs using 2MASS point source data. This all-sky survey employs two automated 1.3m telescopes, at Mt. Hopkins (USA) and Cerro Tololo (Chile), each equipped with a three-channel camera capable of simultaneous observations in the J (1.25 μm), H (1.65 μm), and K_s (2.17 μm) near-infrared bands, down to nominal survey completeness limits of 15.8, 15.1, and 14.3, respectively. Survey operations, begun in 1997 June at Mt. Hopkins and 1998 March at Cerro Tololo, have recently been completed, and final catalogs are expected to be released in 2002. Additional information about 2MASS can be found in Cutri et al. (2001)⁸.

⁸<http://www.ipac.caltech.edu/2mass/releases/second/doc/explsup.html>.

2.1. Color Selection

Molecular absorption and cool effective temperatures cause the spectral energy distributions of T dwarfs to peak at J-band ($1.25 \mu\text{m}$), and near-infrared surveys such as 2MASS are particularly tuned to detecting these objects. Unfortunately, the near-infrared colors of T dwarfs ($J-K_s \sim 0$) make them difficult to distinguish from the overwhelming background of main sequence stars. Figure 1 illustrates this problem in a near-infrared color-color diagram. A typical sample of 2MASS point sources at moderate galactic latitude are plotted as small points; these objects were selected in a one degree radius around 18^h RA and $+40^\circ$ decl. ($|b^{II}| = 26^\circ$), with $J < 15.8$, $H < 15.1$, and $K_s < 14.3$. Their distribution is well traced by the giant and dwarf stellar tracks (solid lines) of Bessell & Brett (1988). Extending from the red branch of the dwarf track, comprised of late M dwarfs (Leggett, Allard, & Hauschildt 1998), are L dwarfs (triangles) identified in 2MASS data (Kirkpatrick et al. 1999, 2000). At the opposite end of the main sequence track lie Gliese 229B (Leggett et al. 1999, square) and the majority of T dwarfs (circles) identified by 2MASS and SDSS. These objects lie just below the densest region of near-infrared color space, occupied by early-type (O-G) stars. “Early” T dwarfs (also known as L/T transition objects; Leggett et al. 2000) lie at colors intermediate between the L dwarfs and Gliese 229B ($J-K_s \sim 1-1.5$) along the giant track. Objects with even bluer near-infrared colors ($J-K_s \sim 0.5-1$) are likely to be indistinguishable from the vast majority of background sources.

Nonetheless, it is possible to distinguish T dwarfs using optical/near-infrared colors. Low effective temperatures, broadened K I absorption (Burrows, Marley, & Sharp 2000; Liebert et al. 2000), and the possible presence of dust opacity (Tsuji, Ohnaka, & Aoki 1999), make T dwarfs extremely red in the optical, with $R-J \gtrsim 9$ (Matthews et al. 1996; Golimowski et al. 1998). Thus, T dwarfs similar to Gliese 229B with $J \gtrsim 10-12$ would have been easily missed in earlier optical sky surveys (e.g., POSS-II; Reid et al. 1991), which have typical limiting magnitudes of $R \lesssim 19-21$.

With these photometric properties in mind, we have constrained our search to the identification of the coolest T dwarfs which have sufficient H_2O and CH_4 absorption to push their near-infrared colors blueward of the majority of background stars ($J-K_s \lesssim 0.6$). We impose an additional optical/near-infrared color cut by rejecting candidate objects with optical counterparts (from the USNO-A2.0 catalog; Monet et al. 1998) within $5''$ of their 2MASS coordinates. We note that objects in the USNO-A2.0 catalog are required to be detected on both the R- and B-band plates, so that faint red objects visible only on the R-band plates (such as background M stars) generally remain on our candidate lists.

2.2. Search Samples

We have drawn three samples from the 2MASS point source catalogues in order to identify T dwarf candidates. The properties of these samples are summarized in Table 1. Initial candidates were required to have $|b^{II}| > 15^\circ$ in order to reduce source confusion near the Galactic plane, and

high source density regions around the Magellenic Clouds and 47 Tuc were excluded. Our main search sample, wdb0699, was drawn from the 2MASS working database in 1999 June, at a time when 2MASS sky coverage was approximately 45% complete. Figure 2 displays a spatial map of the 35280 initial candidates (points) from this sample, drawn from 16620 sq. deg. of 2MASS data. Grey boxes highlight areas surveyed by 2MASS at the time of candidate selection; data from 23510 scans were used in this sample, 12556 from the northern hemisphere and 10954 from the southern hemisphere. Note the increased source density close to the Galactic plane (dashed line), due to a higher concentration of (typically) faint background stars. Initial candidates were further required to have J- and H-band detections with $J < 16$, $J-H < 0.3$, and $H-K_s < 0.3$ (dashed lines in Figure 1). Five T dwarfs have already been published from this sample (Burgasser et al. 1999, 2000a,c)⁹.

The other search samples were drawn from the 2MASS Second Incremental Data Release (2MASS IDR2), and were used to investigate biases inherent to the color criteria of the primary wdb0699 sample. The rdb0400 sample reverses the $H-K_s$ color cut in order to identify faint sources without K_s detections, and thus artificially red $H-K_s$ colors. The rdb0600 sample extends to $J-H \leq 0.4$, with detections in all three bands and $J \leq 15$. This sample was used to identify T dwarfs with weaker CH_4 absorption, and was limited to the sky observable from the Southern Hemisphere during the months of June and July. Note that despite the stricter magnitude limit and smaller search area of this sample, a large number of initial candidates was identified, emphasizing the difficulties caused by the high background source density in this region of color space.

In order to refine our candidate selection, we improved upon our optical/near-infrared color cut by visually examining optical images of each candidate field. R-band imaging data $2'.5 \times 2'.5$ around each candidate coordinate, taken by the POSS-I, POSS-II, ESO/SERC, and AAO SES (Morgan et al. 1992) surveys, were obtained from the Canadian Astronomy Data Centre’s Digitized Sky Survey image server¹⁰. Multiple epochs of each field were examined whenever possible. Candidates with obvious optical counterparts at their 2MASS coordinates were summarily rejected, with the majority of these contaminants being close optical doubles blended in the USNO-A2.0 catalog. Objects identified as proper motion stars based on multiple-epoch optical data were also removed from candidate lists. Note that our criterion of no detection on the optical plates eliminates many of the biases inherent to visual selection, including variable plate quality and masking by bright star halos; these biases will tend to increase the number of false candidates in our candidate list, rather than eliminate bona fide T dwarfs. Nonetheless, 98.8% of the initial 2MASS-selected sources were eliminated in this manner, resulting in a substantially reduced candidate pool (Cut #2, Table 1, col. 6).

⁹A sixth T dwarf, 2MASS 1237+6526 (Burgasser et al. 1999) does not fall into this sample as it is too faint at J (16.03 ± 0.09).

¹⁰<http://cadwww.dao.nrc.ca/cadcbn/getdss>.

2.3. Follow-up Imaging Observations

Despite our optical and near-infrared color constraints, additional contaminants remain. Of primary concern are minor planets, which have near-infrared colors similar to T dwarfs (Sykes et al. 2000), as indicated by the hashed boxes in Figure 1. These objects are also absent in DSS images due to their motion. Known minor planets are flagged in the 2MASS database and subsequently eliminated from search samples; however, uncatalogued asteroids remain. To remove these objects from our candidate pool, we have conducted a near-infrared reimaging campaign, using the Near-Infrared Camera (Murphy et al. 1995, hereafter IRCam) mounted on the Palomar 60" Telescope, and the Cerro Tololo Inter-American Observatory (CTIO) Infrared Imager (CIRIM) and Ohio State InfraRed Imager/Spectrometer (Depoy et al. 1993, hereafter OSIRIS) mounted on the CTIO 1.5m Telescope¹¹. Observations of T candidates from our primary samples are summarized in Table 2. Second epoch imaging has eliminated nearly 80% of our Cut #2 T dwarf candidates with $J-K_s < 0.5$ (Table 1, col. 7). To date, 99%, 76%, and 54% of our wdb0699, rdb0400, and rdb0600 Cut #2 candidates have been reimaged, respectively.

Table 3 lists all of the candidates from the three samples present in the 2MASS IDR2 that were not flagged as minor planets but were absent in near-infrared reimaging. Using ephemerides generated by D. Tholen for the 2MASS project, we reexamined these objects for minor planet associations out to 25". A number of widely separated associations were made (Col. 8), including the major asteroids Pallas, Irene, and Niobe. The majority of these apparently missed associations occurred between 1998 September and 1998 November, and are likely due to slight errors in the ephemeris generation (D. Tholen, priv. comm.). This problem is currently being addressed and will be eliminated in the final release catalog; however, users of the 2MASS IDR2 should be aware of these identifications.

Determining the nature of our unconfirmed candidates can be done by investigating their spatial distribution. Figure 3 shows the ecliptic latitude distribution of 144 unconfirmed targets from our wdb0699 sample present in the 2MASS IDR2 and not associated with a known asteroid in Table 3. We compared this to the distribution of 288 flagged minor planets in the 2MASS IDR2 having the same color and magnitude properties as the wdb0699 sample, plus 25 missed associations with the same constraints. Both populations peak near the ecliptic plane, and it is likely that the vast majority of our unconfirmed candidates are probably uncatalogued minor planets. The distribution of the unconfirmed candidates is distinctly broader, however. We do not rule out that a few of these transient sources may be faint variable stars, infrared counterparts to bursting sources, or, in at least one confirmed case, supernovae¹².

Additional imaging observations were made using the Palomar 60" CCD Camera with a Gunn

¹¹Some additional observations were made using the Keck 10m Near Infrared Camera (Matthews & Soifer 1994) and Hale 5m D78 near-infrared camera.

¹²2MASSI J0101271-073636 is the near-infrared counterpart to SN 1998DN (Cao 1998).

r broad band filter (Wade et al. 1979) over a series of runs extending from 1999 May through 2000 December. The purpose of these observations was to eliminate proper motion stars and background objects close to bright optical sources from our candidate pool. A total of 49 confirmed sources were rejected based on r-band detections. The typical limiting magnitudes of $r \sim 19$ –20 correspond to color limits of $r-J \lesssim 6$, equivalent to spectral types earlier than M6 V to M8 V (Kirkpatrick et al. 1999).

3. Near-Infrared Spectroscopic Observations

The final confirmation of a candidate object as a T dwarf was made through the identification of CH_4 absorption bands in 1–2.5 μm spectral data. Observations made using the Near Infrared Camera (Matthews & Soifer 1994, hereafter NIRC), mounted on the Keck I 10m, and a similar instrument, D78, mounted on the Palomar 5m Hale Telescope, are discussed in §§3.1 and 3.2; observations made using OSIRIS, mounted on the CTIO 4m Blanco Telescope, are discussed in §3.3. The features seen in these spectra are discussed in §3.4. Finally, the accuracy of the NIRC and OSIRIS datasets is examined in §3.5 by comparison with each other and to previously published data.

3.1. NIRC Spectra

The NIRC instrument is comprised of a 256×256 InSb array camera mounted on the f/25 Forward Cassegrain focus of the Keck I 10m Telescope. Filters and grisms permit low-resolution ($\lambda/\Delta\lambda \sim 60$ –120) spectroscopy from 1–2.5 μm in two settings: 1–1.6 μm , using the 150 lines mm^{-1} grating blazed at 1.7 μm and JH order blocking filter; and 1.4–2.5 μm , using the 120 lines mm^{-1} grating blazed at 2.1 μm and HK order blocking filter. Spectral resolutions on the $0''.15 \text{ pixel}^{-1}$ chip are 49 \AA pixel^{-1} and 59 \AA pixel^{-1} , respectively.

A log of observations of identified T dwarfs and known L dwarfs, taken over four nights, is given in Table 4a. Conditions on 1999 November 18 (UT) were clear with good seeing ($\sim 0''.4$); conditions on 2000 January 23–24 (UT) were also clear but windy, with poor seeing ranging from $0''.7$ to $1''.3$; finally, conditions on 2000 July 22 (UT) were plagued by heavy to light cirrus, although seeing was $0''.4$. Targets were initially acquired in imaging mode and placed into a $0''.53$ slit. Multiple sets of three exposures dithered $5''$ along the slit were made for each object at the JH and HK settings. F and G dwarf standards close to the target objects, chosen for their weak Hydrogen lines, were observed using the same instrumental setup. Finally, spectral dome flats were observed in order to calibrate pixel response.

Science images were initially divided by a median-combined, dark-subtracted, normalized dome flat image to correct for pixel-to-pixel spectral response variations, and bad pixels were removed by interpolation using a mask constructed from dark and flat field frames. These processed images were

pairwise subtracted to remove dark current and sky background, and curvature of the dispersion along the chip was corrected by tracing OH sky lines. Spectra were then optimally extracted using a smoothed weighting function. At each dispersion position, object and standard spectra were ratioed and then multiplied by a blackbody appropriate to the standard star (Tokunaga 2000). The resulting flux-calibrated spectra for each grism setting were then separately combined using a clipped average (rejecting 3σ outliers at each wavelength). Wavelength calibration was computed using coefficients listed in the NIRC instrument manual¹³.

Spectra from 1–1.6 μm and 1.4–2.5 μm were then combined and flux calibrated. First, we scaled the spectra by a multiplicative factor to match the overlap region from 1.4–1.6 μm . Then, using spectral data of Vega (Bergeron, Wesemael, & Beauchamp 1995) and 2MASS photometry, we calculated flux corrections by integrating the 2MASS filter response curves¹⁴ over calibrator and object spectra, using the relation:

$$F_{obj}^{(corr)}(\lambda) = F_{obj}^{(uncorr)}(\lambda) \times 10^{-0.4m_b} \times \frac{\int F_{Vega}(\lambda') T_b(\lambda') d\lambda'}{\int F_{obj}^{(uncorr)}(\lambda') T_b(\lambda') d\lambda'}, \quad (1)$$

where $F_{obj}^{(corr)}(\lambda)$ and $F_{obj}^{(uncorr)}(\lambda)$ are the corrected and uncorrected flux densities of the object spectrum, $F_{Vega}(\lambda)$ is the flux density of Vega, m_b is the magnitude of the object through filter b , and $T_b(\lambda)$ is the transmission function. For this calibration, we chose to use $b = \text{J-band}$ magnitudes, as T dwarfs tend to be brightest at this band, reducing photometric errors.

Final NIRC spectra for confirmed T dwarfs are shown in Figure 4, along with data for the L6.5 V 2MASS 0920+3517 and the L7.5 V 2MASS 0825+2115 (Kirkpatrick et al. 2000). Spectra are normalized at their J-band peaks, offset (dotted line), and ordered by increasing 1.1 and 1.6 μm absorption. Major absorption bands of H_2O , CH_4 , CO , FeH (1.19, 1.21, and 1.237 μm), and CIA H_2 are indicated, as are atomic lines of K I (1.169, 1.177, 1.243, and 1.252 μm).

To test our flux calibration, we measured spectrophotometric colors for all of the calibrated spectra in the 2MASS near-infrared bands, and compared these to 2MASS photometric colors. Results are given in Table 5. Residuals ($\delta \equiv \text{photometry minus spectrophotometry}$) are typically on the order of 0.1 to 0.3 mag, slightly larger than the 2MASS photometric errors, with some colors discrepant by more than 0.6 mag. Nonetheless, the mean of these residuals, $\langle \delta_{J-H} \rangle = -0.04 \pm 0.17$, $\langle \delta_{H-K_s} \rangle = -0.03 \pm 0.29$, and $\langle \delta_{J-K_s} \rangle = -0.06 \pm 0.30$, imply overall consistency in the relative calibration. Significant color differences may be due to the effects of cirrus during our 2000 July 22 observations (affecting data for 2MASS 1553+1532, 2MASS 2254+3123, and 2MASS 2339+1352), or possibly low signal-to-noise photometry of objects barely detected by 2MASS at K_s (e.g., 2MASS 0937+2931). Regardless, the flux calibration appears to be adequate for the characterization of gross spectral morphology.

¹³<http://www2.keck.hawaii.edu:3636/realpublic/inst/nirc/manual/Manual.html>.

¹⁴For 2MASS filter response functions, see http://www.ipac.caltech.edu/2mass/releases/second/doc/sec3_1b1.html.

3.2. D78 Spectra

Additional low-resolution observations were made on 2001 January 4-5 (UT) using the D78 near-infrared camera, mounted at the f/70 Cassegrain focus of the Palomar 5m Hale Telescope. This instrument is similar in construction to NIRC, providing grism spectroscopy from 1–2.5 μm in three orders (3^{rd} , 4^{th} , and 5^{th}) with $\lambda/\Delta\lambda \sim 100$. Resolution on the $0''.125$ pixel $^{-1}$ chip ranges from 23 to 37 Å pixel $^{-1}$.

Weather was generally clear on 2001 January 4 with good seeing ($0''.7$); however conditions on 2001 January 5 were poor, with clouds frequently obscuring observations. Only one T dwarf was identified in these observations, 2MASS 0755+2212, observed on January 5. This object was acquired in imaging mode and placed into a $0''.71$ slit. Three exposures dithered $10''$ along the slit were obtained at each setting. Pixel response and flux calibrations at J- and H-bands were made using observations of the G0 V standard HD 4307 taken on January 4, which was smeared along the slit by driving the tip-tilt secondary with a 20 Hz, $40''$ (peak-to-peak amplitude) triangle wave. Corresponding sky frames were also obtained. Observations made at K-band were calibrated using observations of the G7 V HD 67767 (= ψ Cnc) obtained on January 5 in a similar fashion.

Science images at each grism setting were initially divided by the sky-subtracted standard observations, and then pairwise differenced to remove dark current and sky background. The resulting images were then shifted and coadded to boost signal-to-noise, after correcting for dispersion curvature along the slit. Spectra were then extracted from the combined images. The wavelength scale was computed using known dispersion coefficients calibrated to observations of the 1.2818 Pa β emission line in NGC 2392 (Rudy et al. 1992), obtained on January 5. Finally, spectral orders were multiplied by the appropriate blackbody and combined; no attempt was made to scale the individual orders or compute flux calibrations.

Figure 5 shows the reduced spectrum of 2MASS 0755+2212, normalized at the J-band peak; the poor observing conditions are evident in the significant amount of noise present in the data. Nonetheless, H₂O absorption is seen at 1.2, 1.35, and 1.9 μm , and CH₄ bandheads at 1.6 and 2.2 μm can be readily identified. 2MASS 0755+2212 was originally selected as a 2MASS T candidate in early 1999, but was initially rejected from the candidate list due to the presence of a faint and extended optical counterpart. Based on Keck imaging observations made with the Low Resolution Imaging Spectrograph (Oke et al. 1995), it appears that this counterpart is in fact a background galaxy coincident with the T dwarf.

3.3. OSIRIS Spectra

The OSIRIS instrument is a near-infrared imager/spectrometer mounted on the f/14.5 Cassegrain focus of the CTIO 4m Blanco Telescope. It is equipped with a 1024×1024 HgCdTe HAWAII array with 18.5 μm pixels, sampling the entire illuminated field. Use of the single diffraction grating

blazed at $6.6 \mu\text{m}$ with the $120 \text{ lines mm}^{-1}$ grating and $f/2.8$ camera provides simultaneous, cross-dispersed, moderate resolution ($\lambda/\Delta\lambda \sim 1200$) spectroscopy from $1.2\text{--}2.35 \mu\text{m}$ in four orders: J (3^{rd} and 4^{th}), H (5^{th}), and K (6^{th}). Resolution on the $0''.403 \text{ pixel}^{-1}$ chip ranges from 4.4 to $8.8 \text{ \AA pixel}^{-1}$.

Table 4b summarizes our OSIRIS observations. Data obtained during 1999 December 20-22 (UT) were taken in clear to hazy conditions, with seeing ranging from $0''.6$ to $1''.0$; observations made in 2000 July 15-19 (UT) were taken in conditions ranging from clear to cloudy, and seeing ranged from $0''.6$ to $1''.8$. Additional observations were also made during 1999 July 26-29 (UT), with preliminary results reported in Burgasser et al. (2000a); however, targets from this run were reobserved at later dates to higher signal-to-noise, and the early data are not included here. A total of 14 T dwarfs were observed using OSIRIS, along with a number of M and L dwarfs for comparison. Targets were acquired in imaging mode and placed into a $1''.2 \times 30''$ slit. Observations were made in sets of 5 exposures dithered $4\text{--}5''$ along the slit, with individual integrations ranging from 15 to 250 sec per exposure. A-type stars were observed near the target objects for flux calibration and telluric corrections. Spectral lamps reflected off of the 4m dome spot were observed each night for pixel response calibration.

Science images were initially trimmed to eliminate vignetted columns, divided by a median-combined, dark-subtracted flat field, and corrected for bad pixels by interpolation, using a mask created from flat-field and dark exposures. Images were then pairwise subtracted to eliminate sky background and dark current. Curvature of the dispersion lines was determined using standard star observations, and both standard and object spectra were optimally extracted using a smoothed weighting function. Spectra from each order were then scaled by a multiplicative factor and combined using a clipped average. Wavelength calibration was done using OH line identifications from Olivia & Origlia (1992). Telluric H_2O absorption was corrected using spectra of the standard star, and a flux correction was calculated by interpolating over hydrogen Paschen and Brackett lines and multiplying by the appropriate blackbody. Finally, the resulting flux-calibrated spectral orders were combined by first scaling each order by a multiplicative factor to match overlap regions (typically $1.29\text{--}1.31$, $1.53\text{--}1.57$, and $1.96\text{--}1.98 \mu\text{m}$), and then correcting the combined spectra to 2MASS H-band magnitudes (not J, due to the short wavelength cutoff) using Equation 1. Note that the overlap between the H- and K-band orders falls within the $1.9 \mu\text{m}$ H_2O band; because of this, we applied no scaling corrections between these two orders.

Resulting spectra for confirmed T dwarfs are shown in Figure 6, along with data for LHS 511AB (Luyten 1979, M4.5 V), HB 2124-4228 (Hawkins & Bessell 1988, M8.5 V), 2MASS 2224-0158 (Kirkpatrick et al. 2000, L4.5 V), and DENIS 0205-1159AB (Delfosse et al. 1997, L7 V). Spectra are normalized, offset, and ordered as in Figure 4. Bands of H_2O , CH_4 , CO, FeH, and CIA H_2 are indicated, as are lines of K I (1.25 and $1.52 \mu\text{m}$ doublets), Na I ($2.21 \mu\text{m}$ doublet), and Ca I (1.314 , 1.98 , and $2.26 \mu\text{m}$ triplets). The $1.52 \mu\text{m}$ K I doublet and Ca I lines, prominent in M dwarfs (Jones et al. 1994) are only detectable in the M4.5 V LHS 511AB. Regions of increased noise are due to telluric H_2O opacity; note, however, that higher-energy H_2O transitions originating from

the target objects extend well into the J, H, and K telluric windows.

3.4. Near-infrared Spectral Features

The spectra in Figures 4 and 6 show that H_2O and ultimately CH_4 absorption are the dominant features shaping the spectra of objects cooler than late M dwarfs. The H_2O bands centered at 1.15, 1.4, and 1.9 μm segregate the spectral energy distributions into distinct z-, J-, H-, and K-band peaks as early as L6.5 V, while the addition of CH_4 bands beginning at 1.05, 1.3, 1.6, and 2.2 μm further confine the emitted flux into narrow peaks centered at 1.08, 1.27, 1.59, and 2.07 μm . Note that CH_4 is necessary to produce the strong absorption at 1.15 μm , a feature also seen in the spectra of giant planets (Fink & Larson 1979). In addition, the gradually developing slope between the 1.27 μm peak and the 1.4 μm H_2O band is also caused by CH_4 at 1.3 μm .

In addition to H_2O and CH_4 absorptions, the K-band spectral region is shaped by 2.3 μm CO in M and L dwarfs, a feature that has been detected in the early T dwarfs as well (Leggett et al. 2000). The distinct bandheads seen in LHS 511AB strengthen through L4.5 V, but appear to weaken beyond this, as they are barely detectable in our spectrum of SDSS 1254-0122 (an early T dwarf). None of the 2MASS T dwarfs show any indications of CO absorption. The other important molecular absorber at K-band is CIA H_2 , which has no distinct bandhead but likely suppresses flux throughout the 2–2.5 μm region starting in the latest L dwarfs (see §7). With the presence of H_2O , CH_4 , CO, and CIA H_2 absorption features, the K-band peak undergoes a dramatic evolution. Starting from a flat slope with CO bandheads in mid-M dwarfs, the K-band becomes a plateau girded by CO and H_2O absorptions in the L dwarfs; it then develops from a double plateau with the dual presence of CH_4 and CO in the early SDSS T dwarfs to an increasingly suppressed and rounded hump centered at 2.11 μm in the earliest 2MASS T dwarfs; finally, we see a smooth triangular peak centered at 2.07 μm in the latest T dwarfs (those exhibiting the strongest CH_4 and H_2O absorption).

Finer features of FeH and K I have been identified in the J-band spectra of M and L dwarfs by McLean et al. (2000), and these features are also indicated in Figures 4 and 6. The resolution of the NIRC data is generally insufficient to resolve these lines, although the 1.25 μm K I doublet can be seen as a notch in the blue wing of the J-band peak of the T dwarf spectra. OSIRIS data can resolve this doublet, however. Figure 7 shows a close-up of the 1.19–1.34 μm spectral region for the OSIRIS data; spectra are normalized and offset as in Figure 6. The K I lines are present as early as M4.5 V, remain strong from the latest M dwarfs through most of the T dwarfs, but are weak in Gliese 570D. This behavior is mimicked in the evolution of the notch feature in the NIRC spectra. Note that the 1.2432 μm line is blended with an FeH feature at 1.237 μm in HB 2124-4228 and 2MASS 2224-0158. The 1.2522 μm line appears to be relatively stronger in the T dwarfs, an asymmetry noted by Leggett et al. (2001) in the L7 V DENIS 0205-1159AB. Lines of Na I (1.138, 1.141 μm) and Rb I (1.323 μm) noted by McLean et al. (2000) are likely present in the L dwarf spectra, but are weakened by overlying H_2O opacity; we do not see these features in our data.

Finally, we note that several weak absorption features are seen in the H-band peaks of our M and L dwarf spectra, near 1.58, 1.61, 1.63, and 1.67 μm . Reid et al. (2001) have also detected these features in their spectral data, suspecting that they may be due to an unidentified molecular absorber. The features are fairly close to both Brackett Hydrogen lines (1.5885, 1.6114, 1.6412, and 1.6811 μm), which are strong in the spectra of our A-type standards, and weak telluric absorptions. We believe that these features may be artifacts produced during our flux calibration due to imperfect interpolation over the Brackett lines (see §3.3), as they are not obviously present in the data prior to flux calibration. Recalibrating the data using later-type standards may help to elucidate the authenticity and origin of these weak features; however, their presence does not effect the analysis presented here.

3.5. Comparison of Data Sets

Data from NIRC and OSIRIS observations comprise our primary spectral sample. Because the instrumental setup, resolution, standards, and reduction procedures were slightly different for these two datasets, we have observed several objects with both instruments to identify any inherent biases. Figure 8 plots OSIRIS (light gray) and NIRC (black) data for 2MASS 2254+3123, 2MASS 0559-1404, 2MASS 2356-1553, 2MASS 0937+2931, 2MASS 1553+1532, and Gliese 570D. In general, wavelength and overall flux levels agree well, but there are some differences seen in the individual flux peaks. This is most striking at H- and K-bands, where the NIRC data are generally brighter, although differences can also be seen at J-band at the 10–15% level as well. Spectral data for 2MASS 0559-1404 are the most discrepant, with NIRC observations as much as 35% brighter at K; there is also a difference in slope seen in the 1.6 μm CH_4 band. The discrepancies at K may be due to the difficulty in determining overlap between the OSIRIS H- and K-band spectral orders (see §3.3). A similar problem may be present in the spectrum of 2MASS 1553+1532. However, spectral differences generally do not exceed 10–15%, similar to the differences seen between the 2MASS photometry and NIRC spectrophotometry (§3.1).

Figure 9 shows OSIRIS and NIRC data (light gray) compared to data from the literature for DENIS 0205-1159AB (Leggett et al. 2001), SDSS 1254-0122 (Leggett et al. 2000), 2MASS 0559-1404 (Burgasser et al. 2000c), SDSS 1346-0031 (Tsvetanov et al. 2000), and SDSS 1624+0029 (Strauss et al. 1999). Again, overall wavelength calibration and flux levels appear to be consistent, and band morphologies are generally coincident. Most discrepant are data for 2MASS 0559-1404, which is roughly $\sim 50\%$ brighter at K-band in the NIRC spectrum (left panel). Data from Burgasser et al. (2000c) were obtained with the Palomar 60" Cornell-Massachusetts Slit Spectrograph (Wilson et al. 2001a); this instrument has no overlap between the H- and K-bands, and it is possible that the K-band segment of these data was improperly scaled, particularly given the overall agreement from 1–2 μm . OSIRIS data for 2MASS 0559-1404 match the Burgasser et al. (2000c) spectrum better at K (right panel), but not as well at H-band. The spectra of the other objects agree quite well with published results, and small offsets may simply be due to differences in resolution or signal-to-noise.

In general, we find that typical discrepancies do not exceed 10–15%, quite adequate for the task of spectral classification.

4. New T Dwarfs

Based on our spectroscopic results, we have identified eleven new T dwarfs in our 2MASS search samples. The photometric properties of these objects are summarized in Table 6, and $5' \times 5'$ images of each field in the optical (R-band) and near-infrared (J- and K_s -bands) are given in Figures 10a–d. Images are oriented with North up and East to the left. These discoveries span a much broader range of colors than previous detections, with $-0.89 \leq J-K_s \leq 0.45$, reflecting their significant spectral variations. Note, however, that none of these objects are as red as the Leggett et al. (2000) early T dwarfs, a consequence of our near-infrared color constraints.

Considerable follow-up remains for the rdb0400 and rdb0600 samples, but a large percentage of the wdb0699 candidates have been characterized through follow-up imaging and spectroscopy. In addition to 34 confirmed objects from this sample observed at r-band, 33 objects have had near-infrared spectroscopic data taken. The majority of these followed-up candidates (Table 1, Col. 8) appear to be faint background stars or unidentified proper motion stars, based on their r-J colors or spectral morphology. The remaining 26 candidates are mostly faint objects close to bright optical sources, and are likely to be background stars with compromised photometry. Follow-up of our best candidates from the wdb0699 sample is therefore nearly complete, and we can use this sample to make a rough estimate of the space density of T dwarfs with $J-K_s \lesssim 0.6$. With a total of 14 identified T dwarfs (Table 1, Col. 9), the wdb0699 sample yields an areal density of 8.4×10^{-4} T dwarfs deg^{-2} , or roughly one T dwarf for every 1200 deg^2 down to $J \sim 16$. This is nearly one-third the original estimate from Burgasser et al. (1999), and implies only 35 T dwarfs with $J-K_s \lesssim 0.6$ detectable by 2MASS over the whole sky. If we adopt a distance limit based on the absolute brightness of Gliese 229B (Leggett et al. 1999, $M_J = 15.51 \pm 0.09$) and our J-band magnitude limit, we derive a space density of $4.2 \times 10^{-3} \text{ pc}^{-3}$.

Our estimate can be compared to other T dwarf search samples with multiple detections. Tsvetanov et al. (2000) calculate a density of $5 \times 10^{-2} \text{ pc}^{-3}$ based on two detections in 130 deg^2 of SDSS data, with $z^* \lesssim 19.8$. The three early T dwarfs identified by Leggett et al. (2000) in 225 deg^2 of SDSS data yield a space density between 1.9×10^{-2} and $1.8 \times 10^{-3} \text{ pc}^{-3}$, the upper limit based on scaling the J-band magnitude of their faintest object (SDSS 0837-0000; $J_{\text{FTI}} = 16.90 \pm 0.05$) to Gliese 229B (which is likely to be intrinsically fainter at J-band), while the lower limit scales the faintest K-band detection to the L8 V Gliese 584C (Kirkpatrick et al. 2001a, $M_{K_s} = 12.89 \pm 0.09$). Our estimates are generally lower than those of SDSS, but without quantification of biases inherent to our sample (e.g., color selection, photometric completeness), we emphasize that our results are likely a lower limit to the true T dwarf space density. As a comparison, the L dwarf space density ranges from 2×10^{-3} to $8 \times 10^{-3} \text{ pc}^{-3}$, based on 2MASS (Kirkpatrick et al. 1999) and SDSS (Fan et al. 2000) search samples, respectively, scaled to absolute magnitudes from Kirkpatrick et al. (2000).

The low-mass stellar ($0.1\text{--}1.0\text{ M}_\odot$) density, on the other hand, is roughly $2\times 10^{-2}\text{ pc}^{-3}$ (Reid et al. 1999). Our T dwarf space density estimate applied to the mass function simulations of Reid et al. (1999) predicts a substellar mass function that goes as $\frac{dN}{dM} \propto M^{-1}$, consistent with results from various cluster surveys (Luhman et al. 2000).

Table 7 lists all of the 24 currently known T dwarfs¹⁵. 2MASS photometry is listed where available. Many more T dwarfs are expected to be found with the anticipated completion of the 2MASS and SDSS surveys.

5. Spectral Typing

The evolution of molecular features seen in Figures 4 and 6 suggest the makings of a classification scheme for T dwarfs. To do this, we have followed the philosophy of the MK system, basing our classification criteria exclusively on the observed spectral features, without presumption of the precise physical properties of these objects (i.e., T_{eff} , gravity, or metallicity). This is an important point, as models of cool brown dwarfs, although greatly improved over earlier work, do not yet adequately predict all of the features seen in T dwarf spectra (Leggett et al. 2001). It is, in our opinion, better to classify an object on its actual appearance, rather than on possibly incorrect physical interpretations.

5.1. Near-Infrared or Optical Classification?

A classification scheme for T dwarfs should be able to distinguish these objects from the warmer L dwarfs. One might expect to do this at red optical wavelengths, where both the Kirkpatrick et al. (1999) and Martín et al. (1999) L dwarf classification schemes are defined. Burgasser et al. (2001) and Kirkpatrick et al. (2001b) have shown that T dwarfs can be segregated from L dwarfs in this spectral regime, and features useful for classification have been identified. However, T dwarfs are exceedingly faint shortward of $1\text{ }\mu\text{m}$, ($i^*\text{--}J \gtrsim 7.5$; Leggett et al. 2000), and data are difficult to obtain using even the largest ground-based telescopes.

In the near-infrared, however, T dwarfs are significantly brighter, and large samples can be observed using only moderate-sized (4m class) facilities. Because of this utility, we advocate a T classification scheme based on $1\text{--}2.5\text{ }\mu\text{m}$ spectroscopy. Corresponding classification schemes for L dwarfs in this spectral regime have only recently been proposed, however. Preliminary efforts have been made by Tokunaga & Kobayashi (1999) using indices that measure H_2O and H_2 features at K-band. Reid et al. (2001) have mapped the Kirkpatrick et al. (1999) L dwarf scheme onto near-infrared spectra using the strengths of the 1.4 and $1.9\text{ }\mu\text{m}$ H_2O bands. Testi et al. (2001) find

¹⁵Additional T dwarfs identified by Geballe et al. (2001b, this volume) in SDSS data are not included here.

similar correlations using their own H_2O and color indices. Other near-infrared investigations are currently underway by McLean et al. (2001), Gizis et al. (2001b), and Wilson et al. (2001c).

In order to gauge how well our classification system segregates L and T dwarfs in the near-infrared, we have augmented our spectral sample with NIRC and OSIRIS observations of known M and L dwarfs. We have also included data for M, L, and T dwarfs obtained from the literature (Geballe et al. 1996; Strauss et al. 1999; Tsvetanov et al. 2000; Leggett et al. 2000, 2001; Reid et al. 2001, hereafter CGS4 data). Note that no attempt is made to define a near-infrared L classification scheme; our purpose is simply to examine the behavior of our T classification (in particular, spectral indices, §5.3) over a broader sample. We examine how L dwarf near-infrared schemes may carry into the T dwarf regime in §5.6.

5.2. Defining the Subtypes

The first step toward classification is to determine groupings, or subtypes. Numerous techniques for identifying spectral subtypes in the MK system have been proposed (Morgan 1950; Bailer-Jones 2001). We have chosen to define T subclasses by the following procedure: First, we visually compared the spectra, normalized at their J-band peaks, with OSIRIS and CGS4 data smoothed with a Gaussian filter to match the resolution of the NIRC data. These spectra were then sorted into a morphological order based on the strengths of the 1.6 and 2.2 μm CH_4 bands, the 1.15 μm $\text{H}_2\text{O}/\text{CH}_4$ band, and the overall appearance of the J, H, and K-band peaks, similar to the ordering used in Figures 4 and 6. The CH_4 absorption bands are expected to strengthen with decreasing T_{eff} (Burrows et al. 1997), so that a classification scheme based on these features should adequately represent an underlying temperature sequence. The spectra were then grouped into subtypes of similar morphology, with the number of subtypes chosen to evenly represent the spectral variations seen. This process was repeated until a consistent system developed, resulting in seven groups we have labeled T1 V, T2 V, T3 V, T5 V, T6 V, T7 V, and T8 V. Our two subtype omissions, T0 V and T4 V, are based on apparent gaps in the photometric colors and spectral morphologies of the currently known T dwarf population. The earliest T dwarf so far identified, SDSS 0837-0000, is considerably bluer in J- K_s color than the latest L8 dwarfs, suggesting the presence of an additional (earlier) subtype with weaker methane features. We have also omitted a class between the latest of the Sloan transition dwarfs, SDSS 1021-0304, and the reddest 2MASS T dwarf, 2MASS 2254+3123, again based on the significant near-infrared color differences, as well as substantial relative suppression of the H- and K-band peaks in the spectrum of the latter object. Note that all of the 2MASS discoveries fall exclusively in the last four subtypes, due to the color constraints discussed in §2.

Representative bright standards for each subtype were then chosen. Low resolution spectra of these standards are shown in Figure 11, along with data for the L7 V DENIS 0205-1159AB (Leggett et al. 2001). Spectra are normalized at their J-band peaks with zero point offsets indicated by dashed lines. Data from Leggett et al. (2000, 2001) have been degraded to NIRC resolution

using a Gaussian filter. The spectral properties of these subtypes are summarized in Table 8. The progressive strengthening of the H_2O and CH_4 bands throughout the sequence is readily apparent. Early types are distinguishable from L dwarfs by the presence of weak CH_4 absorption at 1.6 and 2.2 μm , the latter of which appears in conjunction with CO at 2.3 μm in types T1 V, T2 V, and T3 V. Other important features include the strengthening 1.15 μm $\text{H}_2\text{O}/\text{CH}_4$ band, weakening 1.25 μm K I doublets, suppression of H- and K-band flux relative to J (significant between T3 V and T5 V), and narrowing of the 1.08, 1.27, 1.59, and 2.07 μm peaks through T8 V. The K-band peak of the later subtypes evolves from a rounded hump centered at 2.11 μm (T5 V), to a sloped, asymmetric peak notched at 2.17 μm (T7 V), and finally into a sharper, symmetric peak centered at 2.07 μm (T8 V).

5.3. T Dwarf Spectral Indices

T dwarfs can be classified, to first order, by a simple visual comparison against the standard sequence plotted in Figure 11. A more quantitative approach is to use spectral indices, ratios of fluxes in spectral regions which measure specific morphological features, such as the CH_4 and H_2O bands and the changing appearance of the K-band peak. Based on the subtype properties listed in Table 8, we have defined a suite of spectral indices, listed in Table 9. For each index, flux regions were chosen to sample the feature of interest and a nearby pseudo-continuum point (typically the flux peaks at J, H, or K), and the mean of the data in these regions were ratioed. The H_2O , CH_4 , and CO indices measure the relative depths of their respective bands, while the color indices H/J, K/J, and K/H are approximate measures of color around the 1.25, 1.6, and 2.1 μm flux peaks. Both the 2.11/2.07 and K shape indices measure the change in the K-band peak, influenced by the molecular absorbers H_2O , CH_4 , CO, and CIA H_2 .

The behavior of these indices was examined for the T dwarf standards, and a subset of indices showing obvious trends were chosen for use in spectral typing. These include the H_2O -A, H_2O -B, CH_4 -A, CH_4 -B, and CH_4 -C band indices; the H/J and K/J color indices; and the 2.11/2.07 K-band ratio. Values of these indices measured for late-L (Kirkpatrick et al. 1999) and T dwarf standards are listed in Table 10. NIRC data were used to compute the standard ratios for types T5 V through T8 V, while CGS4 data were used for types L5 V through T3 V.

Using the standard values as benchmarks, we then computed spectral types for the remaining T dwarfs by directly comparing the individual indices. Tables 11a–c list the index values and corresponding subtypes derived from NIRC and D78, OSIRIS, and literature data, respectively. Only measurable indices are listed in each set; for example, the spectral limits of the OSIRIS and D78 data, and significant K-band noise, restrict the use of the H_2O -A, CH_4 -C, and 2.11/2.07 indices. We note that the CH_4 -C, H/J, and K/J indices appear to saturate in the latest subtype standards, obviating their use in distinguishing between types T7 V and T8 V; in addition, the 2.07/2.11 index shows a consistent trend only for types T3 V through T8 V.

Individual subtypes were then averaged into a decimal classification after rejecting the single highest and lowest values; these are listed in the last column of each table. Uncertainties were determined from the scatter of the index subtypes, which in no case exceeded ± 0.9 subclasses. Finally, the decimal classifications were rounded off to the nearest 0.5 subclass to produce the final subtypes listed in Table 7 (col. 2). In general, preference was given to classifications derived from NIRC and CGS4 data, as these samples were used to derive the standard ratios. Nonetheless, differences between the various datasets for common objects did not exceed ± 0.9 subclasses. Objects observed on multiple occasions by the same instrument showed no differences in their final spectral types, indicating that the classifications are robust (i.e., not changed by intrinsic variability in the source). Note that final subtypes for 2MASS 0755+2212 and NTTDF 1205-0744 are assigned tentative (uncertain) values due to the poor quality of their spectral data. Ignoring these objects, comparison between the datasets indicates that the derived subtypes have typical uncertainties of ± 0.5 subclasses.

5.4. Spectral Index Relations

The behavior of our derived spectral indices as compared to spectral type allows us to ascertain the usefulness of these indices for classification, while also probing the evolution of spectral features. Figures 12a–d plot these ratios for objects with types M4.5 V through T8 V, measured from the NIRC (diamonds), OSIRIS (triangles), and CGS4 (squares) datasets. Filled circles indicate spectral standard values; T spectral types are those listed in Table 7. Note that we have ended the L sequence in this (and subsequent) diagrams at L8 V; motivation for this choice is discussed in §7.

The H₂O indices (Figure 12a) are seen to decrease monotonically over the entire sequence, except for the H₂O-C index, which increases from T2 V to T8 V. Decreasing indices imply strengthening bands, which can be easily seen in the spectral data shown in Figures 4 and 6. The slopes are greater in the T dwarfs, reflecting either increased band contrast with the loss of higher-energy (and hence higher temperature) wing transitions; increased H₂O photospheric abundance with the formation of CH₄, via:



or increased transparency due to the settling of dust cloud layers (Ackerman & Marley 2001; Burrows et al. 2001). The sharper increase in slope for the H₂O-A index is due to the additional contribution of CH₄ absorption in this feature. Note that the H₂O-C index has a great deal of scatter in the T dwarf regime, and its behavior is likely affected by CH₄ and CIA H₂ absorption at K-band.

The CH₄ indices (Figure 12b) are generally flat for most of the M and L dwarfs earlier than type L5 V, but rapidly decrease starting around L5 V to T1 V. Note that this behavior makes the CH₄ indices particularly useful in distinguishing T dwarfs from other late-type objects, as expected. The CH₄-A and CH₄-B indices start to decrease around L8 V to T1 V, while CH₄-C decreases as

early as L3 V to L5 V. The latter downturn is likely due to absorption by CIA H_2 in the late-L and T dwarfs, although we cannot rule out the early influence of CH_4 as a minor absorber.

The color indices (Figure 12c) reflect the well-known reddening seen in near-infrared photometry of M and L dwarfs, but shows that there is a smooth transition to bluer colors in the T dwarf regime. All three of these indices peak around L5 V, at which point colors become steadily bluer, with late T dwarf values below those of mid-M dwarfs. It is interesting to note that both H/J and K/J turn over at the same spectral type, since CIA H_2 likely affects only the latter index. Kirkpatrick et al. (1999) see a similar downturn in FeH and CrH bandstrengths in the red optical around L4 V to L5 V, and it is possible that these trends are in some way correlated, possibly through the precipitation of photospheric dust (see §6.3.2). Both the H/J and K/J indices appear to saturate and possibly reverse their downward trends between types T7 V and T8 V. The K/H index shows more scatter and is less useful than the other color indices.

The remaining indices (Figure 12d) are generally not useful for spectral classification over the full range of spectral types shown. The CO index shows a gradual decline from mid-M to early-T (implying increasing band strength), but is predominantly scatter for most of the T dwarfs due to $2.2\ \mu\text{m}$ CH_4 absorption. The $2.11/2.07$ index is generally constant from mid-M to early-T, but shows a downturn beyond T3 V. Despite the significant scatter, this index appears to separate mid- and late-T dwarfs from warmer objects, probably reflecting changes in the relative strengths of absorbers at K-band beyond T5 V. Finally, the K-shape index appears to show no real trends over the entire range of subtypes.

Overlaid on these plots are linear fits to select indices over discrete subtype ranges. Fits to T dwarfs are indicated by long-dashed lines, while fits to M and L dwarfs are indicated by short-dashed lines. Coefficients for these linear fits are given in Tables 12a and 12b, with values for the root mean square (RMS) deviations over the subtype ranges used. Most of these relations yield accurate spectral types to within ± 1.0 subclasses for the T dwarfs.

5.5. A Recipe for Spectral Classification

Based on the discussion above, we outline a procedure for determining the spectral type of T dwarfs using near-infrared data:

1. Measure the $\text{H}_2\text{O-A}$, $\text{H}_2\text{O-B}$, $\text{CH}_4\text{-A}$, $\text{CH}_4\text{-B}$, $\text{CH}_4\text{-C}$, H/J, K/J, and $2.11/2.07$ indices as defined in Table 9. A subset of these indices can be used when spectral data do not extend into the required spectral regions.
2. Compare each index with standard values, either from Table 10 or (preferably) from measurements using the same instrumental setup. Compute spectral types for each index.
3. Average the derived subtypes, rejecting the single high and low values, to determine a mean

decimal spectral type. This decimal value rounded off to the nearest 0.5 subclass yields the final discrete subtype.

The linear relations given in Table 12a can be used to derive individual spectral types in step 2, although trends in the indices are not necessarily linear and direct comparison to standard values is generally preferable. Spectral types should be computed using as many of the indices listed in step 1 as possible, in order to reduce any biases due to differences in instrumentation (resolution or response characteristics) or observing conditions. Nonetheless, we find that this procedure yields consistent results for data with low to moderate resolutions to better than ± 1.0 subclasses.

5.6. Comparison to L Dwarf Classification Indices

A number of spectral indices have been defined to classify M and L dwarfs in the near-infrared, and it is useful to examine the behavior of these indices in the T dwarf regime. Tokunaga & Kobayashi (1999) defined two indices at K-band to measure the strengths of the $1.9 \mu\text{m}$ H_2O and CIA H_2 :

$$K1 = \frac{\langle F_{2.10-2.18} \rangle - \langle F_{1.96-2.04} \rangle}{0.5(\langle F_{2.10-2.18} \rangle + \langle F_{1.96-2.04} \rangle)} \quad (3)$$

$$K2 = \frac{\langle F_{2.20-2.28} \rangle - \langle F_{2.10-2.18} \rangle}{0.5(\langle F_{2.20-2.28} \rangle + \langle F_{2.10-2.18} \rangle)}, \quad (4)$$

the latter of which is also sensitive to CH_4 in the T dwarfs. Figure 13 is an extension of Figure 4 from Tokunaga & Kobayashi (1999), comparing these indices for types M (triangles), L (squares), and T (circles) from the NIRC (open symbols) and CGS4 (filled symbols) datasets. T dwarf standards and representative M and L dwarfs are labeled by their spectral types. The K1 index appears to peak in the early T dwarfs, then decreases toward the later T dwarfs, similar to what is seen in our $\text{H}_2\text{O}-\text{C}$ index. K2 decreases from late L through late T, reflecting increased CH_4 and CIA H_2 toward cooler temperatures. Despite significant scatter in the T dwarf regime, these indices, defined for objects with $2600 \gtrsim T_{\text{eff}} \gtrsim 1500 \text{ K}$, do show trends in objects as cool as $\sim 800 \text{ K}$.

Reid et al. (2001) have defined two indices for L dwarfs that measure the blue and red wing of the $1.4 \mu\text{m}$ H_2O band; respectively,

$$H_2O^A = \frac{\langle F_{1.33-1.35} \rangle}{\langle F_{1.28-1.30} \rangle} \quad (5)$$

$$H_2O^B = \frac{\langle F_{1.47-1.49} \rangle}{\langle F_{1.59-1.61} \rangle}. \quad (6)$$

We plot these indices versus spectral type in Figure 14, using NIRC (diamonds) and CGS4 (squares) data; filled circles denote values for L and T dwarf spectral standards. The index-spectral type relations from Reid et al. (2001), defined over the range M8 V to L8 V, are plotted as short-dashed lines. These relations are extended into the T dwarf region for comparison. The H_2O^A index does

not track linearly into the T regime, due to contamination by the $1.3\ \mu\text{m}$ CH_4 band. The H_2O^B index is remarkably linear, however, over the entire subtype range shown. A fit to this index over types M5 V through T8 V yields (long-dashed line):

$$SpT = (12.6 \pm 0.9) - (26.7 \pm 0.6) \times [H_2O^B], \quad (7)$$

with an RMS scatter of 1.2 subtypes, where $SpT(\text{T0 V}) = 0$, $SpT(\text{T5 V}) = 5$, $SpT(\text{L5 V}) = -4$, etc. This relation is consistent with that derived by Reid et al. (2001), and it appears that the H_2O^B index is useful for classification over a broad range of late-type dwarfs.

6. Properties of T Dwarf Subtypes

Having established a spectral classification scheme that consistently characterizes changes in near-infrared spectral morphology, we now examine some of the general properties of the individual subtypes. From the behaviors of spectral features and colors, it is possible to probe some of the fundamental properties of these cool brown dwarfs.

6.1. $1.25\ \mu\text{m}$ K I doublet

The 1.2432 and $1.2522\ \mu\text{m}$ K I transitions are particularly useful diagnostics of photospheric temperature. These higher order lines originate in the $4p\ ^2P_0$ level, 1.6 eV above the $4s\ ^2S$ ground state. For local thermodynamic equilibrium (LTE), the relative number density of the excited state goes as $T^{12.5}$ at a photospheric temperature of $\sim 1500\ \text{K}$ ¹⁶. We might therefore expect to see the $1.25\ \mu\text{m}$ lines weaken sharply as the photospheric temperature at J-band decreases.

We have measured the pseudo-equivalent widths (PEWs) of the K I lines by integrating over their line profiles:

$$PEW = \frac{\int [C(\lambda) - f(\lambda)] d\lambda}{C(\lambda_c)}, \quad (8)$$

where $C(\lambda)$ is the neighboring pseudo-continuum and λ_c the transition wavelength. Results for OSIRIS data and literature CGS4 data are given in Tables 13a and 13b, respectively, which list the central wavelength and PEW for each transition. Errors were determined from the noise in the neighboring pseudo-continuum. Figure 15 plots these values versus spectral type, with OSIRIS data shown as triangles and CGS4 data as squares. There is an apparent strengthening of the $1.2432\ \mu\text{m}$ line from the mid-M dwarfs to the mid-L dwarfs, which is present but more subtle at $1.2522\ \mu\text{m}$. The growth of the $1.2432\ \mu\text{m}$ line is likely influenced by contamination of FeH at $1.237\ \mu\text{m}$; however, the gradual strengthening of both lines mimic that of the $0.77\ \mu\text{m}$ K I resonance

¹⁶The $0.77\ \mu\text{m}$ resonance doublet, which populates the $4p\ ^2P_0$ level, has a similar transition rate (Wiese, Smith, & Glennon 1966) but is a much stronger feature, due to the greater number of atoms in the ground state.

doublet in red optical data (Kirkpatrick et al. 1999). There is a significant drop in the PEWs of the $1.2432\ \mu\text{m}$ line between L5 V and L7 V, likely due to the disappearance of the FeH lines (McLean et al. 2000), although a subtle dip may be present in the $1.2522\ \mu\text{m}$ line strengths. Both lines appear to peak up slightly in the mid-T dwarfs, and then drop toward T8 V (Gliese 570D). The mid-T peak is unexpected assuming LTE, both in terms of the presumably cooler photospheres of these objects and the presence of overlying H_2O and CH_4 absorption centered at $1.15\ \mu\text{m}$. Relative opacity and depth effects are clearly important in the formation of the K I line, and their re-strengthening may be the result of greater transparency at J-band as dust layers settle deeper into the atmosphere or begin to rain out (Burrows & Sharp 1999; Ackerman & Marley 2001). Dropping temperatures and/or H_2O and CH_4 opacity likely leads to the disappearance of these lines in the latest T dwarfs. The complicated behavior of the K I lines reflects the competing influences of decreasing temperature and increasing transparency as dust settles out of the photosphere, but contributions by neighboring molecular features must be considered as well.

6.2. Near-infrared Colors

The 2MASS near-infrared colors of T dwarfs versus spectral type are shown in Figure 16. Colors for individual objects are indicated by open diamonds, with arrows indicating upper limits for objects not detected in both bands. Solid points give the weighted (by photometric uncertainty) mean colors for each half subtype, computed only from those objects with definite color measurements. These values are listed in Table 14. L dwarf average colors from Kirkpatrick et al. (2000) are also shown in Figure 16 for comparison. The reddening of near-infrared colors through the L dwarfs, and subsequent shift to bluer colors in the T dwarfs, closely resemble the trends seen in the H/J, K/J, and K/H color indices in Figure 12c, although the L5 V peak is not as readily apparent. Color breaks between L8 V and T1 V, and between T3 V and T5 V, are evident in the J-H and J- K_s colors. We note, however, that the T3 V object, SDSS 1021-0304, appears to be slightly redder than the T2 V SDSS 1254-0122 in all three colors. Beyond T5 V, colors appear to saturate around J-H ~ 0.0 , H- $K_s \sim 0.1$, and J- $K_s \sim 0.1$, although any trends (such as the slight rise in the H/J and K/J color indices between T7 V and T8 V) may be hidden by photometric uncertainties of 0.1–0.3 mag. The mean H- K_s and J- K_s colors for T6 V objects are biased by the very blue colors of the T6 Vp 2MASS 0937+2931 (see §8); excluding this object, colors for this subtype generally match those for T5.5 V through T8 V. The largest color changes therefore occur between L8 V and T5 V, with later objects showing little variation in near-infrared colors, despite apparent differences in spectral morphology.

6.3. Effective Temperatures

Spectral types in the MK system generally map onto an underlying temperature (or more accurately, ionization) scale, while separate luminosity classes yield radius/surface gravity information.

The temperature and luminosity of a brown dwarf are directly related, however, as substellar radii remain constant to within 35% for effective temperatures less than 2200 K and ages greater than of 0.01 Gyr (Burrows et al. 1997), with little variation due to metallicity (Chabrier & Baraffe 2000). Thus, for most field L and T dwarfs:

$$T_{eff}(K) = \left(\frac{L}{4\pi R^2 \sigma}\right)^{0.25} \sim 555 \left(\frac{L}{10^{-6} L_{\odot}}\right)^{0.25} \quad (9)$$

to within 20%, assuming $R = 7.5 \times 10^9$ cm = $1.06 R_{Jup} = 0.11 R_{\odot}$. This simple relation is important when we consider the difficulty in estimating effective temperature from spectral data. These objects are clearly not blackbodies, and brightness temperatures derived from spectral data can range over 1000 K in the 1–2.5 μ m regime (Saumon et al. 2000). However, a reasonable estimate of T_{eff} can be obtained if the total luminosity of a degenerate brown dwarf is known. This approach only requires assumptions based on the well-understood internal physics of brown dwarfs, rather than relying on extensive atmospheric modeling.

6.3.1. The Temperatures of L dwarfs

Luminosities for a number of late-M and L dwarfs have recently been compiled by Leggett et al. (2001) and Reid et al. (2001). These authors calculate bolometric corrections by extrapolating near-infrared spectral and photometric data to shorter and longer wavelengths. Luminosities are then determined by:

$$\log\left(\frac{L}{L_{\odot}}\right) = -0.4(m_b + BC_b + 5\log\pi + 5 - M_{bol,\odot}) = -0.4M_{bol} + 1.896 \quad (10)$$

where $M_{bol} = M_b + BC_b$ is the intrinsic bolometric magnitude (intrinsic brightness plus bolometric correction at band b), determined from the parallax π (in arcsec), and using $M_{bol,\odot} = 4.74$ (Livingston 2000). T_{eff} can then be computed from Equation 9.

Figure 17 plots the effective temperatures for late-M and L dwarfs with known parallaxes (Kirkpatrick et al. 2000, 2001a; Wilson et al. 2001b), using 2MASS photometry and J-band bolometric corrections from Reid et al. (2001):

$$BC_J = 1.904 - 0.034 \times SpT \quad (11)$$

(here, $SpT(L0) = 0$, $SpT(L5) = 5$, $SpT(M5) = -4$, etc.) and Equations 9 and 10 above. Based on uncertainties in the T_{eff} –luminosity relation and scatter in Equation 11 (about 0.1 mag), we estimate T_{eff} uncertainties at 15%. Also plotted in this diagram are T_{eff} estimates from Leggett et al. (2001), based on K-band bolometric corrections and structure models from Chabrier et al. (2000). There is a good correlation between these two temperatures sets, with differences for common objects never exceeding ± 100 K. The data show a fairly monotonic decrease in T_{eff} with spectral type from M9 V to L8 V; a linear fit yields (dashed line):

$$T_{eff}(K) = 2190 - 113 \times SpT, \quad (12)$$

with an RMS deviation of 120 K. We compare this relation to the Kirkpatrick et al. (1999, 2000) and Basri et al. (2000) L dwarf temperature scales (solid lines) in Figure 17, where the latter scale has been adjusted to the Kirkpatrick et al. (1999) L dwarf types using transformations given in Martín et al. (1999). These scales clearly bracket the effective temperatures calculated here and from Leggett et al. (2001) for most of the L dwarfs, although the Kirkpatrick scale generally underestimates temperatures for the early L dwarfs, while the Basri scale overestimates temperatures for the late L dwarfs. Additional discussion on the L dwarf temperature scale is given in Gizis et al. (2001b).

6.3.2. *The Temperatures of T dwarfs*

Currently, only two T dwarfs have known distances and hence absolute brightness determinations: Gliese 229B and Gliese 570D. Because they are companions to well-studied bright stars, accurate estimates of effective temperature for these objects have been derived using evolutionary models and the properties of their primaries (Marley et al. 1996; Allard et al. 1996; Tsuji et al. 1996b; Burgasser et al. 2000a; Geballe et al. 2001a); these temperatures are plotted as solid circles in Figure 17.

It is clear that an extrapolation of Equation 13 into the T dwarf regime substantially underestimates the temperatures of these objects. Indeed, as pointed out by Kirkpatrick et al. (2000), there appears to be a relatively small difference in T_{eff} between the coolest L dwarfs and Gliese 229B, only ~ 350 K. How do we resolve this situation with the observed changes in spectromorphology and photometric colors, including the apparently continuous strengthening of H_2O indices across the L/T boundary? The solution to this problem may lie in the behavior of atmospheric dust. Recent models by Ackerman & Marley (2001) indicate that dust clouds, which significantly modify the emergent spectra of L dwarfs, reside at the 1500–1800 K temperature layer in brown dwarfs, and thus begin to settle below the photosphere around the L/T transition. Tsuji, Ohnaka, & Aoki (1999) find a similar critical temperature at $T_{cr} = 1550$ K. Loss of dust opacity likely causes substantial redistribution of emergent flux, increasing transparency in some spectral regions, while also increasing H_2O and (ultimately) CH_4 band strengths as the photosphere cools. In addition, the cooling of the atmosphere above the dust layers will drive the formation of CH_4 and H_2O , increasing their column abundances and hence further increasing band strengths. These events should result in a significant strengthening of molecular bands over a narrow T_{eff} range. The dust loss scenario also explains the strengthening of the $1.25\ \mu m$ K I doublet from L8 V to T5 V, inducing greater transparency at J-band and a corresponding increase in column abundance. Another intriguing scenario suggested by Ackerman & Marley (2001) is the formation of holes in the dust clouds, or “hot spots”, similar to what is seen on Jupiter at $5\ \mu m$ (Westphal, Matthews, & Terrile 1974). Small bright regions could potentially dominate over discrete spectral bands, modifying the emergent flux with little change to the total luminosity or effective temperature.

Based on these considerations, we speculate that the evolution of brown dwarfs from spectral types L8 V to T5 V occurs over a narrow range in T_{eff} , perhaps as little as 200 K (dot-dashed line).

This temperature difference is similar to that between Gliese 229B (T6.5 V) and Gliese 570D (T8 V). Because dust resides in a relatively narrow range of thermal layers, its effect on the emergent spectrum below $T_{eff} \sim 1000$ K will no longer be important. Indeed, dust-free models by Tsuji et al. (1996b) provided better fits to the spectrum of Gliese 229B than corresponding dusty models. The evolution of spectral features at this point should once again be tied to effective temperature, with spectral types later than roughly T6 V sampling a broader range of T_{eff} . Parallax observations of T dwarfs are necessary to test this hypothesis, and variability observations of the latest L dwarfs and earliest T dwarfs could also provide clues to the behavior of atmospheric dust as it settles below the photosphere. Note that a narrow T_{eff} range for objects of type L8 V through T5 V would imply a paucity of these brown dwarfs relative to later-type T dwarfs; more accurate space densities are needed to test this prediction. Nonetheless, we believe that the rapid depletion of dust provides a natural explanation to the observed evolution of spectral features and estimated effective temperatures.

7. DENIS 0205-1159AB and the L/T Transition

The behavior of spectral indices and colors between the latest L dwarfs and early T dwarfs shows a small morphological gap between L8 V and T1 V. The recent detection of the fundamental band of CH_4 at $3.3 \mu\text{m}$ in objects as early as L5 V (Noll et al. 2000) and the lack of objects later than L8 V in 2MASS L dwarf searches (Kirkpatrick et al. 2000) both suggest that the separation in temperature between these two classes is also not large. To investigate the L/T transition, we examined the near-infrared spectrum of the L7 V DENIS 0205-1159AB, a bright, well-studied, equal-magnitude binary (Koerner et al. 1999; Leggett et al. 2001), 17.5 pc from the Sun (Kirkpatrick et al. 2000). Delfosse et al. (1997) discovered this object in DENIS survey data, and identified a feature at $2.22 \mu\text{m}$ that they attributed to weak CH_4 absorption. Tokunaga & Kobayashi (1999) rejected this hypothesis, however, favoring CIA H_2 absorption based on the spectral models of Tsuji, Ohnaka, & Aoki (1999).

Figure 18 plots spectral data from 2.01 to $2.35 \mu\text{m}$ for DENIS 0205-1159AB obtained from Delfosse et al. (1997), Tokunaga & Kobayashi (1999), Leggett et al. (2001), and Reid et al. (2001). Near-infrared spectral data for SDSS 0539-0059 (L5 V) and SDSS 1254-0122 (T2 V) from Leggett et al. (2000) are also shown for comparison. Spectra are normalized at their K-band peaks (short-dashed lines) and offset for comparison. Above these data are opacity spectra for CIA H_2 (thick line), CH_4 (thin line), H_2O (dashed line), and CO (dot-dashed line) at $T = 1400$ K and $P = 1$ bar (see references in Burrows et al. 1997). This combination of temperature and pressure is expected to represent the typical photospheric conditions for a 1 Gyr, $T_{eff} = 1500$ K brown dwarf (Burrows et al. 1997; Ackerman & Marley 2001). Opacity data for CH_4 , H_2O , and CO have been scaled by their number densities relative to H_2 using the chemical equilibrium models of Burrows & Sharp (1999).

The opacity spectra indicate that the broad absorption feature seen from 2.18 to $2.29 \mu\text{m}$ is a

combination of CIA H_2 , CH_4 , and H_2O , with CIA H_2 being the strongest contributor beyond $2.1\ \mu\text{m}$. In addition, there is a weak absorption feature at $2.20\ \mu\text{m}$ (arrows) present in all of the DENIS 0205-1159AB spectra except that of Leggett et al. (2001) that closely corresponds to a sharp feature in the CH_4 opacity spectrum. This absorption is only slightly offset from the $2.2056/2.2084\ \mu\text{m}$ Na I doublet ($4s\ ^2\text{S} \rightarrow 4p\ ^2\text{P}_0$), indicated by vertical lines in Figure 18. The high-energy Na I lines form $3.2\ \text{eV}$ above the ground state and appear to weaken over types late-M to mid-L (Reid et al. 2001). It is likely, therefore, that Na I is not responsible for this feature in DENIS 0205-1159AB.

Does the weak $2.20\ \mu\text{m}$ feature constitute a clear detection of CH_4 at K-band in the latest L dwarfs? In our opinion it does not, due to the weakness and occasional non-detection of the absorption. Its apparent variability in the spectra of Figure 18 may be intrinsic to the source, as a number of L- and T-type brown dwarfs have recently been shown to be variable, both photometrically (Bailer-Jones & Mundt 1999, 2001) and spectroscopically (Nakajima et al. 2000; Kirkpatrick et al. 2001a), likely due to patchy clouds of dust in the photosphere (Ackerman & Marley 2001). Differences in instrumental resolution and observing conditions, however, make this interpretation ambiguous, and the weakness of this feature may lend doubt to its reality. Higher resolution, higher signal-to-noise, and time-resolved data are required to confirm its authenticity and possible variable nature.

Nonetheless, the opacity spectra in Figure 18 do suggest that CH_4 is an important minor absorber at these temperatures, and its emergence as an identifiable feature likely occurs in objects only slightly cooler than DENIS 0205-1159AB. This suggests that the earliest T dwarfs (i.e., those with clear CH_4 bands) are probably not significantly cooler than the latest L dwarfs currently known. In that case, L8 V may be the last subtype of the L spectral class, with cooler objects showing obvious CH_4 absorption features at K-band, classifying them as T dwarfs. In order to verify this hypothesis, it is necessary to identify more of the so-called “L/T transition” objects and determine at what point the detection of CH_4 becomes unambiguous at J-, H-, and K-bands. Note that even if the $2.20\ \mu\text{m}$ CH_4 feature is confirmed in DENIS 0205-1159AB or in other L7/L8 dwarfs, it does not necessitate a reclassification of these objects, much as the $3.3\ \mu\text{m}$ absorption seen in mid- and late-L dwarfs reclassify them as T dwarfs (Noll et al. 2000), or the presence of TiO bands in bright K5 and K7 dwarfs (Reid, Hawley, & Gizis 1995) reclassify them as M dwarfs. The weak feature described here may indicate that the latest-type L dwarfs known are close to the L/T boundary, but not that they have traversed it.

8. 2MASS 0937+29: A Template for Measuring Gravity/Composition?

One T dwarf that deserves special attention is the T6 Vp 2MASS 0937+2931, designated peculiar because of its highly suppressed K-band peak. Indeed, this object’s near-infrared colors are significantly bluer than any other T dwarf so far identified. As can be seen in Table 13a and Figures 7 and 15, 2MASS 0937+2931 also has very weak or absent $1.25\ \mu\text{m}$ K I absorption, weaker even than the T8 V Gliese 570D.

To identify the source of this anomalous absorption, we again examined the molecular contributors to the photospheric opacity in this object. Figure 19 plots 1.9–2.3 μm NIRC data for 2MASS 0937+2931 (solid line) along with data for the T6 V standard 2MASS 0243-2453. Both spectra are normalized at their J-band peaks and match very well from 1–1.8 μm ; however, 2MASS 0937+2931 is nearly 50% fainter at K-band. Plotted above this are opacity spectra for CIA H₂ (thick solid line), CH₄ (solid line), and H₂O (dotted line) at $T = 1000$ K and $P = 1$ bar, with CH₄ and H₂O scaled to their chemical equilibrium relative number densities (Burrows & Sharp 1999). H₂O and CH₄ are clearly more important at cooler temperatures, as CIA H₂ at 1 bar is only a minor absorber outside of the 2.1 μm window. However, because H₂ features form via collisional processes, they strengthen with increasing pressure, scaling roughly as $\sigma \propto P$. This effect can be seen in the increased opacity of CIA H₂ for $P = 10$ bar (thick dashed line). The corresponding opacities of H₂O and CH₄ are generally unaffected by changes in pressure; and at or below $T \sim 1000$ K, number densities at equilibrium remain essentially unchanged (Burrows & Sharp 1999). Thus, CIA H₂ is the only major molecular absorber sensitive to local pressure in T dwarf atmospheres.

Photospheric pressure is directly related to specific gravity by hydrostatic equilibrium:

$$\frac{dP}{d\tau} \sim \frac{P}{\tau} = \frac{g}{\kappa_R} \propto \frac{M}{R^2 \kappa_R}. \quad (13)$$

Because brown dwarf radii are roughly constant, this implies the (simplistic) relation $P_{\text{phot}} \propto M$ for constant κ_R . Thus, at a given T_{eff} and composition, an older, more massive object will tend to have a higher photospheric pressure than a younger, less massive object, and hence stronger CIA H₂ absorption. If we assume that most T dwarfs identified to date have masses between 40 to 60 M_{Jup} (assuming $800 < T_{\text{eff}} < 1200$ and $1 < \tau < 5$ Gyr), then CIA H₂ absorption should be 1.5 times stronger in 2MASS 0937+2931 if it were a 75 M_{Jup} object. The structure models of (Burrows et al. 1997) predict a factor of 1.75 increase in specific gravity due to the increased contraction of the older, more massive object. Thus, significant differences in photospheric pressures are possible. However, a 75 M_{Jup} brown dwarf with $T_{\text{eff}} = 1000$ K would also have to be older than 11.5 Gyr (Burrows et al. 1997).

An alternate hypothesis for the strong K-band absorption in 2MASS 0937+2931 is decreased metallicity. Zero-metallicity brown dwarf spectral models are dominated by CIA H₂ opacity and peak shortward of 1 μm ; when molecular absorption is included, the suppression of flux at shorter wavelengths increases the relative luminosity at K-band by roughly a factor of 2 (Saumon, Chabrier, & Van Horn 1995). If the metallicity of a brown dwarf atmosphere were decreased from $Z = Z_{\odot}$ to 0.1 Z_{\odot} , the number densities of CH₄ and H₂O and (in an approximate sense) their relative opacities would also decrease roughly by a factor of 10. Decreased metallicity would not significantly affect the amount of photospheric H₂ present, although it may slightly alter the opacity spectrum. Assuming photospheric pressure remained constant, one might expect the same relative opacity contributions in this scenario as in the $Z = Z_{\odot}$, $P = 10$ bar case. Decreased metallicity would also explain the deficit of K I absorption seen at J-band. Note that because of the reduced opacity and corresponding increased luminosity, brown dwarfs with subsolar metallicity cool more rapidly

(Chabrier & Baraffe 1997). Thus, a metal-poor model for 2MASS 0937+2931 is either younger (same mass) or more massive (same age) than its solar metallicity, $T_{eff} = 1000$ K counterpart, while a high-pressure model must be both older and more massive.

These arguments are based on very simple scaling laws of abundance and opacity, and disentangling the effects of T_{eff} , specific gravity, and metallicity on the emergent spectrum of 2MASS 0937+2931 requires more extensive modeling. It is clear, however, that CIA H_2 plays an important role in shaping the spectra of both L and T dwarfs, and its sensitivity to the ambient pressure makes it an excellent tracer of surface gravity and hence mass. Diagnostics that measure the relative contributions of CIA H_2 , CH_4 , and H_2O may allow us to extract the physical characteristics of these constantly evolving objects.

9. Conclusions

In 1995, the discovery of the uniquely cool brown dwarf Gliese 229B was announced, an object exhibiting CH_4 absorption features reminiscent of the reflectance spectrum of the giant planet Jupiter (Oppenheimer et al. 1995). Six years later, at least two dozen counterparts have been identified, the majority found only in the past two years by the 2MASS and SDSS surveys. We now know that these objects, T dwarfs, form a distinct spectral class, defined by the presence of CH_4 absorption bands in the near-infrared.

In this article, we have examined the morphologies of the CH_4 and H_2O bands and J, H, and K flux peaks that characterize the 1–2.5 μm spectra of known and newly discovered T dwarfs. Based on these features, we have made a first attempt to define a classification scheme for T dwarfs which segregates the currently known population into subtypes T1 V, T2 V, T3 V, T5 V, T6 V, T7 V, and T8 V. We have also introduced a prescription for near-infrared classification using a suite of spectral indices that measure the strengths of CH_4 and H_2O bands, near-infrared colors, and the evolution of the K-band peak. Our work parallels independent efforts reported by Geballe et al. (2001b) in this volume, who produce a nearly identical sequence based on CGS4 spectral data (D. Golimowski, priv. comm.). That this should be the case is not surprising, since both schemes are based on the observed strengths of H_2O and CH_4 features. Nevertheless, their independent convergence intimates a natural order in the spectra of T dwarfs.

From the properties of spectral features, particularly H_2O bands, and the progression of near-infrared colors, it appears that the latest L dwarfs are not very different from the earliest T dwarfs. The possible role of CH_4 as a minor contributor in shaping the K-band peak of the latest L dwarfs, and the recent detection of CH_4 at 3.3 μm in objects as early as L5 V (Noll et al. 2000), lead us to believe that perhaps only one subclass exists between the latest L subtype (L8 V) and the earliest T subtype (T1 V). Thus, the gap between these two separately defined spectral classes appears to be effectively bridged.

The evolution of spectral features from late L to early T dwarfs is likely dominated by the

behavior of atmospheric dust, which greatly influences the near-infrared spectra of L dwarfs but appears to be absent in T dwarfs such as Gliese 229B (Tsuji et al. 1996b; Allard et al. 1996; Marley et al. 1996). The condensation and gravitational settling of dust clouds leads to a substantial evolution of spectral morphology, possibly over a narrow T_{eff} range. A rapid depletion of observed dust opacity, perhaps stimulated by the formation of holes in dust clouds extending to significantly hotter layers, could explain both the small effective temperature difference between the ~ 1300 K L8 V Gliese 584C (Kirkpatrick et al. 2000) and the ~ 950 K T6.5 V Gliese 229B (Saumon et al. 2000), as well as the behavior of K I line strengths at J-band. One may argue that the spectral transition between the L and T classes is driven more by the physics of dust condensation than by the thermochemical formation of CH_4 bands (in addition, the latter process is likely driven by the former). Modeling the L/T transition clearly requires a more accurate treatment of the condensation, coagulation, and settling of dust species (Tsuji, Ohnaka, & Aoki 1999; Ackerman & Marley 2001). A similarly complex transition may occur with the condensation of H_2O at $T_{eff} \sim 400$ K (Burrows et al. 1997), a possible endpoint to the T spectral class.

In any case, the near-infrared classification scheme derived in this article appears to adequately represent nearly all of the currently known T dwarfs. Atmospheric models, spectral indices, and the properties of the two known T dwarf companions Gliese 229B and Gliese 570D imply that this scheme maps directly onto a decreasing temperature sequence. Extensive modeling is required to derive the true physical properties of the observed objects, and hence our interpretations are best deemed preliminary. However, we believe that the one notable anomaly, 2MASS 0937+2931, which has a highly suppressed K-band peak likely caused by increased opacity from CIA H_2 , could be an extreme example of an old, high-mass brown dwarf or one with diminished metallicity. Determining the properties of this unusual T dwarf will enable us to understand how the physical characteristics of mass, age, and composition separately shape the emergent energy distribution of cool brown dwarfs. It is clear that the identification of new T dwarfs in the 2MASS and SDSS surveys will help fill in the current gaps, both in the spectral sequence (which must be developed to include such discoveries) and in our understanding of processes occurring in cool brown dwarf atmospheres.

A. J. B. would like to thank J. Cuby, X. Delfosse, T. Geballe, S. Leggett, M. Strauss, A. Toku-naga, and Z. Tsvetanov for providing electronic versions of their published spectra, and acknowledges useful discussions with R. Blum, D. Golimowski, M. Marley, G. Neugebauer, D. Saumon, and M. R. Zapatero Osorio in the preparation of the manuscript. Observations described in this article would not have been possible without the assistance of our knowledgeable telescope operators and instrument specialists: Mike Doyle, Karl Dunscombe, Jean Mueller, Kevin Rykowski, Barrett “Skip” Staples, and Merle Sweet at Palomar; Teresa Chelminiak, Bob Goodrich, Chuck Sorenson, and Meg Whittle at Keck; and Maria Theresa Acevedo, Alberto Alvarez, Robert Blum, Mauricio Fernandez, Angel Guerra, and Patricio Ugarte at CTIO. A. J. B., J. D. K., and J. E. G. acknowledge the support of the Jet Propulsion Laboratory, California Institute of Technology, which is operated under contract with the National Aeronautics and Space Administration. A. B. acknowledges support from NASA grants NAG 5-7073, NAG 5-7499, and NAG 5-10629. Portions

of the data presented herein were obtained at the W. M. Keck Observatory which is operated as a scientific partnership among the California Institute of Technology, the University of California, and the National Aeronautics and Space Administration. The Observatory was made possible by the generous financial support of the W. M. Keck Foundation. The Digitized Sky Survey was produced at the Space Telescope Science Institute under US Government grant NAG W-2166. DSS images were obtained from the Canadian Astronomy Data Centre, which is operated by the Herzberg Institute of Astrophysics, National Research Council of Canada. This research has made use of the SIMBAD database, operated at CDS, Strasbourg, France. This publication makes use of data from the Two Micron All Sky Survey, which is a joint project of the University of Massachusetts and the Infrared Processing and Analysis Center, funded by the National Aeronautics and Space Administration and the National Science Foundation.

REFERENCES

- Ackerman, A. S., & Marley, M. S. 2001, *ApJ*, 556, in press
- Allard, F., Hauschildt, P. H., Baraffe, I., & Chabrier, G. 1996, *ApJ*, 465, L123
- Bailer-Jones, C. A. L. 2001, in *Automated Data Analysis in Astronomy*, ed. R. Gupta, H. P. Singh, & C. A. L. Bailer-Jones (New Delhi: Narosa Publishing House), in press
- Bailer-Jones, C. A. L., & Mundt, R. 2001, *A&A*, 367, 218
- Bailer-Jones, C. A. L., & Mundt, R. 1999, *A&A*, 348, 800
- Basri, G., Mohanty, S., Allard, F., Hauschildt, P. H., Delfosse, X., Martín, E. L., Forveille, T., & Goldman, B. 2000, *ApJ*, in press
- Becklin, E. E., & Zuckerman, B. 1988, *Nature*, 336, 656
- Bergeron, P., Wesemael, F., & Beauchamp, A. 1995, *PASP*, 107, 1047
- Bessell, M. S., & Brett, J. M. 1988, *PASP*, 100, 1134
- Burgasser, A. J. 2001, in *The Fourth Tetons Summer Conference: Galactic Structure, Stars, and the Interstellar Medium*, ed. C. W. Woodward, M. Bica, & J. M. Schull (San Francisco: ASP), in press
- Burgasser, A. J., et al. 2000a, *ApJ*, 531, L57
- Burgasser, A. J., Kirkpatrick, J. D., Reid, I. N., Liebert, J., Gizis, J. E., & Brown, M. E. 2000b, *AJ*, 120, 473
- Burgasser, A. J., et al. 2000c, *AJ*, 120, 1100

- Burgasser, A. J., et al. 1999, *ApJ*, 522, L65
- Burrows, A., Hubbard, W. B., Lunine, J. I., & Liebert, J. 2001, *Rev. of Modern Physics*, in press
- Burrows, A., Marley, M. S., & Sharp, C. M. 2000, *ApJ*, 531, 438
- Burrows, A., & Sharp, C. M. 1999, *ApJ*, 512, 843
- Burrows, A., et al. 1997, *ApJ*, 491, 856
- Cao, L. 1998, *IAUC*, 6994
- Chabrier, G., & Baraffe, I. 2000a, *ARA&A*, 38, 337
- Chabrier, G., Baraffe, I., Allard, F., & Hauschildt, P. 2000b, *ApJ*, 542, 464
- Chabrier, G., & Baraffe, I. 1997, *A&A*, 327, 1039
- Cuby, J. G., Saracco, P., Moorwood, A. F. M., D’Odorico, S., Lidman, C., Comerón, F., & Spyromilio, J. 1999, *A&A*, 349, L41
- Delfosse, X., et al. 1997, *A&A*, 327, L25
- Depoy, D. L., Atwood, B., Byard, P. L., Frogel, J., & O’Brien, T. P. 1993, in *Proceedings of SPIE*, Vol. 1946, ed. A. M. Fowler (Bellingham: SPIE), 667
- Epchtein, N., et al. 1997, *The Messenger*, 87, 27
- Fan, X., et al. 2000, *AJ*, 119, 928
- Fink, U., & Larson, H. P. 1979, *ApJ*, 233, 1021
- Geballe, T. R., Saumon, D., Leggett, S. K., Knapp, G. R., Marley, M. S., & Lodders, K. 2001a, *ApJ*, in press
- Geballe, T. R., et al. 2001b, *ApJ*, in prep.
- Geballe, T. R., Kulkarni, S. R., Woodward, C. E., & Sloan, G. C. 1996, *ApJ*, 467, 101
- Gizis, J. E., Kirkpatrick, J. D., & Wilson, J. C. 2001a, *AJ*, in press
- Gizis, J. E., et al. 2001b, *AJ*, submitted
- Gizis, J. E., Monet, D. G., Reid, I. N., Kirkpatrick, J. D., Liebert, J., & Williams, R. 2000, *AJ*, 120, 1085
- Goldman, B., et al. 1999, *A&A*, 351, L5
- Golimowski, D. A., Burrows, C. S., Kulkarni, S. R., Oppenheimer, B. R., & Brukardt, R. A. 1998, *AJ*, 115, 2579

- Hawkins, M. R. S., & Bessell, M. S. 1988, *MNRAS*, 234, 177
- Jones, H. R. A., Longmore, A. J., Jameson, R. F., & Mountain, C. M. 1994, *MNRAS*, 267, 413
- Kirkpatrick, J. D., Dahn, C. C., Monet, D. G., Reid, I. N., Gizis, J. E., Liebert, J., & Burgasser, A. J. 2001a, *AJ*, 121, 3235
- Kirkpatrick, J. D., et al. 2001b, *ApJ*, in prep.
- Kirkpatrick, J. D., Reid, I. N., Liebert, J., Gizis, J. E., Burgasser, A. J., Monet, D. G., Dahn, C. C., Nelson, B., & Williams, R. J. 2000, *AJ*, 120, 447
- Kirkpatrick, J. D., et al. 1999, *ApJ*, 519, 802
- Koerner, D. W., Kirkpatrick, J. D., McElwain, M. W., & Bonaventura, N. R. 1999, *ApJ*, 526, L25
- Leggett, S. K., Allard, F., Geballe, T., Hauschildt, P. H., & Schweitzer, A. 2001, *ApJ*, in press
- Leggett, S. K., et al. 2000, *ApJ*, 536, L35
- Leggett, S. K., Toomey, D. W., Geballe, T. R., & Brown, R. H. 1999, *ApJ*, 517, L139
- Leggett, S. K., Allard, F., & Hauschildt, P. H. 1998, *ApJ*, 509, 836
- Liebert, J., Reid, I. N., Burrows, A., Burgasser, A. J., Kirkpatrick, J. D., & Gizis, J. E. 2000, *ApJ*, 533, L155
- Livingston, W. C. 2000, in *Allen’s Astrophysical Quantities*, Fourth Edition, ed. A. N. Cox (New York: Springer-Verlag), p. 151
- Luhman, K. L., Rieke, G. H., Young, E. T., Cotera, A. S., Chen, H., Rieke, M. J., Schneider, G., Thompson, R. I. 2000, *ApJ*, 540, 1016
- Luyten, W. J. 1979, *A Catalogue of Stars with Proper Motions Exceeding 0.5 Annually* (Univ. Minn. Press: Minneapolis)
- Marley, M. S., Saumon, D., Guillot, T., Freedman, R. S., Hubbard, W. B., Burrows, A., & Lunine, J. I. 1996, *Science*, 272, 1919
- Martín, E. L., Delfosse, X., Basri, G., Goldman, B., Forveille, T., & Zapatero Osorio, M. R. 1999, *AJ*, 118, 2466
- Martín, E. L., Basri, G., Zapatero Osorio, M. R., Rebolo, R., Lòpez, R. J. García 1998, *ApJ*, 507, L41
- Matthews, K., Nakajima, T., Kulkarni, S. R., & Oppenheimer, B. R. 1996, *AJ*, 112, 1678
- Matthews, K., & Soifer, B. T. 1994, in *Infrared Astronomy with Arrays: The Next Generation*, ed. I. McLean (Dordrecht: Kluwer), 239

- Maury, A. C., & Pickering, E. C. 1897, *Harvard College Observ. Ann.*, 28 (Part I), 1
- McLean, I., et al. 2001, *ApJ*, submitted
- McLean, I., et al. 2000, *ApJ*, 533, L45
- Monet, D., et al. 1998, *USNO-A2.0 Catalog* (Flagstaff: USNO)
- Morgan, D. H., Tritton, S. B., Savage, A., Hartley, M., & Cannon, R. D. 1992, in *Digitised Optical Sky Surveys*, ed. H. T. MacGillivray & E. B. Thomson (Dordrecht: Boston), p. 11
- Morgan, W. 1950, *Publ. Michigan Obs.*, 10, 33
- Morgan, W. W., Keenan, P. C., & Kellman, E. 1943, *An Atlas of Stellar Spectra, with an Outline of Spectral Classification*. (Chicago: Univ. Chicago Press)
- Murphy, D. C., Persson, S. E., Pahre, M. A., Sivaramakrishnan, A., & Djorgovski, S. G. 1995, *PASP*, 107, 1234
- Nakajima, T., Tsuji, T., Tamura, M., & Yamashita, T. 2000, *PASJ*, 52, 87
- Nakajima, T., Oppenheimer, B. R., Kulkarni, S. R., Golimowski, D. A., Matthews, K., & Durrance, S. T. 1995, *Nature*, 378, 463
- Noll, K. S., Geballe, T. R., Leggett, S. K., & Marley, M. S. 2000, *ApJ*, 541, L75
- Oke, J. B., et al. 1995, *PASP*, 107, 375
- Olivia, E., & Origlia, L. 1992, *A&A*, 254, 466
- Oppenheimer, B. R., Kulkarni, S. R., Matthews, K., van Kerkwijk, M. H. 1998, *ApJ*, 502, 932
- Oppenheimer, B. R., Kulkarni, S. R., Matthews, K., & Nakajima, T. 1995, *Science*, 270, 1478
- Pickering, E. C. 1890, *Harvard College Observ. Ann.*, 27, 1
- Rebolo, R., Zapatero Osorio, M. R., Madrugá, S., Béjar, V. J. S., Arribas, S., & Licandro, J. 1998, *Science*, 282, 1309
- Reid, I. N., Burgasser, A. J., Cruz, K., Kirkpatrick, J. D., & Gizis, J. E. 2001, *ApJ*, submitted
- Reid, I. N., Kirkpatrick, J. D., Gizis, J. E., Dahn, C. C., Monet, D. G., Williams, R. J., Liebert, J., & Burgasser, A. J. 2000, *AJ*, 119, 369
- Reid, I. N., et al. 1999, *ApJ*, 521, 613
- Reid, I. N., Hawley, S. L., & Gizis, J. E. 1995, *AJ*, 110, 1838
- Ruiz, M. T., Leggett, S. K., & Allard, F. 1997, *ApJ*, 491, L107

- Rudy, R. J., Erwin, P., Rossano, G. S., & Puetter, R. C. 1992, *ApJ*, 384, 536
- Saumon, D., Geballe, T. R., Leggett, S. K., Marley, M. S., Freedman, R. S., Lodders, K., Fegley, B., Jr., & Sengupta, S. K. 2000, *ApJ*, 541, 374
- Saumon, D., Chabrier, G., & Van Horn, H. M. 1995, *ApJS*, 99, 713
- Skrutskie, M. F., et al. 1997, in *The Impact of Large-Scale Near-IR Sky Surveys*, ed. F. Garzon (Dordrecht: Kluwer), p. 25
- Strauss, M. A., et al. 1999, *ApJ*, 522, L61
- Sykes, M. V., Cutri, R. M., Fowler, J. W., Tholen, D. J., Skrutskie, M. F., Price, S., & Tedesco, E. F. 2000, *Icarus*, 146, 161
- Testi, L., et al. 2001, *ApJ*, submitted
- Tokunaga, A. T. 2000, in *Allen’s Astrophysical Quantities, Fourth Edition*, ed. A. N. Cox (New York: Springer-Verlag), p. 151
- Tokunaga, A. T., & Kobayashi, N. 1999, *AJ*, 117, 1010
- Tsuji, T., Ohnaka, K., & Aoki, W. 1999, *ApJ*, 520, L119
- Tsuji, T., Ohnaka, K., & Aoki, W. 1996a, *A&A*, 305, L1
- Tsuji, T., Ohnaka, K., Aoki, W., & Nakajima, T. 1996b, *A&A*, 308, L29
- Tsvetanov, Z. I., et al. 2000, *ApJ*, 531, L61
- Wade, R. A., Hoessel, J. G., Elias, J. H., & Huchra, J. P. 1979, *PASP*, 91, 35
- Westphal, J. A., Matthews, K., & Terrile, R. J. 1974, *ApJ*, 188, L111
- Wiese, W. L., Smith, M. W., & Glennon, B. M. 1966, *Atomic Transition Probabilities*, Vol. 1. (Washington, D. C.: GPO)
- Wilson, J. C., Skrutskie, M. F., Colonno, M. R., Enos, A. T., Smith, J. D., Henderson, C. P., Gizis, J. E., Monet, D. G., & Houck, J. R. 2001a, *PASP*, 113, 227
- Wilson, J. C., et al. 2001b, *AJ*, submitted
- Wilson, J. C., et al. 2001c, *ApJ*, in preparation
- Wolf, C., et al. 1998, *A&A*, 338, 127
- York, D. G., et al. 2000, *AJ*, 120, 1579
- Zapatero Osorio, M. R., Béjar, V. J. S., Martín, E. L., Rebolo, R., Barrado y Navascuès, D., Bailer-Jones, C. A. L., & Mundt R. 2000, *Science*, 290, 103

Zapatero Osorio, M. R., Béjar, V. J. S., Rebolo, R., Martín, E. L., & Basri, G. 1999, ApJ, 524, L115

Fig. 1.— Near-infrared color-color diagram of objects detected by 2MASS. Small points are unresolved sources with $J < 15.8$, $H < 15.1$, and $K_s < 14.3$, selected within a 1° radius around 18^h R.A., 40° decl. Solid lines trace out the Bessell & Brett (1988) dwarf and giant tracks. L dwarf (triangles) and T dwarf (circles) colors are shown with error bars, based on 2MASS photometry. Colors for Gliese 229B (square) are taken from Leggett et al. (1999). The locations of S-, C-, and M-type asteroids are indicated by hash-marked boxes (Sykes et al. 2000). Dashed lines delineate the color constraints of the wdb0699 sample.

Fig. 2.— Aitoff projection map of sky area searched in wdb0699 sample. Light gray boxes map out areas scanned by 2MASS at the time of sample selection, covering 16620 sq. deg., while individual points mark the locations of the 35280 Cut # 1 candidates selected in this sample.

Fig. 3.— Ecliptic latitude distribution of 144 objects in the 2MASS IDR2, unconfirmed in near-infrared reimaging observations (thick line). These objects, with $J < 16$, $J-H < 0.3$, and $H-K_s < 0.3$, are not flagged as minor planets and are not associated with any catalogued asteroid within $25''$, based on ephemerides provided by D. Tholen. The distribution of 288 flagged minor planets and 25 missed associations (see Table 3) in the 2MASS IDR2 with the same magnitude and color constraints is overlain for comparison (thin line).

Fig. 4.— $1\text{--}2.5\ \mu\text{m}$ spectra of T dwarfs observed using the Keck I NIRC instrument. Spectra are normalized at their J-band peaks, offset by a constant (dotted lines), and ordered by increasing 1.15 and $1.6\ \mu\text{m}$ absorption. Major H_2O , CH_4 , CO , and FeH absorption bands are indicated, as are lines of K I (1.169 , 1.177 , 1.243 , and $1.252\ \mu\text{m}$) and the region of strongest CIA H_2 absorption. The L dwarfs 2MASS 0920+3517 (L6.5 V) and 2MASS 0825+2115 (L7.5 V) are shown for comparison.

Fig. 5.— $1.2\text{--}2.3\ \mu\text{m}$ spectrum of 2MASS 0755+2212 obtained in poor observing conditions using the Hale D78 near-infrared camera. Data are normalized at $1.27\ \mu\text{m}$. Identifying H_2O and CH_4 absorption bands are indicated.

Fig. 6.— $1\text{--}2.3\ \mu\text{m}$ spectra of objects observed using the CTIO 4m OSIRIS instrument. Data are normalized at $1.27\ \mu\text{m}$, offset by a constant (dotted lines), and sorted as in Figure 4. Bands of H_2O , CH_4 , CO , FeH , and CIA H_2 are indicated, as are lines of K I ($1.25\ \mu\text{m}$ doublet) and Na I ($2.2\ \mu\text{m}$ doublet). Ca I (1.314 , 2.26 , and $1.98\ \mu\text{m}$ triplets) and the $1.52\ \mu\text{m}$ K I doublet present in the spectrum of the M4.5 V LHS 511AB is also noted. Noisy regions around 1.4 and $1.9\ \mu\text{m}$ are due to telluric H_2O absorption.

Fig. 7.— OSIRIS data from 1.19 to $1.33\ \mu\text{m}$. Spectra are scaled and offset as in Figure 6. The $1.25\ \mu\text{m}$ K I doublet is indicated by dashed lines, and FeH features at 1.194 , 1.21 , and $1.237\ \mu\text{m}$, and the Ca I triplet at $1.314\ \mu\text{m}$ (present in LHS 511AB) are noted.

Fig. 8.— Comparison between NIRC (black lines) and OSIRIS data (gray lines) for the T dwarfs 2MASS 2254+3123, 2MASS 0559-1404, 2MASS 2356-1553, 2MASS 0937+2931, 2MASS 1553+1532,

and Gliese 570D.

Fig. 9.— Comparison between NIRC/OSIRIS data (gray lines) and data from the literature (black lines) for DENIS 0205-1159AB (L7 V) and the T dwarfs SDSS 1254-0122, 2MASS 0559-1404, SDSS 1346-0031, and SDSS 1624+0029.

Fig. 10.— Finder images for newly discovered T dwarfs. $5' \times 5'$ optical (R-band) and near-infrared (2MASS J- and K_s-band) images are shown, oriented with North up and East to the left. $10'' \times 10''$ boxes in each image highlight the positions of the identified T dwarfs.

Fig. 11.— Low resolution spectra of T dwarf standards and the L7 V DENIS 0205-1159AB. Data are normalized at their J-band peaks, and zero point offsets are indicated by dotted lines. Data for DENIS 0205-1159AB (Leggett et al. 2001), SDSS 0837-0000, SDSS 1254-0122, and SDSS 1021-0304 (Leggett et al. 2000) have been degraded to the resolution of the NIRC spectra using a Gaussian filter.

Fig. 12.— Near-infrared spectral indices for M, L, and T dwarfs versus spectral type. NIRC data are represented by diamonds, OSIRIS data by triangles, and CGS4 data (from the literature) by squares. Filled circles indicate measures for late-L and T dwarf standards. Long-dashed and short-dashed lines trace linear fits to indices in the T and late-M and L dwarf regimes, respectively. (a) H₂O indices; (b) CH₄ indices; (c) color indices; (d) CO, 2.11/2.07, and K shape indices.

Fig. 13.— Comparison of K1 and K2 indices from Tokunaga & Kobayashi (1999) for M (triangles), L (squares), and T dwarfs (circles). Filled symbols are data taken from NIRC, open symbols are CGS4 data from the literature. Representative M, L, and T dwarfs are labeled by their subtypes.

Fig. 14.— Values for H₂O^A and H₂O^B indices from Reid et al. (2001) versus spectral type. Symbols are those used in Figure 12. Short-dashed lines are the index/spectral type relations determined by Reid et al. (2001) for spectral types M8 V through L8 V, extended over the spectral range shown. The long-dashed line traces a linear fit to the H₂O^B indices for types M5 V through T8 V.

Fig. 15.— 1.2432 and 1.2522 μ m K I psuedo-equivalent width (PEW) measurements for late-M, L, and T dwarfs. OSIRIS data are indicated with triangles; CGS4 data from the literature are indicated by squares.

Fig. 16.— 2MASS colors for L and T dwarfs versus spectral type. Individual T dwarf colors with errors are indicated by open symbols, with upper limit detections indicated by downward arrows. Weighted averages at each half-subtype are indicated by slightly offset filled circles. L dwarf mean colors (with one-sigma scatter) are taken from Kirkpatrick et al. (2000).

Fig. 17.— Effective temperatures for late-type dwarfs. Temperatures for M and L dwarfs computed from bolometric corrections from Reid et al. (2001) are shown as squares. T_{eff} estimates from Leggett et al. (2001) are indicated by triangles. The two solid circles plot T_{eff} estimates for Gliese 229B (Saumon et al. 2000) and Gliese 570D (Burgasser et al. 2000a; Geballe et al. 2001a). Spectral

type/effective temperature scales from Kirkpatrick et al. (1999, 2000) and Basri et al. (2000) are indicated, with the latter scale corrected to the Kirkpatrick et al. (1999) spectral sequence. The dashed line shows a linear fit of T_{eff} for objects of type M9 V through L8 V, while the dot-dashed line traces a hypothetical T_{eff} scale from L8 V through T8 V.

Fig. 18.— The K-band spectrum of DENIS 0205-1159AB. Top panel shows opacity spectra of CH_4 (solid line), H_2O (dotted line), CO (dot-dashed line) and CIA H_2 (thick solid line) at $T = 1400$ K and $P = 1$ bar. Data for CH_4 , H_2O , and CO have been scaled to their chemical equilibrium number densities at this temperature and pressure (Burrows & Sharp 1999). The location of the $2.2 \mu\text{m}$ Na I doublet is also indicated. Bottom panel shows spectra of DENIS 0205-1159AB from Delfosse et al. (1997); Tokunaga & Kobayashi (1999); Leggett et al. (2001); and Reid et al. (2001). Data for SDSS 0539-0059 (L5 V) and SDSS 0837-0000 (T1 V) from Leggett et al. (2000) are also shown for comparison. Spectra are normalized at $2.15 \mu\text{m}$ (dotted lines) and offset. Arrows identify a possible weak CH_4 feature at $2.20 \mu\text{m}$.

Fig. 19.— The K-band spectrum of 2MASS 0937+2931. Top panel shows opacity spectra of CH_4 (solid line) and H_2O (dotted line) at $T = 1000$ K and $P = 1$ bar, and CIA H_2 opacity at $T = 1000$ K and $P = 1$ bar (thick solid line) and 10 bar (thick dashed line). CH_4 and H_2O data have been scaled as in Figure 18. Bottom panel shows spectra of 2MASS 0937+2931 (solid line) and the T6 V standard 2MASS 0243-2453 (dashed line). Both spectra have been normalized at their J-band peaks.

Table 1. 2MASS T Dwarf Search Samples.

Sample (1)	Mag. Cut (2)	Color Cuts (3)	Area (sq. deg.) (4)	Candidates (Cut #1) ^a (5)	Candidates (Cut #2) ^b (6)	Confirmed ^c (7)	Followed up ^d (8)	Identified T Dwarfs (9)
wdb0699	$J < 16$	$J-H < 0.3$ $H-K_s < 0.3$	16620	35280	404	93	67	14
rdb0400 ^e	$J < 16$	$J-H < 0.3$ $H-K_s \geq 0.3$	15315	15558	272	137	33	2
rdb0600 ^e	$J \leq 15$	$J-H \leq 0.4$ $H-K_s \leq 0.3$	4735	16560	138	9	5	1

^aInitial candidate pool from 2MASS catalogues.

^bNumber of candidates remaining after visual inspection of DSS images.

^cNumber of candidates remaining after near-infrared reimaging observations.

^dNumber of confirmed candidates with follow-up Gunn r-band imaging or near-infrared spectroscopy.

^eSubstantial follow-up remains for these samples.

Table 2. Log of Confirmation Imaging Observations.

UT Date (1)	Instrument (2)	# Observed All / (J-K _s < 0.5) (3)	% Confirmed All / (J-K _s < 0.5) (4)	Conditions (5)
1998 Oct 7-9	Palomar 60" IRCam	11 (10)	0.0 (0.0)	thin cirrus to clear
1999 Feb 23-27	Palomar 60" IRCam	6 (6)	16.7 (16.7)	clear to scattered clouds
1999 May 3	Palomar 60" IRCam	4 (2)	50.0 (0.0)	cirrus and fog
1999 May 27	Keck 10m NIRC	4 (4)	50.0 (50.0)	clear
1999 July 23-25	CTIO 1.5m CIRIM	194 (176)	7.2 (6.3)	clear to hazy
1999 Sept 22-25	Palomar 60" IRCam	83 (70)	37.3 (37.1)	fog to hazy
1999 Nov 19-21	Palomar 60" IRCam	4 (3)	0.0 (0.0)	thin clouds to cloudy
1999 Dec 17-19	CTIO 1.5m CIRIM	28 (22)	50.0 (36.4)	hazy to scattered clouds
2000 Jan 23-24	Keck 10m NIRC	5 (5)	0.0 (0.0)	clear and windy
2000 Apr 14-15	Palomar 60" IRCam	54 (45)	55.6 (57.8)	clear to low clouds and wind
2000 May 18-20	Palomar 60" IRCam	83 (8)	80.7 (25.0)	clear to fog and haze
2000 June 21-23	CTIO 1.5m OSIRIS	104 (45)	35.6 (15.6)	cloudy to clear
2000 Aug 18-20	CTIO 1.5m OSIRIS	26 (6)	53.8 (16.7)	light cirrus
2000 Oct 11-13	Palomar 60" IRCam	27 (5)	63.0 (40.0)	clear, high humidity
2001 Jan 5	Palomar 5m D78	1 (1)	100.0 (100.0)	cloudy
TOTAL		634 (408)	36.3 (21.3)	

Table 3. 2MASS IDR2 Sources Unconfirmed in Second Epoch Imaging (Partial).

Object ^a (1)	Date (UT) ^b (2)	2MASS J (3)	2MASS H (4)	2MASS K _s (5)	Instrument ^c (6)	Date (UT) (7)	Note ^d (8)
2MASSI J0004085-101237	1998 Oct 07	15.95±0.07	15.79±0.14	15.78±0.25	CTIO CIRIM	1999 Jul 24	
2MASSI J0006171-072119	1998 Oct 07	15.98±0.07	15.76±0.13	> 15.19	CTIO OSIRIS	2000 Aug 20	13''0 from 1998 QP104
2MASSI J0009296+163226	1997 Jul 12	15.84±0.07	15.32±0.09	15.52±0.22	CTIO CIRIM	1999 Jul 24	
2MASSI J0009332-111547	1998 Oct 16	15.27±0.05	15.02±0.09	15.00±0.14	CTIO CIRIM	1999 Jul 23	
2MASSI J0011144-043556	1998 Sep 17	15.24±0.04	14.94±0.06	14.69±0.10	CTIO CIRIM	1999 Jul 24	
2MASSI J0012248-020023	1998 Sep 17	12.94±0.03	12.59±0.03	12.49±0.03	CTIO OSIRIS	2000 Jun 21	10''3 from (927) Ratisbona
2MASSI J0012529-062929	1998 Oct 16	14.88±0.04	14.59±0.06	14.49±0.08	CTIO CIRIM	1999 Jul 24	11''0 from (2321) Luznice 1980 DB1
2MASSI J0014365-130605	1998 Jul 20	15.62±0.07	15.36±0.11	15.27±0.18	CTIO CIRIM	1999 Jul 24	
2MASSI J0014407-080107	1998 Oct 16	14.06±0.03	13.72±0.03	13.50±0.05	CTIO OSIRIS	2000 Jun 21	9''6 from (2132) Zhukov 1975 TW3
2MASSI J0015297+032103	1998 Oct 18	14.84±0.04	14.70±0.06	14.64±0.10	CTIO OSIRIS	2000 Jun 21	6''8 from (6046) 1991 RF14
⋮							

^aSource designations for 2MASS sources in the Incremental Release Catalogs are given as “2MASSI Jhhmmss[.]s±ddmmss’. The suffix conforms to IAU nomenclature convention and is the sexagesimal R.A. and decl. at J2000 equinox.

^bUT Date observed by 2MASS.

^cTelescope shorthand as follows: P60 = Palomar 60”, CTIO = Cerro Tololo 1.5m, and KECK = Keck 10m.

^dUnconfirmed objects near asteroid positions are likely missed associations due to errors in ephemerides. See text for discussion.

Table 4a. Log of NIRC Observations.

Object (1)	Type (2)	UT Date (3)	Int. (s) (4)	Airmass (5)	Calibrator (6)	Type ^a (7)
2MASS J0243–2453	T	2000 Jan 24	1080	1.41	HD 19378	G0 V
2MASS J0415–0935	T	1999 Nov 18	1080	1.21	SAO 150589	G5 V
2MASS J0415–0935	T	2000 Jan 24	1080	1.35	HD 22855	G3 V
2MASS J0559–1404	T	2000 Jan 23	1080	1.21	HD 41083	G2/3 V
2MASS J0559–1404	T	2000 Jan 24	1080	1.26	HD 41083	G2/3 V
2MASS J0727+1710	T	2000 Jan 23	1080	1.00	SAO 96796	G5 V
2MASS J0825+2115 ^b	L7.5 V	2000 Jan 23	1080	1.00	SAO 96796	G5 V
2MASS J0920+3517 ^b	L6.5 V	2000 Jan 24	1080	1.04	HD 73617	F5 V
2MASS J0937+2931	T	2000 Jan 23	1080	1.01	HD 76332	G2 V
2MASS J0937+2931	T	2000 Jan 24	1080	1.03	HD 76332	G2 V
2MASS J1047+2124	T	2000 Jan 23	1080	1.00	HD 98562	G2 V
2MASS J1047+2124	T	2000 Jan 24	1080	1.00	HD 98562	G2 V
2MASS J1217–0311	T	2000 Jan 23	1080	1.09	HD 108754	G7 V
2MASS J1237+6526	T	2000 Jan 24	1080	1.42	HD 110276	G0 V _w
SDSSp J1346–0031	T	2000 Jan 23	1080	1.07	HD 127913	G2 V
Gliese 570D	T	2000 Jan 24	1080	1.39	HD 126253	G0 V
2MASS J1553+1532	T	2000 Jul 22	900	1.15	HD 146759	G5 V
2MASS J2254+3123	T	2000 Jul 22	900	1.08	HD 219213	G5 V
2MASS J2339+1352	T	2000 Jul 22	900	1.08	HD 219213	G5 V
2MASS J2356–1553	T	1999 Nov 18	1080	1.28	HD 990	F5 V

^aSpectral types obtained from the SIMBAD database.

^bPreviously identified L dwarfs observed for spectral comparison.

Table 4b. Log of OSIRIS Observations.

Object (1)	Type (2)	UT Date (3)	Int. (s) (4)	Airmass (5)	Calibrator (6)	Type ^a (7)
DENIS J0205–1159 ^b	L7 V	2000 Jul 19	1250	1.07	HD 13406	A3 V _m
2MASS J0243–2453	T	1999 Dec 20	3600	1.04–1.15	HD 17168	A1 V
2MASS J0243–2453	T	1999 Dec 21	4200	1.01–1.09	HD 17168	A1 V
2MASS J0559–1404	T	1999 Dec 20	2400	1.05–1.09	HD 40972	A0 V
2MASS J0727+1710	T	1999 Dec 20	3600	1.52–1.72	HD 60275	A1 V
2MASS J0937+2931	T	1999 Dec 21	3000	1.98–2.00	HD 79248	A2 V
2MASS J1225–2739	T	2000 Jul 18	2500	1.16–1.24	HD 109142	A3 V _m
SDSSp J1254-0122	T	2000 Jul 16	4500	1.21–1.54	HD 112846	A3 V
Gliese 570D	T	2000 Jul 16	4500	1.09–1.30	HD 131992	A2/3 V
SDSSp J1624+0029	T	2000 Jul 15	3450	1.49–2.07	HD 148207	A0 V
2MASS J1534–2952	T	2000 Jul 18	2500	1.19–1.28	HD 139202	A1 V _m
2MASS J1546–3325	T	2000 Jul 19	3750	1.04–1.13	HD 140442	A1 V
2MASS J1553+1532	T	2000 Jul 17	3750	1.43–1.53	HD 143936	A0 V
2MASS J1553+1532	T	2000 Jul 18	2500	1.46–1.51	HD 143936	A0 V
HB 2115–4518 ^b	M8.5 V	2000 Jul 19	750	1.04	HD 203725	A0 III
HB 2124–4268 ^b	M7.5 V	2000 Jul 19	750	1.02	HD 203725	A0 III
LHS 511AB ^b	M4.5 V	2000 Jul 19	75	1.08	HD 205178	A0 V
2MASS J2224–0158 ^b	L4.5 V	2000 Jul 19	1250	1.15	HD 212417	A3 V
2MASS J2254+3123	T	2000 Jul 16	3750	2.10–2.20	HD 216716	A0 V
2MASS J2339+1352	T	2000 Jul 16	2500	1.44–1.51	HD 222250	A3 V
2MASS J2356–1553	T	1999 Dec 20	1800	1.27–1.37	HD 4065	A0 V
2MASS J2356–1553	T	2000 Jul 17	5000	1.04–1.15	HD 223785	A1 V

^aSpectral types obtained from the SIMBAD database.

^bPreviously identified M and L dwarfs observed for spectral comparison.

Table 5. Comparison of NIRC Spectrophotometric Colors to 2MASS Photometry.

Object (1)	2MASS J-H			2MASS H-K _s			2MASS J-K _s		
	Phot. (2)	Spec. (3)	δ^a (4)	Phot. (5)	Spec. (6)	δ^a (7)	Phot. (8)	Spec. (9)	δ^a (10)
2MASS J0243–2453	0.25±0.11	0.10	0.15	−0.06±0.20	0.15	−0.21	0.19±0.18	0.25	−0.06
2MASS J0415–0935 ^b	0.14±0.13	0.12	0.02	0.12±0.23	0.21	−0.09	0.26±0.21	0.33	−0.07
2MASS J0415–0935 ^b	0.14±0.13	0.12	0.02	0.12±0.23	−0.04	0.16	0.26±0.21	0.08	0.18
2MASS J0559–1404 ^b	0.14±0.05	0.25	−0.11	0.07±0.06	0.18	−0.11	0.21±0.06	0.43	−0.22
2MASS J0559–1404 ^b	0.14±0.05	0.26	−0.12	0.07±0.06	0.34	−0.27	0.21±0.06	0.60	−0.39
2MASS J0727+1710	−0.27±0.19	−0.15	−0.12	0.26±0.28	0.05	0.21	−0.01±0.22	−0.10	0.09
2MASS J0825+2115	1.33±0.06	0.98	0.35	0.74±0.06	0.77	−0.03	2.07±0.06	1.75	0.32
2MASS J0920+3517	0.93±0.10	0.85	0.08	0.73±0.11	0.68	0.05	1.66±0.11	1.52	0.14
2MASS J0937+2931 ^b	−0.03±0.08	0.15	−0.18	−0.86±0.25	−0.30	−0.56	−0.89±0.24	−0.16	−0.73
2MASS J0937+2931 ^b	−0.03±0.08	0.02	−0.05	−0.86±0.25	−0.49	−0.37	−0.89±0.24	−0.48	−0.41
2MASS J1047+2124 ^b	0.03±0.13	0.15	−0.12	< −0.50	−0.22	–	< −0.47	−0.06	–
2MASS J1047+2124 ^b	0.03±0.13	0.19	−0.16	< −0.50	−0.22	–	< −0.47	−0.02	–
2MASS J1217–0311	0.06±0.14	0.01	0.05	< −0.12	0.23	–	< −0.06	0.24	–
2MASS J1237+6526	0.31±0.18	0.00	0.31	< −0.18	−0.41	–	< 0.13	−0.41	–
SDSSp J1346–0031	−0.19±0.22	0.02	−0.21	< 0.30	0.15	–	< 0.11	0.17	–
Gliese 570D	0.05±0.10	0.09	−0.04	0.01±0.19	−0.01	0.02	0.06±0.18	0.07	−0.01
2MASS J1553+1532	−0.11±0.19	0.14	−0.25	0.41±0.25	0.05	0.36	0.30±0.21	0.19	0.11
2MASS J2254+3123	0.24±0.10	0.20	0.04	0.21±0.17	−0.09	0.30	0.45±0.15	0.11	0.34
2MASS J2339+1352	−0.16±0.19	0.12	−0.28	0.34±0.33	−0.08	0.42	0.18±0.29	0.04	0.14
2MASS J2356–1553	0.16±0.12	0.18	−0.02	−0.19±0.21	0.12	−0.31	−0.03±0.20	0.30	−0.33

^a $\delta \equiv$ photometry minus spectrophotometry.

^bSeparate observations obtained on 2000 January 23-24 (UT).

Table 6. New T Dwarfs Identified in the 2MASS Catalog.

2MASS Designation	Primary Sample ^a	2MASS J	2MASS H	2MASS K _s
2MASSI J0243137–245329	wdb0699	15.40±0.05	15.15±0.10	15.21±0.17
2MASSI J0415195–093506	wdb0699	15.71±0.06	15.57±0.12	15.45±0.20
2MASSI J0727182+171001	wdb0699	15.55±0.07	15.82±0.18	15.56±0.21
2MASSI J0755480+221218	wdb0699	15.72±0.07	15.66±0.14	15.77±0.21
2MASSI J0937347+293142	wdb0699	14.65±0.04	14.68±0.07	15.54±0.24
2MASSI J1534498–295227	wdb0699	14.90±0.04	14.89±0.09	14.86±0.11
2MASSI J1546271–332511	wdb0699	15.60±0.05	15.44±0.09	15.42±0.17
2MASSI J1553022+153236	rdb0400	15.81±0.08	15.92±0.17	15.51±0.19
2MASSI J2254188+312349	wdb0699	15.28±0.05	15.04±0.09	14.83±0.14
2MASSI J2339101+135230	rdb0400	15.88±0.08	16.04±0.17	15.70±0.28
2MASSI J2356547–155310	wdb0699	15.80±0.06	15.64±0.10	15.83±0.19

^aSome objects found in multiple samples due to overlapping search criteria.

Table 7. Known T Dwarfs.

Object (1)	Type (2)	J ^a (3)	J–H ^a (4)	H–K _s ^a (5)	J–K _s ^a (6)	Ref. (7)
2MASS J0243137–245329	T6 V	15.40±0.05	0.25±0.11	–0.06±0.20	0.19±0.18	1
2MASS J0415195–093506	T8 V	15.71±0.06	0.14±0.13	0.12±0.23	0.26±0.21	1
2MASS J0559191–140448	T5 V	13.82±0.03	0.14±0.05	0.07±0.06	0.21±0.06	2
Gliese 229B	T6.5 V	14.32±0.05 ^b	–0.03±0.07 ^b	–0.10±0.07 ^b	–0.13±0.07 ^b	3
2MASS J0727182+171001	T7 V	15.55±0.07	–0.27±0.19	0.26±0.28	–0.01±0.22	1
2MASS J0755480+221218	T5 V:	15.72±0.07	0.06±0.16	–0.11±0.25	–0.05±0.22	1
SDSSp J083717.22–000018.3	T1 V	17.23±0.25	1.25±0.30	< 0.33	< 1.58	4
2MASS J0937347+293142	T6 Vp	14.65±0.04	–0.03±0.08	–0.86±0.25	–0.89±0.24	1
SDSSp J102109.69–030420.1	T3 V	16.26±0.10	0.93±0.15	0.23±0.20	1.16±0.20	4
2MASS J1047538+212423	T6.5 V	15.82±0.06	0.03±0.13	< –0.50	< –0.47	5
NTTDF 1205–0744	T6 V:	20.15 ^c	–	–	–0.15 ^c	6
2MASS J1217110–031113	T7.5 V	15.85±0.07	0.06±0.14	< –0.12	< –0.06	5
2MASS J1225543–273946	T6 V	15.23±0.05	0.13±0.09	0.04±0.17	0.17±0.16	5
2MASS J1237392+652615	T6.5 V	16.03±0.09	0.31±0.18	< –0.18	< 0.13	5
SDSSp J125453.90–012247.4	T2 V	14.88±0.03	0.84±0.05	0.21±0.07	1.05±0.07	4
SDSSp J134646.45–003150.4	T6 V	15.86±0.08	–0.19±0.22	< 0.30	< 0.11	7
Gliese 570D	T8 V	15.33±0.05	0.05±0.10	0.01±0.19	0.06±0.18	8
2MASS J1534498–295227	T5.5 V	14.90±0.04	0.01±0.10	0.03±0.14	0.04±0.12	1
2MASS J1546271–332511	T5.5 V	15.60±0.05	0.16±0.10	0.02±0.19	0.18±0.18	1
2MASS J1553022+153236	T7 V	15.81±0.08	–0.11±0.19	0.41±0.25	0.30±0.21	1
SDSSp J162414.37+002915.6	T6 V	15.49±0.06	–0.03±0.12	< 0.08	< 0.05	9
2MASS J2254188+312349	T5 V	15.28±0.05	0.24±0.10	0.21±0.17	0.45±0.15	1
2MASS J2339101+135230	T5.5 V	15.88±0.08	–0.16±0.19	0.34±0.33	0.18±0.29	1
2MASS J2356547–155310	T6 V	15.80±0.06	0.16±0.12	–0.19±0.21	–0.03±0.20	1

^a2MASS photometry unless otherwise noted.

^bUKIRT JHK photometry from Leggett et al. (1999).

^cJK photometry from Cuby et al. (1999).

References. — (1) This paper; (2) Burgasser et al. (2000b); (3) Nakajima et al. (1995); (4) Leggett et al. (2000); (5) Burgasser et al. (1999); (6) Cuby et al. (1999); (7) Tsvetanov et al. (2000); (8) Burgasser et al. (2000a); (9) Strauss et al. (1999).

Table 8. Near-Infrared Spectral Properties of T Dwarf Subtypes.

Type (1)	Description (2)	Standard (3)
T1 V	Weak CH ₄ bands seen at 1.3, 1.6, and 2.2 μm Distinct 1.07 and 1.27 μm peaks separated by 1.15 μm H ₂ O/CH ₄ feature K-band peak noticeably depressed relative to J and H CH ₄ and CO bands at K equal in strength K I lines at 1.25 μm strong	SDSS 0837-0000
T2 V	CH ₄ bands strengthening Flux at 1.15 μm feature roughly 50% J-band peak K-band CH ₄ stronger than CO K-band peak rounded	SDSS 1254-0122
T3 V	Flux at 1.15 μm feature roughly 40% J-band peak Flux at 1.6 μm feature roughly 60% H-band peak CO barely visible at K-band	SDSS 1021-0304
T5 V	Flux at 1.6 μm trough roughly 50% H-band peak No CO present H-band suppressed relative to J and K K I lines at 1.25 μm peak in strength	2MASS 0559-1404
T6 V	Flux at 1.15 μm feature roughly 20% J-band peak Flux at 1.6 μm feature roughly 30% H-band peak 1.25 μm K I lines beginning to weaken 1.3 μm CH ₄ band blended with 1.4 μm H ₂ O 2.2 μm CH ₄ absorption nearly saturated K-band beginning to flatten, asymmetric peak centered at 2.11 μm	2MASS 0243-2453
T7 V	Flux at 1.15 μm feature roughly 10% J-band peak Flux at 1.6 μm feature roughly 10% H-band peak 1.25 μm K I lines barely discernible H- and K-band peaks maximally suppressed relative to J J-band peak increasingly narrow	2MASS 0727+1710
T8 V	Flux at 1.15 μm feature nearly saturated Flux at 1.6 μm feature nearly saturated No 1.25 μm K I lines present Slight increase in H- and K-band peaks relative to J K-band peak more sharply peaked and symmetric about 2.07 μm	2MASS 0415-0935

Table 9. Ratios Used as T Dwarf Spectral Diagnostics.

Diagnostic (1)	Numerator (μm) (2)	Denominator (μm) (3)	Feature Measured (4)
H ₂ O-A ^a	$\langle F_{1.12-1.17} \rangle$	$\langle F_{1.25-1.28} \rangle$	1.15 μm H ₂ O/CH ₄
H ₂ O-B ^a	$\langle F_{1.505-1.525} \rangle$	$\langle F_{1.575-1.595} \rangle$	1.4 μm H ₂ O
H ₂ O-C	$\langle F_{2.00-2.04} \rangle$	$\langle F_{2.09-2.13} \rangle$	1.9 μm H ₂ O
CH ₄ -A ^a	$\langle F_{1.295-1.325} \rangle$	$\langle F_{1.25-1.28} \rangle$	1.3 μm CH ₄
CH ₄ -B ^a	$\langle F_{1.64-1.70} \rangle$	$\langle F_{1.575-1.595} \rangle$	1.6 μm CH ₄
CH ₄ -C ^a	$\langle F_{2.225-2.275} \rangle$	$\langle F_{2.09-2.13} \rangle$	2.2 μm CH ₄
H/J ^a	$\langle F_{1.50-1.75} \rangle$	$\langle F_{1.20-1.325} \rangle$	NIR color
K/J ^a	$\langle F_{2.00-2.30} \rangle$	$\langle F_{1.20-1.325} \rangle$	NIR color
K/H	$\langle F_{2.00-2.30} \rangle$	$\langle F_{1.50-1.75} \rangle$	NIR color
CO	$\langle F_{2.325-2.375} \rangle$	$\langle F_{2.09-2.13} \rangle$	2.3 μm CO
2.11/2.07 ^a	$\langle F_{2.10-2.12} \rangle$	$\langle F_{2.06-2.08} \rangle$	K-band shape/CIA H ₂
K shape	$\langle F_{2.12-2.13} \rangle - \langle F_{2.15-2.16} \rangle$	$\langle F_{2.17-2.18} \rangle - \langle F_{2.19-2.20} \rangle$	K-band shape/CIA H ₂

^aSpectral ratio used as a classification diagnostic.

Table 10. Spectral Diagnostics for L and T Dwarf Standards.

Object (1)	Type (2)	H ₂ O-A (3)	H ₂ O-B (4)	CH ₄ -A (5)	CH ₄ -B (6)	CH ₄ -C (7)	H/J (8)	K/J (9)	2.11/2.07 (10)
DENIS 1228–1547	L5 V	0.765	0.771	1.044	1.035	0.938	0.891	0.575	1.102
DENIS 0205–1159	L7 V	0.764	0.760	1.026	1.010	0.841	0.837	0.524	1.079
SDSS 0837–0000	T1 V	0.669	0.637	0.991	0.920	0.662	0.746	0.326	1.061
SDSS 1254–0122	T2 V	0.501	0.569	0.910	0.832	0.527	0.637	0.299	1.081
SDSS 1021–0304	T3 V	0.393	0.518	0.864	0.657	0.498	0.581	0.250	1.068
2MASS 0559–1404 ^a	T5 V	0.351	0.450	0.786	0.464	0.210	0.380	0.185	0.999
2MASS 0243–2453	T6 V	0.174	0.353	0.555	0.292	0.139	0.310	0.136	0.902
2MASS 0727+1710	T7 V	0.117	0.296	0.498	0.176	0.087	0.241	0.097	0.864
2MASS 0415–0935 ^a	T8 V	0.062	0.228	0.407	0.102	0.071	0.301	0.127	0.825

^aIndices averaged from multiple spectra.

Table 11a. T Dwarf Spectral Indices: NIRC and D78 Data.

Object (1)	H ₂ O-A (2)	H ₂ O-B (3)	CH ₄ -A (4)	CH ₄ -B (5)	CH ₄ -C ^a (6)	H/J ^a (7)	K/J ^a (8)	2.11/2.07 (9)	Type (10)
2MASS 2254+3123	0.442(2–3)	0.496(3–5)	0.721(5)	0.513(5)	0.243(5)	0.378(5)	0.133(6)	0.965(5)	4.8±0.4
2MASS 0559–1404 ^b	0.351(5)	0.450(5)	0.786(5)	0.464(5)	0.210(5)	0.380(5)	0.185(5)	0.999(5)	5.0±0.0
2MASS 2339+1352	0.300(5)	0.418(5)	0.547(6)	0.388(5–6)	0.182(5)	0.337(6)	0.119(6–7)	0.990(5)	5.4±0.5
2MASS 0755+2212	–	0.548(2–3)	0.758(5)	0.450(5)	–	0.327(6)	0.159(5–6)	–	5.2: ^c
2MASS 2356–1553	0.261(5–6)	0.389(6)	0.720(5)	0.322(6)	0.140(6)	0.351(5–6)	0.150(6)	0.946(6)	5.8±0.4
2MASS 0937+2931 ^b	0.185(6)	0.410(5–6)	0.602(6)	0.287(6)	0.199(5)	0.314(6)	0.082(7)	0.920(6)	5.9±0.2
2MASS 0243–2453	0.174(6)	0.353(6)	0.555(6)	0.292(6)	0.139(6)	0.310(6)	0.136(6)	0.902(6)	6.0±0.0
SDSS 1346–0031	0.157(6)	0.354(6)	0.561(6)	0.240(6–7)	0.145(6)	0.286(6)	0.125(6)	0.900(6)	6.0±0.0
2MASS 1047+2124 ^b	0.166(6)	0.345(6)	0.524(7)	0.235(6–7)	0.170(6)	0.339(6)	0.105(7)	0.884(6–7)	6.3±0.4
2MASS 1237+6526	0.127(7)	0.328(6–7)	0.511(7)	0.221(7)	0.144(6)	0.284(6)	0.073(7)	0.902(6)	6.6±0.5
2MASS 0727+1710	0.117(7)	0.296(7)	0.498(7)	0.176(7)	0.087(≥ 7)	0.241(≥ 7)	0.097(≥ 7)	0.864(7)	7.0±0.0
2MASS 1553+1532	0.130(7)	0.311(7)	0.444(8)	0.175(7)	0.078(≥ 7)	0.317(≥ 7)	0.128(≥ 7)	0.864(7)	7.0±0.0
2MASS 1217–0311	0.091(7–8)	0.292(7)	0.412(8)	0.138(7–8)	0.074(≥ 7)	0.276(≥ 7)	0.132(≥ 7)	0.817(8)	7.7±0.2
Gliese 570D	0.080(8)	0.242(8)	0.441(8)	0.135(7–8)	0.063(≥ 7)	0.293(≥ 7)	0.110(≥ 7)	0.938(6)	7.8±0.3
2MASS 0415–0935 ^b	0.062(8)	0.228(8)	0.407(8)	0.102(8)	0.071(≥ 7)	0.301(≥ 7)	0.127(≥ 7)	0.825(8)	8.0±0.0

^aIndex ambiguous for subtypes T7 V through T8 V.^bIndices averaged from multiple spectra.^cSpectral type uncertain due to poor quality of D78 spectrum.

Table 11b. T Dwarf Spectral Indices: OSIRIS Data.

Object (1)	H ₂ O-B (2)	CH ₄ -A (3)	CH ₄ -B (4)	H/J ^a (5)	K/J ^a (6)	Type (7)
SDSS 1254–0122	0.558(2)	0.943(2)	0.825(2)	0.680(2)	0.344(1)	2.0±0.0
2MASS 2254+3123	0.469(5)	0.886(2–3)	0.484(5)	0.410(5)	0.184(5)	5.0±0.0
2MASS 0559–1404	0.456(5)	0.811(5)	0.383(5–6)	0.337(5–6)	0.153(5–6)	5.3±0.3
2MASS 2339+1352	0.456(5)	0.756(5)	0.344(6)	0.266(7)	0.176(5)	5.3: ^b
2MASS 1534–2952	0.441(5)	0.824(3–5)	0.380(5–6)	0.305(6)	0.103(7)	5.5±0.4
2MASS 1546–3325	0.418(5)	0.788(5)	0.283(6)	0.297(6)	0.134(6)	5.7±0.6
2MASS 2356–1553	0.409(5–6)	0.795(5)	0.254(6)	0.297(6)	0.153(6)	5.8±0.3
2MASS 0937+2931	0.388(6)	0.710(5)	0.246(6)	0.282(6)	0.147(6)	6.0±0.0
2MASS 0243–2453	0.328(6)	0.605(6)	0.225(7)	0.277(6)	0.205(5)	6.0±0.0
2MASS 1225–2739	0.403(5–6)	0.745(5)	0.262(6)	0.264(7)	0.110(7)	6.2±0.8
SDSS 1624+0029	0.230(8)	0.739(5)	0.188(7)	0.235(7)	0.057(7)	7.0: ^b
2MASS 0727+1710	0.332(6)	0.511(7)	0.133(8)	0.183(7)	0.137(≥ 7)	7.0±0.0
2MASS 1553+1532 ^c	0.300(7)	0.601(6)	0.114(8)	0.250(7)	0.109(≥ 7)	7.0±0.0
Gliese 570D	0.294(7)	0.537(6)	0.106(8)	0.261(7)	0.111(≥ 7)	7.0±0.0

^aIndex ambiguous for subtypes T7 V through T8 V.

^bSpectral type uncertain due to poor quality spectrum.

^cIndices averaged from multiple spectra.

Table 11c. T Dwarf Spectral Indices: Data from Literature.

Object (1)	Ref. (2)	H ₂ O-A (3)	H ₂ O-B (4)	CH ₄ -A (5)	CH ₄ -B (6)	CH ₄ -C (7)	H/J (8)	K/J (9)	2.11/2.07 ^a (10)	Type (11)
SDSS 0837–0000	1	0.669(1)	0.637(1)	0.991(1)	0.920(1)	0.662(1)	0.746(1)	0.326(1)	1.061(≤ 3)	1.0 \pm 0.0
SDSS 1254–0122	1	0.501(2)	0.569(2)	0.910(2)	0.832(2)	0.527(2)	0.637(2)	0.299(2)	1.081(≤ 3)	2.0 \pm 0.0
SDSS 1021–0304	1	0.393(3)	0.518(3)	0.864(3)	0.657(3)	0.498(3)	0.581(3)	0.250(3)	1.068(≤ 3)	3.0 \pm 0.0
2MASS 0559–1404	2	0.350(5)	0.494(3–5)	0.862(3)	0.470(5)	0.232(6–7)	0.377(6)	0.127(7)	1.001(5)	5.3 \pm 0.9
SDSS 1624+0029	3	0.167(6)	0.371(6)	0.703(5)	0.280(6)	0.150(6)	0.279(6–7)	0.099(7)	0.937(6)	6.1 \pm 0.2
SDSS 1346–0031	5	0.175(6)	0.352(6)	0.635(6)	0.247(6)	0.094(7)	0.261(7)	0.113(6–7)	0.937(6)	6.3 \pm 0.4
NTTDF 1205–0744	4	0.087(7–8)	0.289(7)	0.723(5)	0.229(6–7)	0.261(5)	0.279(6–7)	0.117(6–7)	0.913(6)	6.3: ^b
Gliese 229B ^c	6,7	0.114(7)	0.425(5–6)	0.485(7)	0.200(7)	0.195(5)	0.277(6–7)	0.100(7)	0.926(6)	6.5 \pm 0.6

^aIndex ambiguous for subtypes T1 V through T3 V.

^bSpectral type uncertain due to poor quality spectrum.

^cIndices averaged from multiple spectra.

References. — (1) Leggett et al. (2000); (2) Burgasser et al. (2000c); (3) Strauss et al. (1999); (4) Cuby et al. (1999); (5) Tsvetanov et al. (2000); (6) Geballe et al. (1996); (7) Oppenheimer et al. (1998).

Table 12a. Linear Fits to Spectral Indices: T Dwarfs^a

Index (1)	c0 (2)	c1 (3)	Range (4)	RMS Error (SpT) ^b (5)
H ₂ O-A	8.5±2.8	-11.9±0.9	T1 V – T8 V	0.6
H ₂ O-B	12.9±3.1	-18.2±1.4	T1 V – T8 V	0.7
CH ₄ -A	13.2±3.9	-11.3±1.1	T1 V – T8 V	0.9
CH ₄ -B	8.3±1.5	-8.0±0.3	T1 V – T8 V	0.4
CH ₄ -C	8.2±2.4	-12.0±0.8	T1 V – T8 V	0.5
H/J	9.7±2.3	-12.0±0.7	T1 V – T7 V	0.5
K/J	9.0±3.4	-23.9±2.2	T1 V – T7 V	0.7
2.11/2.07	24.0±10.0	-19.1±3.8	T3 V – T8 V	1.2

^aCoefficients are for linear fit $\text{SpT} = c0 + c1 \times \text{Index}$, where $\text{SpT}(\text{T0}) = 0$, $\text{SpT}(\text{T5}) = 5$, $\text{SpT}(\text{L5}) = -4$, etc.

^bRMS of SpT minus adopted spectral type, the latter quantity from the literature or listed in Table 7.

Table 12b. Linear Fits to Spectral Indices: M and L Dwarfs^a

Index (1)	c0 (2)	c1 (3)	Range (4)	RMS Error (SpT) ^b (5)
H ₂ O-A	37.7±7.0	−41.0±5.8	M5 V – L7 V	2.5
H ₂ O-B	47.7±4.6	−53.9±4.2	M5 V – L7 V	1.7
H ₂ O-C	57.8±8.1	−65.5±7.7	M5 V – L7 V	2.2
CH ₄ -C	20.8±2.7	−17.1±1.3	L3 V – T3 V	0.8
H/J	−32.7±4.6	43.9±7.8	M5 V – L7 V	3.9
K/J	−18.3±2.5	40.4±6.8	M5 V – L7 V	3.6
K/H	−30.7±8.0	68.2±16.4	M5 V – L7 V	5.3

^aCoefficients are for linear fit $\text{SpT} = c0 + c1 \times \text{Index}$, where $\text{SpT}(\text{L0}) = 0$, $\text{SpT}(\text{L5}) = 5$, $\text{SpT}(\text{M5}) = -5$, etc.

^bRMS of SpT minus adopted spectral type, the latter quantity from the literature.

Table 13a. K I Pseudo-equivalent Widths - OSIRIS Data

Object (1)	Type (2)	1.2432 μm		1.2522 μm	
		λ_c (μm) (3)	PEW (\AA) (4)	λ_c (μm) (5)	PEW (\AA) (6)
LHS 511AB	M4.5 V	1.2425	1.50 \pm 0.15	1.2514	1.50 \pm 0.12
HB 2115–4518	M7.5 V	1.2433	8.1 \pm 0.7	1.2518	4.3 \pm 0.7
HB 2124–4228	M8.5 V	1.2429	9.2 \pm 0.7	1.2518	5.6 \pm 0.8
2MASS 2224–0158	L4.5 V	1.2425	8.6 \pm 0.9	1.2513	6.9 \pm 0.9
DENIS 0205–1159	L7 V	1.2433	3.3 \pm 0.8	1.2522	6.2 \pm 0.7
SDSS 1254–0122	T2 V	1.2433	5.5 \pm 0.9	1.2521	9.1 \pm 0.9
2MASS 2254+3123	T5 V	1.2434	7.5 \pm 1.4	1.2527	10.6 \pm 1.3
2MASS 0559–1404	T5 V	1.2423	6.4 \pm 1.0	1.2515	9.3 \pm 0.9
2MASS 1534–2952	T5.5 V	1.2432	5.9 \pm 0.6	1.2521	7.7 \pm 0.6
2MASS 2339+1352	T5.5 V	1.2405	< 3.2	1.2516	7.4 \pm 3.5
2MASS 1546–3325	T5.5 V	1.2427	5.9 \pm 1.3	1.2528	11.1 \pm 1.2
2MASS 2356–1553	T6 V	1.2427	4.1 \pm 1.4	1.2506	11.7 \pm 1.1
2MASS 0243–2453	T6 V	1.2430	4.2 \pm 1.0	1.2523	8.9 \pm 1.2
2MASS 0937+2931	T6 V	1.2407	< 1.3	1.2508	2.5 \pm 1.2
2MASS 1225–2739	T6 V	1.2436	6.6 \pm 1.1	1.2524	7.8 \pm 0.6
SDSS 1624+0029	T6 V	1.2429	3.4 \pm 1.8	1.2517	9.8 \pm 1.8
2MASS 0727+1710	T7 V	1.2428	1.9 \pm 1.2	1.2516	6.8 \pm 1.0
2MASS 1553+1532	T7 V	1.2430	2.9 \pm 1.0	1.2519	5.8 \pm 0.9
2MASS 1553+1532	T7 V	1.2425	1.5 \pm 1.1	1.2522	5.7 \pm 1.1
Gliese 570D	T8 V	1.2411	3.7 \pm 0.7	1.2491	3.0 \pm 0.5

Table 13b. K I Pseudo-equivalent Widths - Data from the Literature

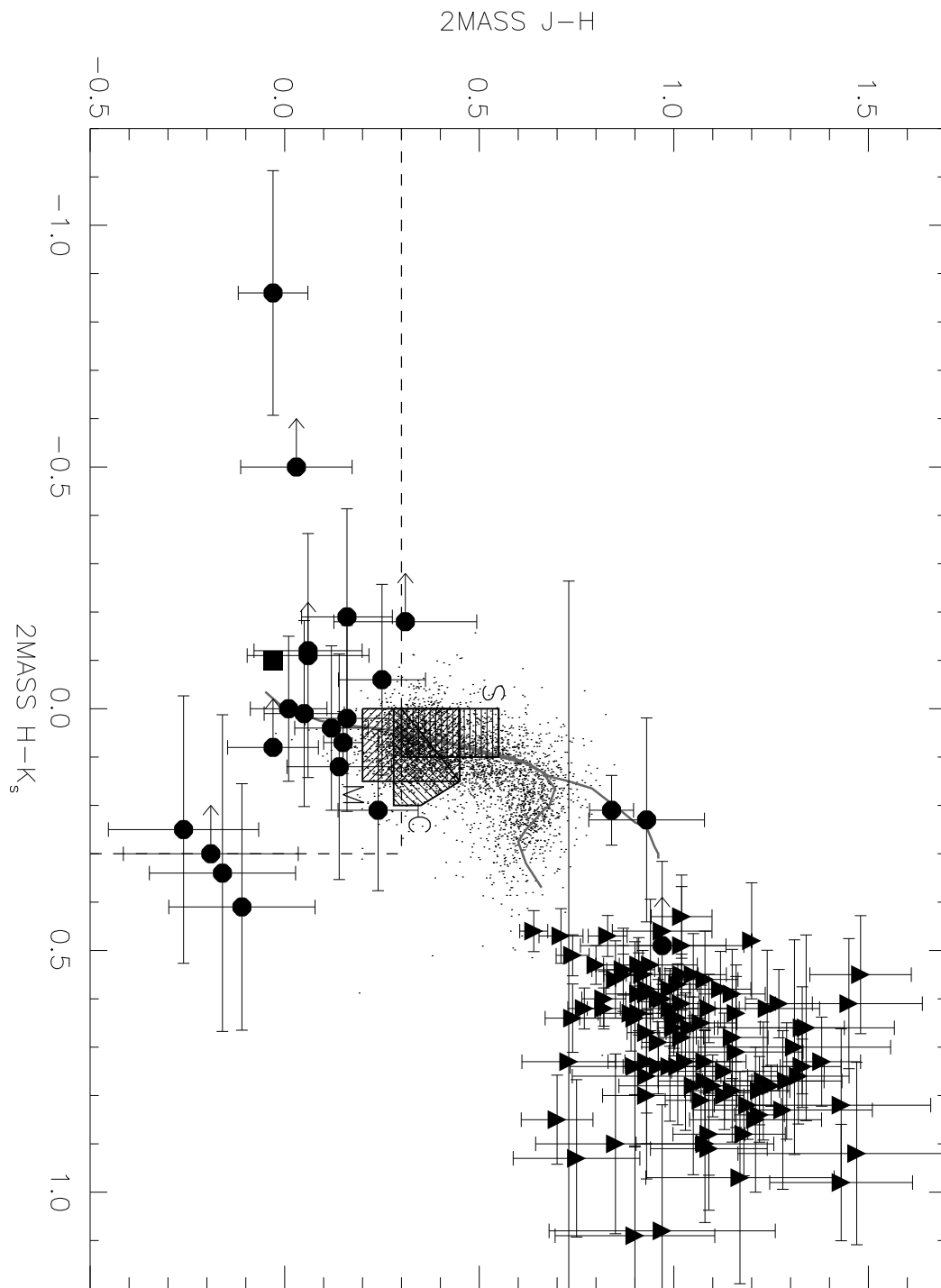
Object (1)	Type (2)	1.2432 μm		1.2522 μm		Ref.
		λ_c (μm) (3)	PEW (\AA) (4)	λ_c (μm) (5)	PEW (\AA) (6)	
LHS 3406	M5.5 V	1.2416	5.1 \pm 0.9	1.2503	4.2 \pm 0.2	1
LHS 2930	M6.5 V	1.2404	4.5 \pm 1.1	1.2503	2.9 \pm 0.5	1
LHS 3003	M7 V	1.2404	4.2 \pm 0.9	1.2503	2.0 \pm 0.4	1
LHS 429	M7 V	1.2404	4.0 \pm 0.7	1.2503	1.8 \pm 0.4	1
LHD 94	M7 V	1.2434	5.4 \pm 0.6	1.2519	4.3 \pm 0.7	2
2MASS 0320+1854	M8 V	1.2438	7.2 \pm 0.3	1.2524	4.3 \pm 0.4	2
TVLM 513–46546	M8.5 V	1.2436	9.0 \pm 0.4	1.2528	6.2 \pm 0.3	1
BRI 0021–0214	M9.5 V	1.2432	9.0 \pm 0.6	1.2525	5.2 \pm 0.5	1
2MASS 0345+2540	L0 V	1.2435	8.0 \pm 0.5	1.2522	6.1 \pm 0.3	1
2MASS 0345+2540	L0 V	1.2438	8.0 \pm 0.6	1.2525	6.2 \pm 0.5	2
2MASS 0746+2000	L0.5 V	1.2436	9.3 \pm 0.4	1.2522	6.8 \pm 0.3	2
2MASS 0829+1456	L2 V	1.2431	11.2 \pm 1.8	1.2518	6.9 \pm 0.6	2
Kelu 1	L2 V	1.2435	9.8 \pm 0.5	1.2527	6.6 \pm 0.3	1
2MASS 1029+1626	L2.5 V	1.2422	8.2 \pm 1.5	1.2513	5.0 \pm 0.8	2
DENIS 1058–1548	L3 V	1.2434	11.6 \pm 0.5	1.2521	8.4 \pm 0.6	1
2MASS 0036+1821	L3.5 V	1.2435	10.1 \pm 0.5	1.2522	9.4 \pm 0.4	2
GD 165B	L4 V	1.2436	12.5 \pm 0.7	1.2522	6.3 \pm 0.4	1
2MASS 1112+3548	L4.5 V	1.2439	9.2 \pm 1.0	1.2518	5.2 \pm 1.2	2
DENIS 1228–1547	L5 V	1.2431	9.4 \pm 0.9	1.2525	7.8 \pm 0.8	1
SDSS 0539–0059	L5 V	1.2440	8.1 \pm 0.6	1.2527	7.3 \pm 0.5	3
DENIS 0205–1159	L7 V	1.2435	4.9 \pm 1.0	1.2529	5.3 \pm 0.4	1
DENIS 0205–1159	L7 V	1.2435	< 1.0	1.2516	6.2 \pm 1.7	2
2MASS 0825+2115	L7.5 V	1.2424	4.1 \pm 1.9	1.2522	4.6 \pm 1.0	2
2MASS 0310+1648	L8 V	1.2439	< 1.8	1.2532	7.1 \pm 1.5	2
SDSS 0837–0000	T1 V	1.2430	3.4 \pm 1.2	1.2517	3.2 \pm 1.4	3
SDSS 1254–0122	T2 V	1.2460	3.5 \pm 0.5	1.2517	7.2 \pm 0.6	3
SDSS 1021–0304	T3 V	1.2430	4.7 \pm 0.5	1.2517	7.8 \pm 0.4	3
SDSS 1346–0031	T6 V	1.2429	2.9 \pm 1.1	1.2516	9.1 \pm 0.9	4
SDSS 1624+0029	T6 V	1.2425	1.9 \pm 0.4	1.2513	5.1 \pm 0.7	5
Gliese 229B	T6.5 V	1.2410	1.3 \pm 0.6	1.2520	4.3 \pm 0.5	6

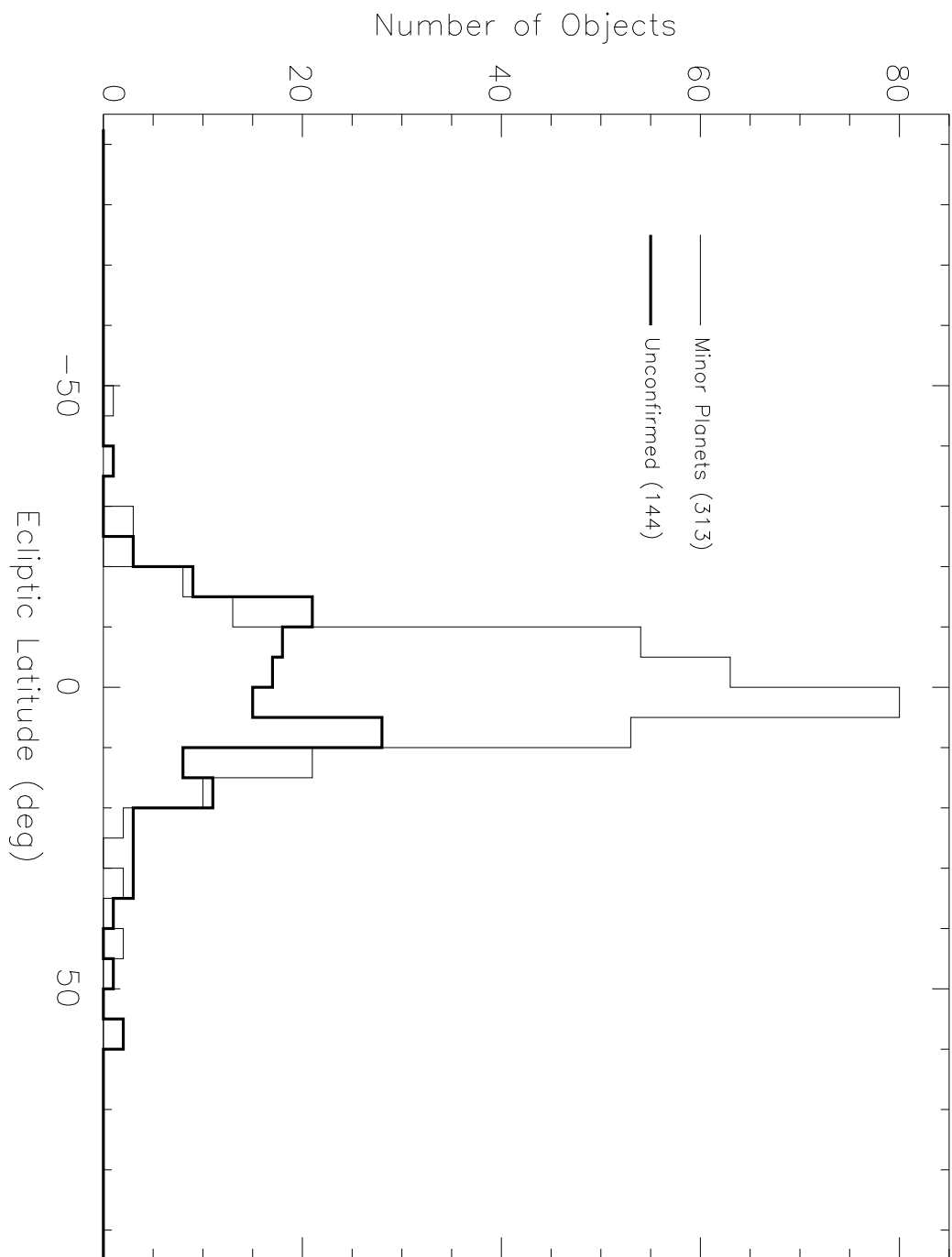
References. — (1) Leggett et al. (2001); (2) Reid et al. (2001); (3) Leggett et al. (2000); (4) Tsvetanov et al. (2000); (5) Strauss et al. 1999; (6) Geballe et al. (1996).

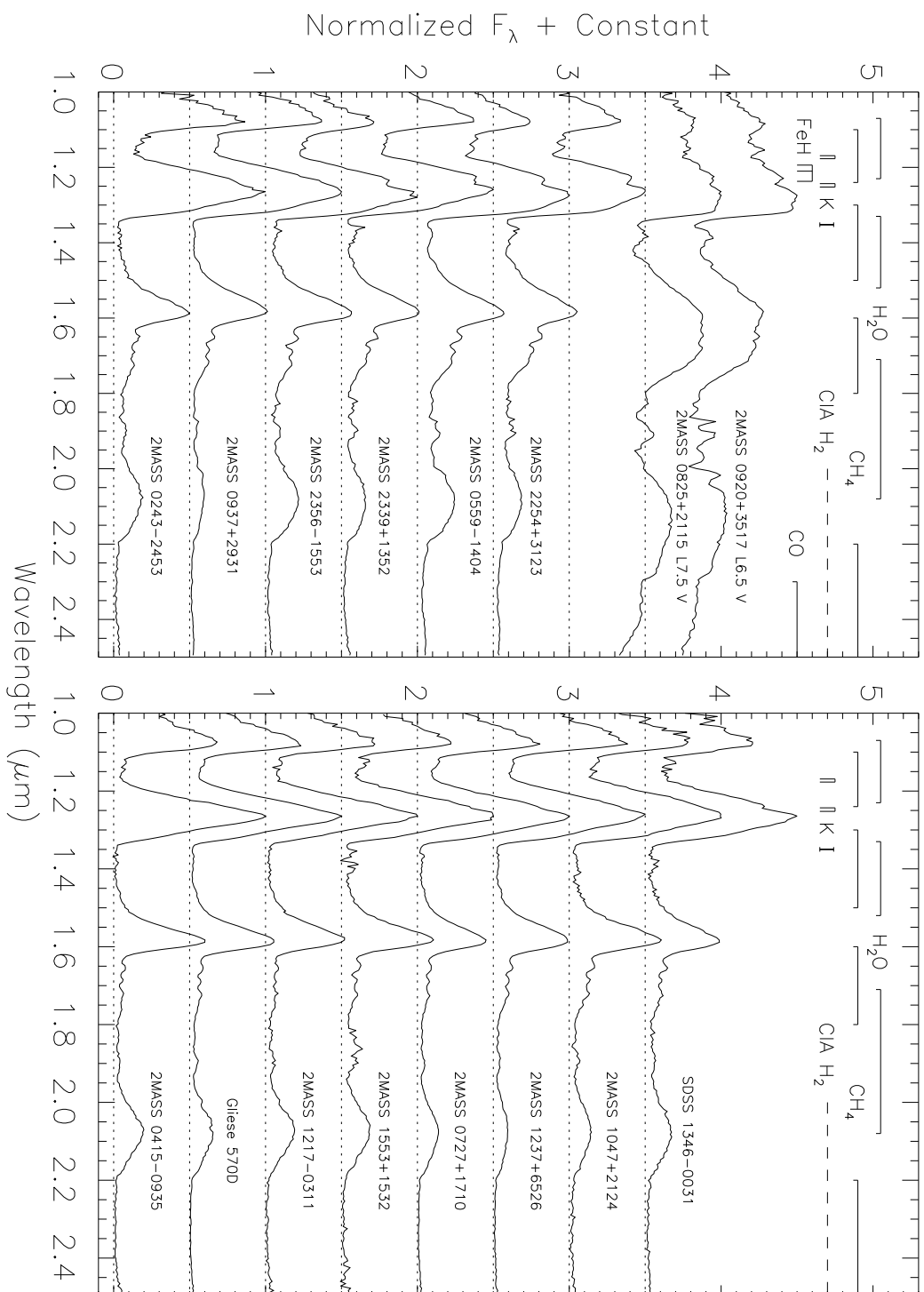
Table 14. Average 2MASS Colors for T dwarfs

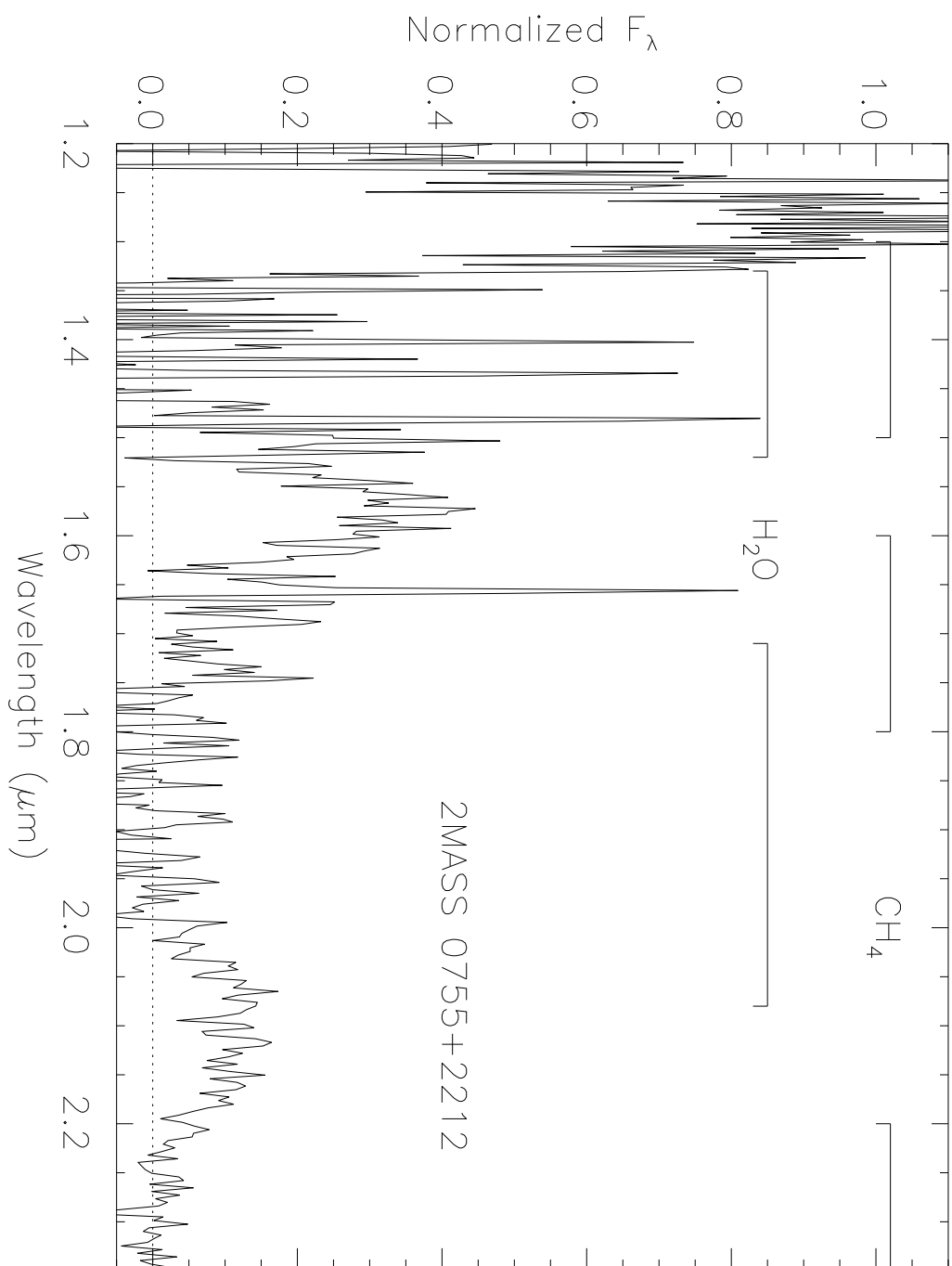
Type (1)	$\langle 2\text{MASS J-H} \rangle$ (2)	n ^a (3)	$\langle 2\text{MASS H-K}_s \rangle$ (4)	n ^a (5)	$\langle 2\text{MASS J-K}_s \rangle$ (6)	n ^a (7)
T2 V	0.84±0.06	1	0.22±0.07	1	1.05±0.07	1
T3 V	0.93±0.15	1	0.23±0.21	1	1.16±0.21	1
T5 V	0.17±0.04	2	0.09±0.06	2	0.25±0.05	2
T5.5 V	0.05±0.07	3	0.05±0.11	3	0.08±0.09	3
T6 V	0.07±0.05	6	−0.19±0.10	4	−0.03±0.09	4
T6.5 V	0.14±0.11	2	...	0	...	0
T7 V	−0.18±0.13	2	0.33±0.19	2	0.15±0.15	2
T7.5 V	0.06±0.14	1	...	0	...	0
T8 V	0.09±0.08	2	0.05±0.15	2	0.14±0.13	2

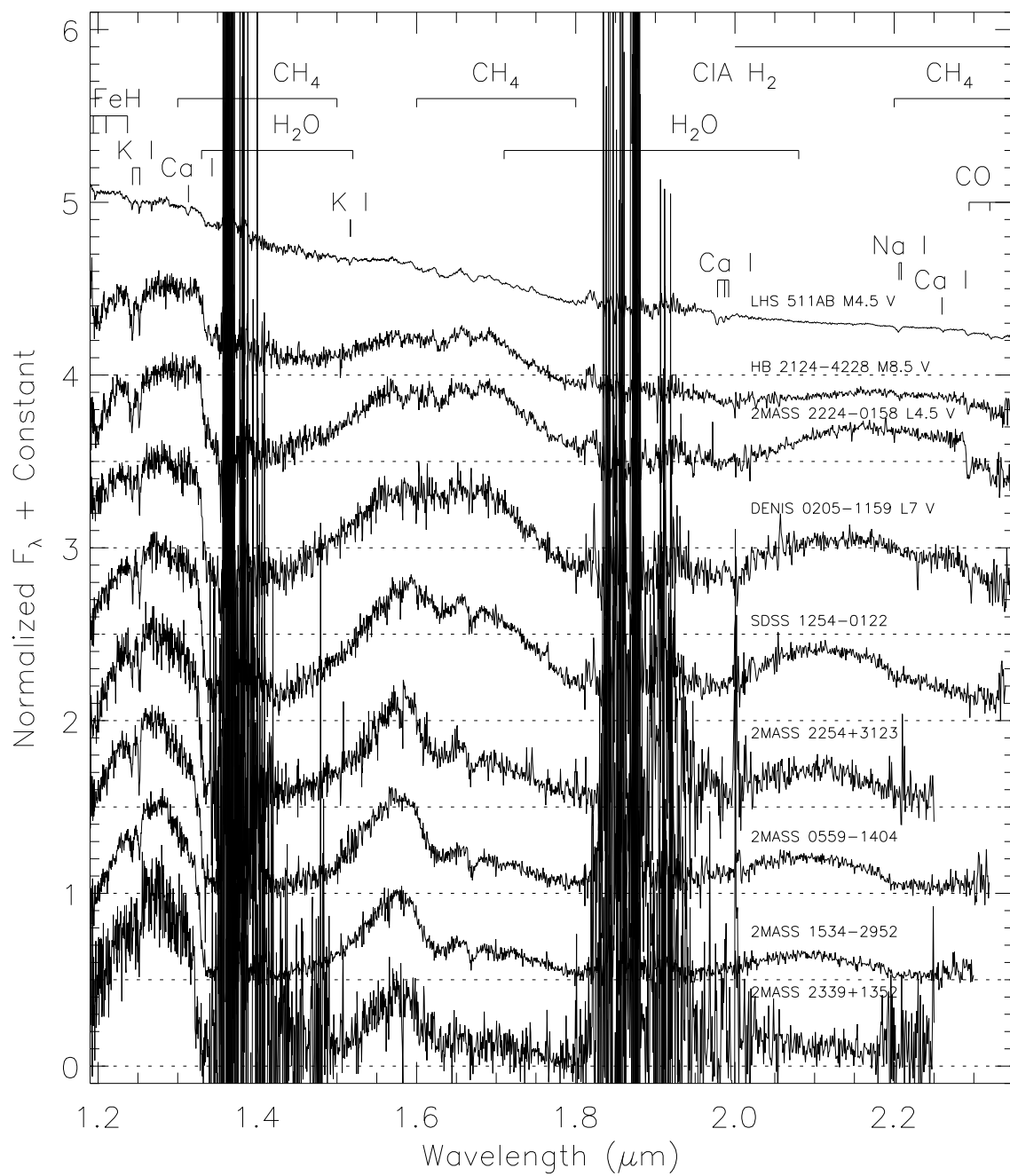
^aNumber of objects used in average.

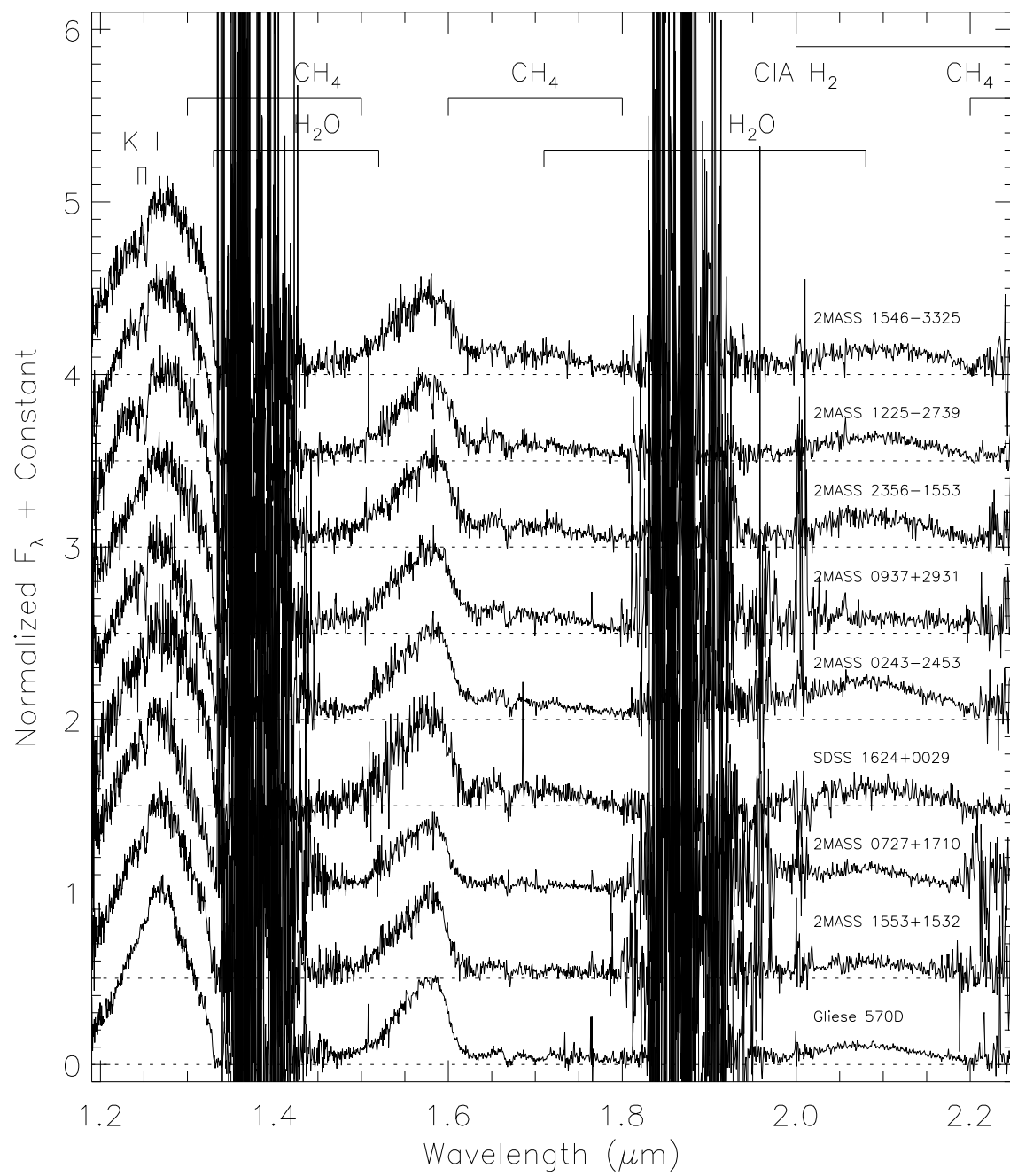


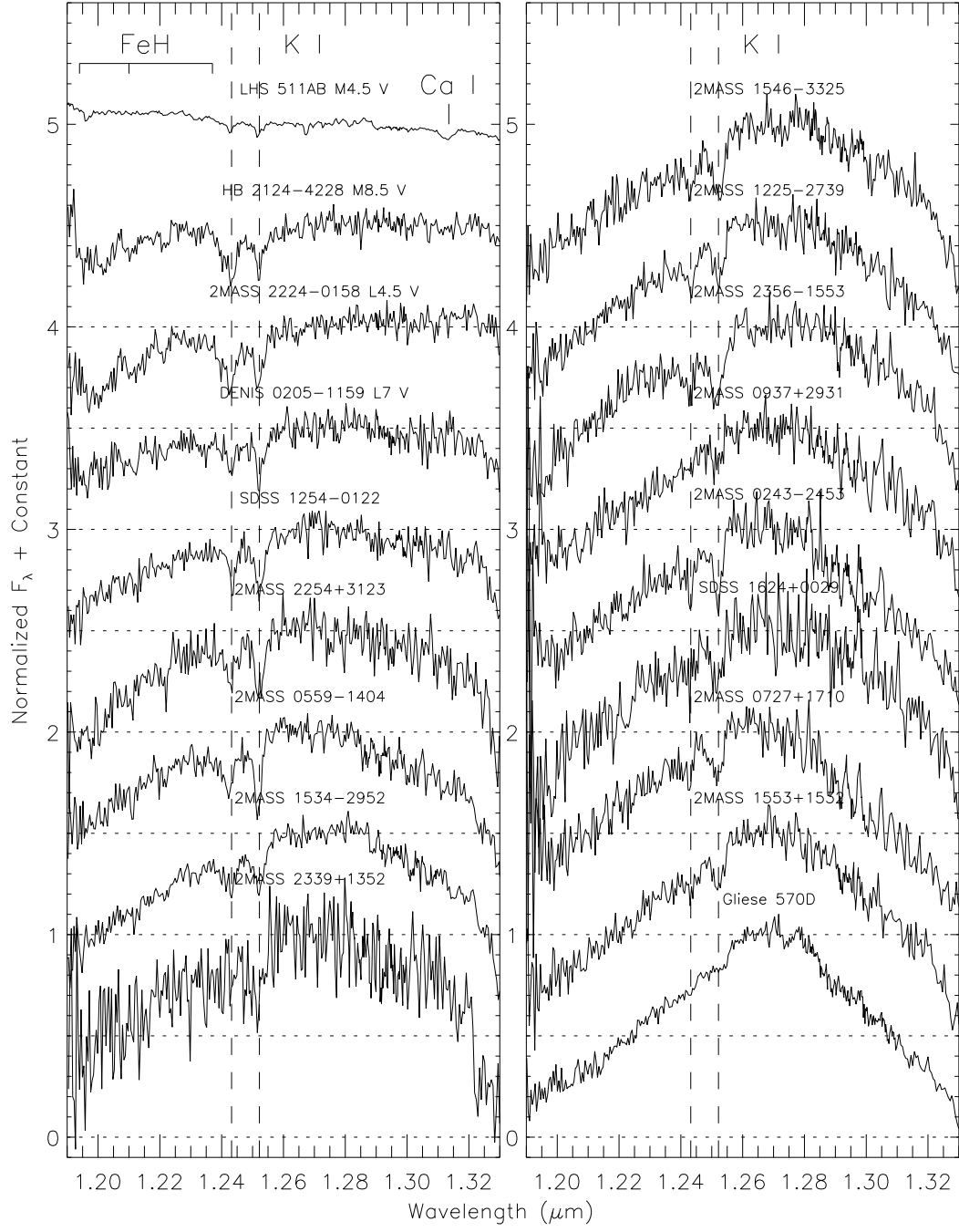


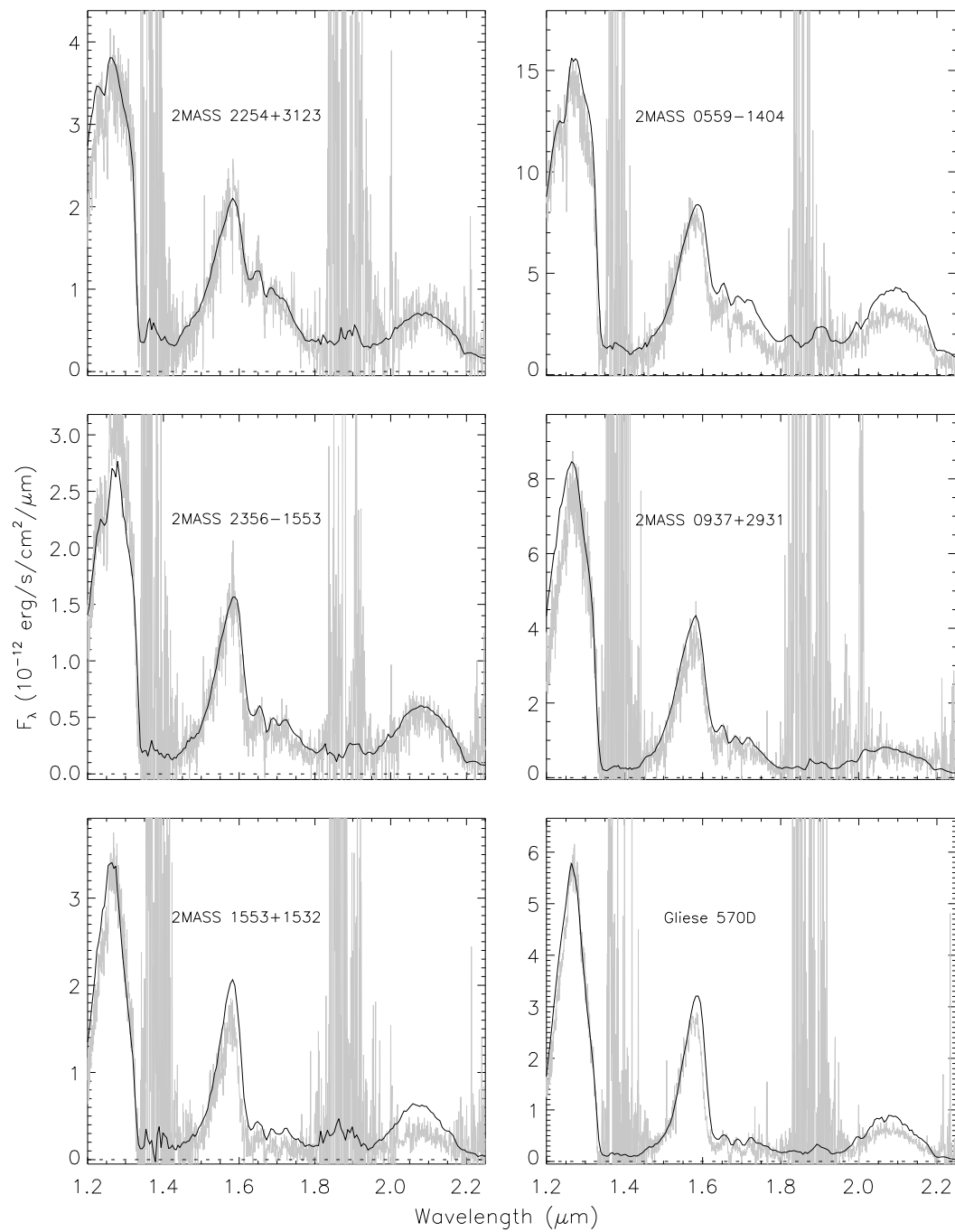


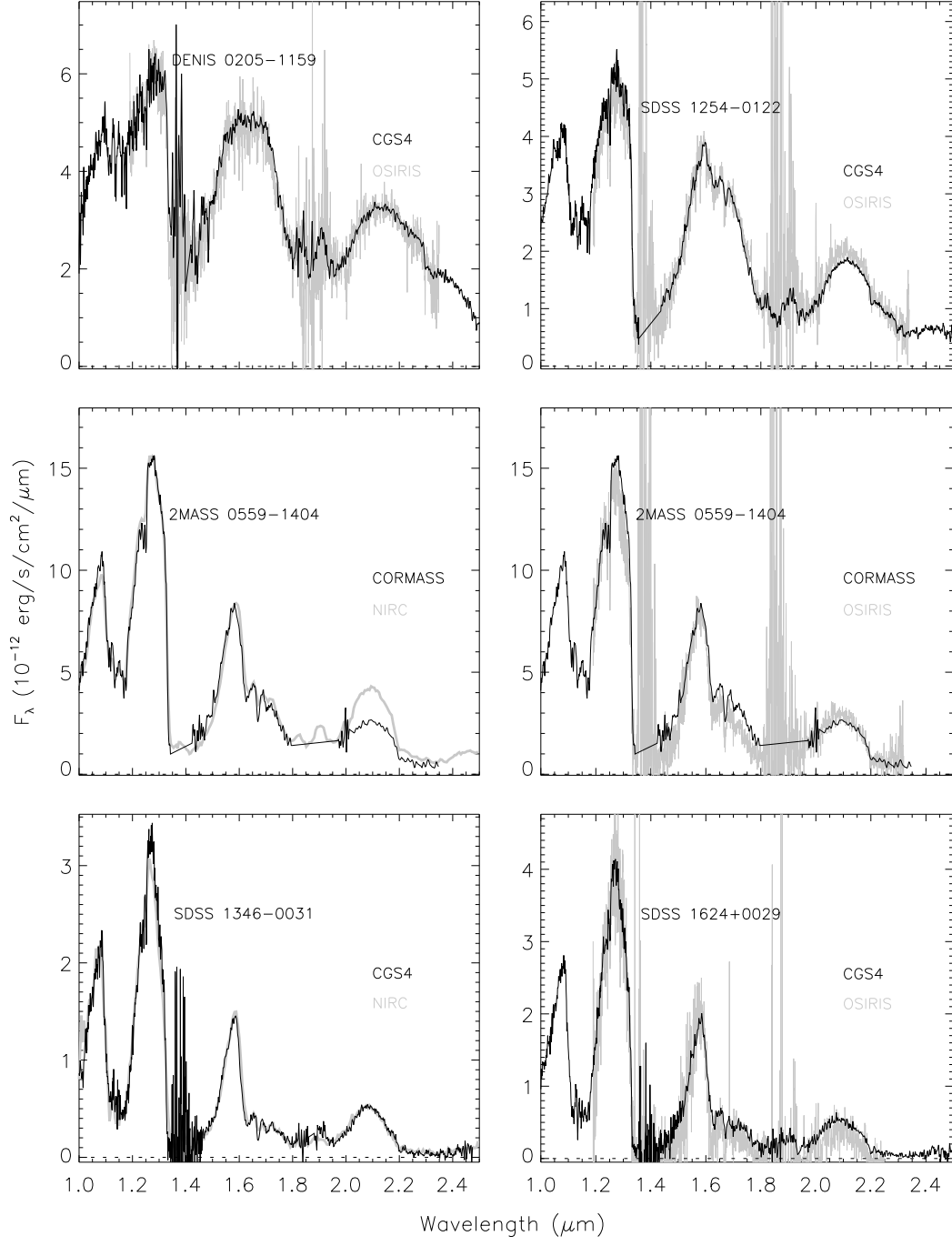


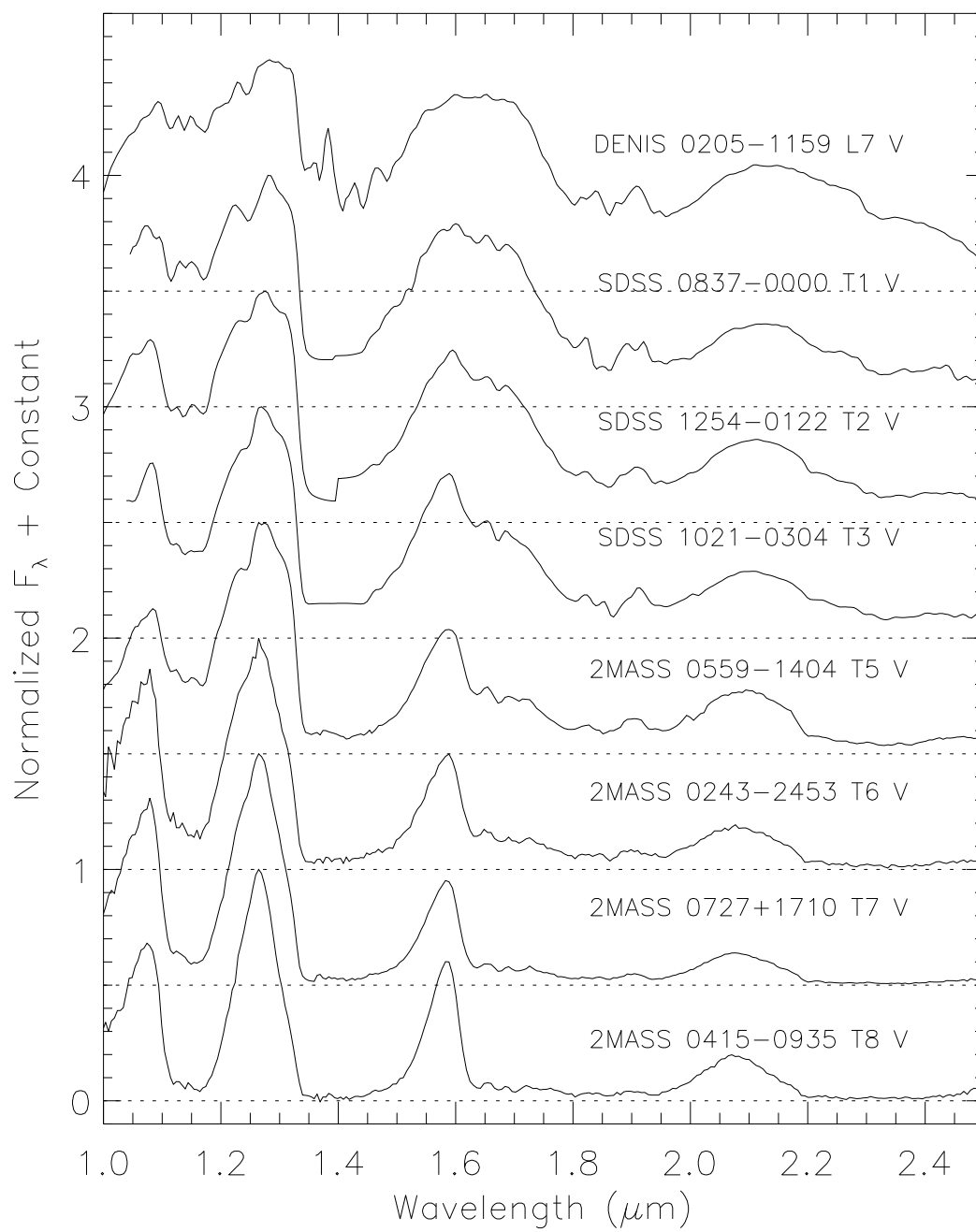


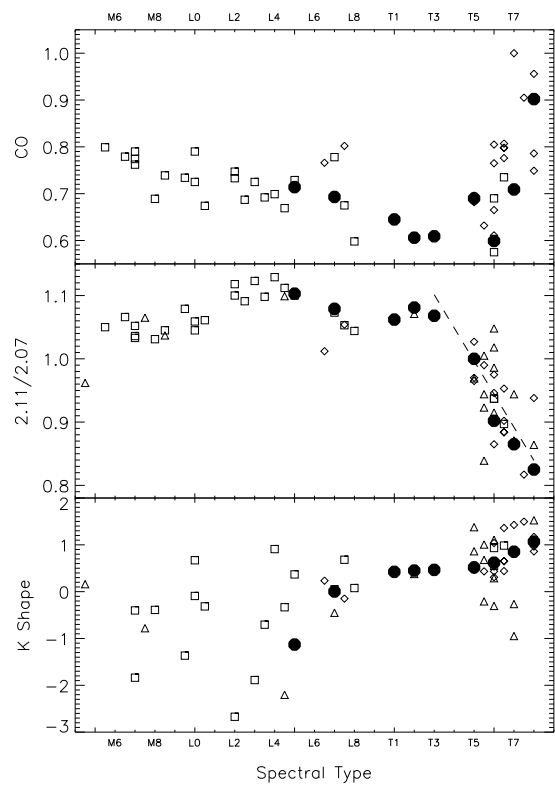
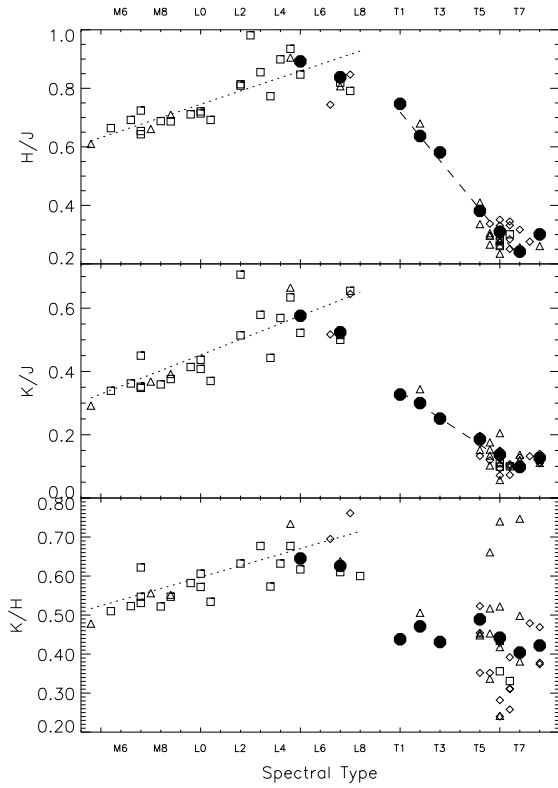
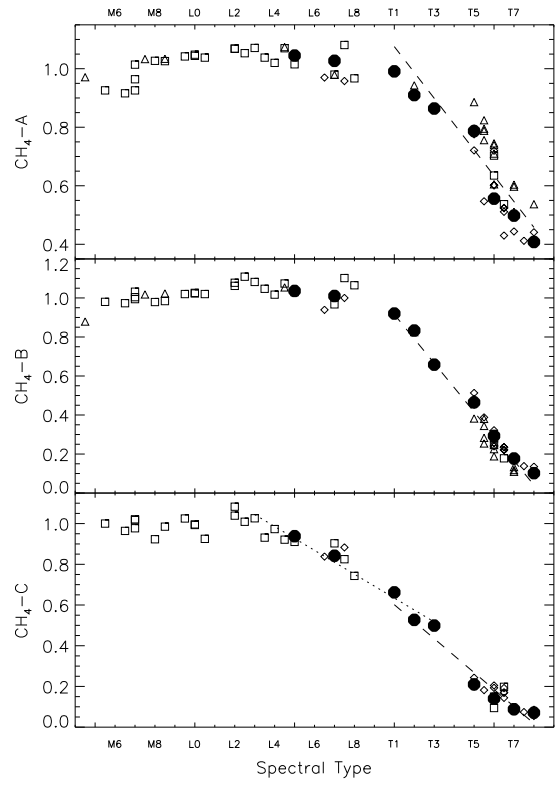
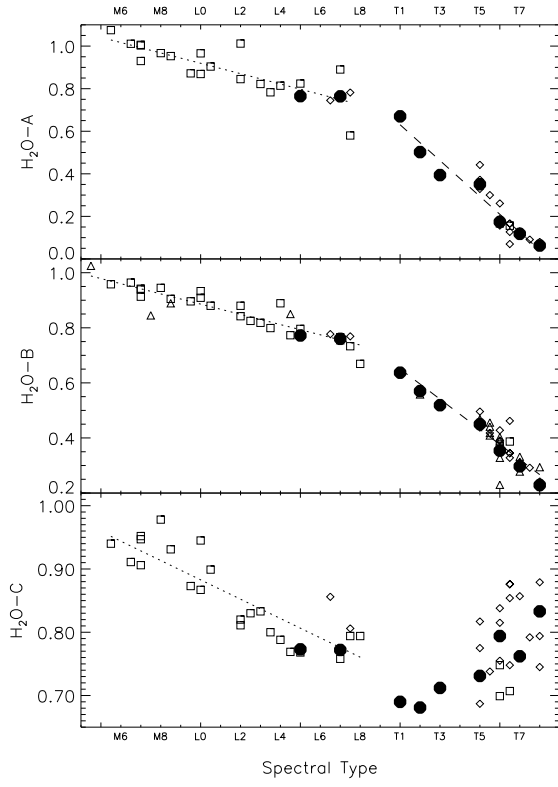


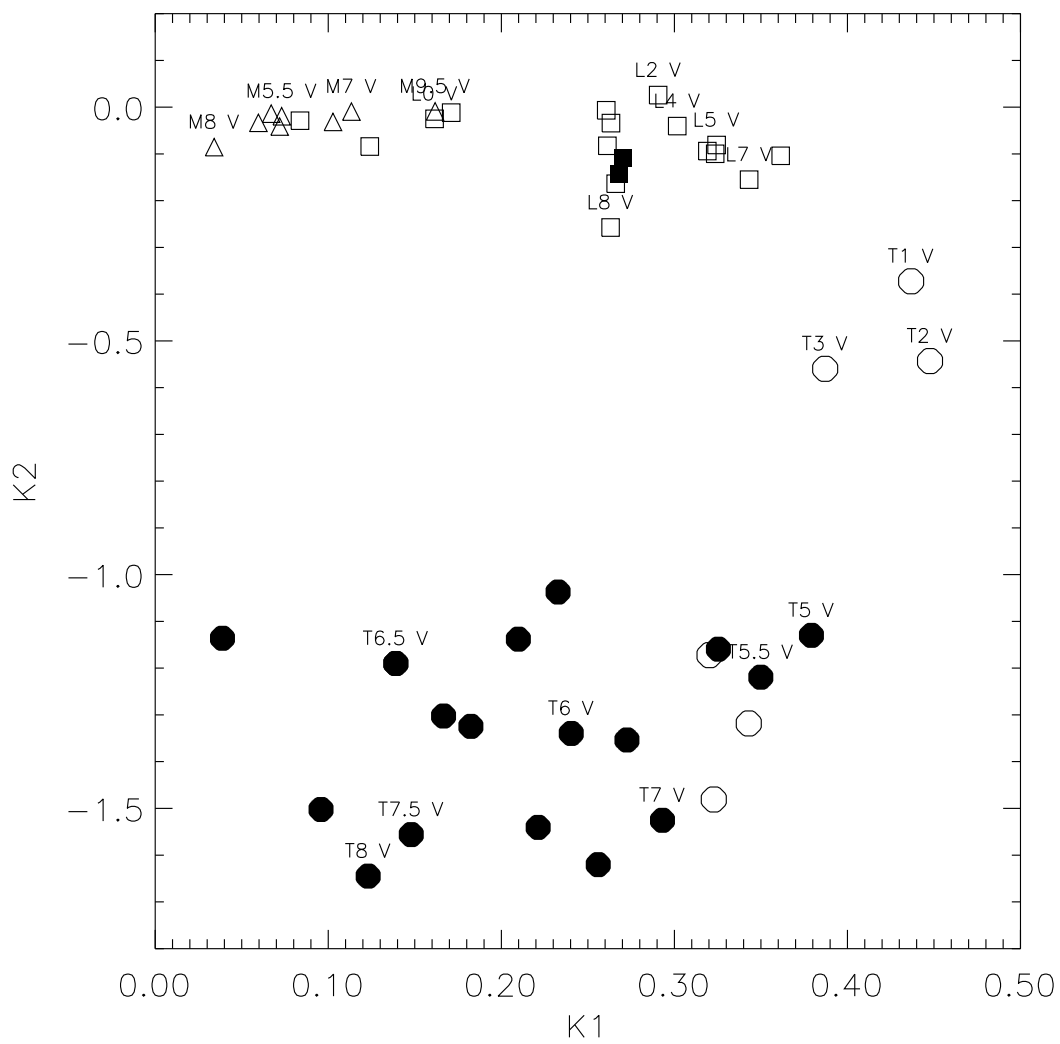


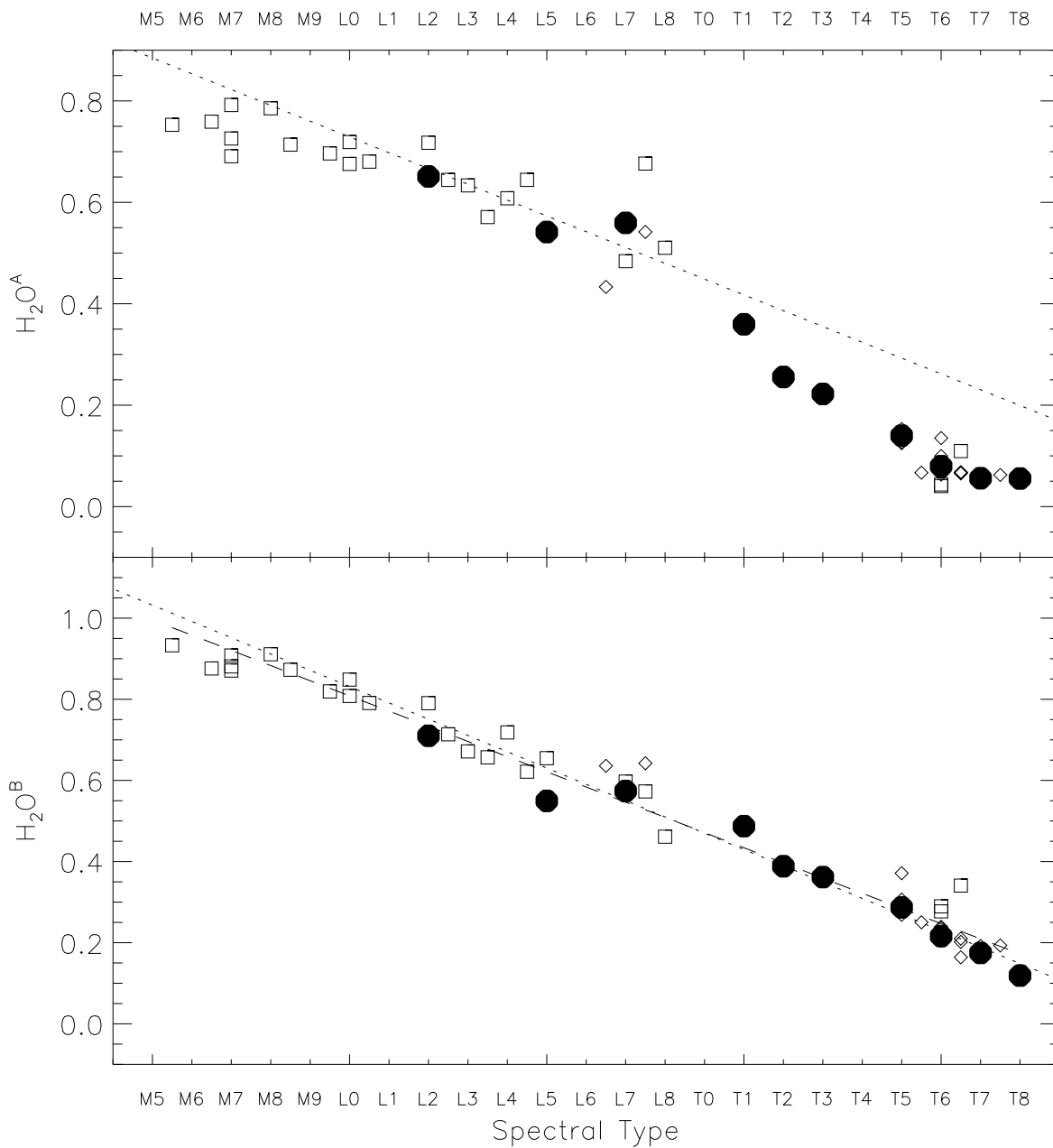


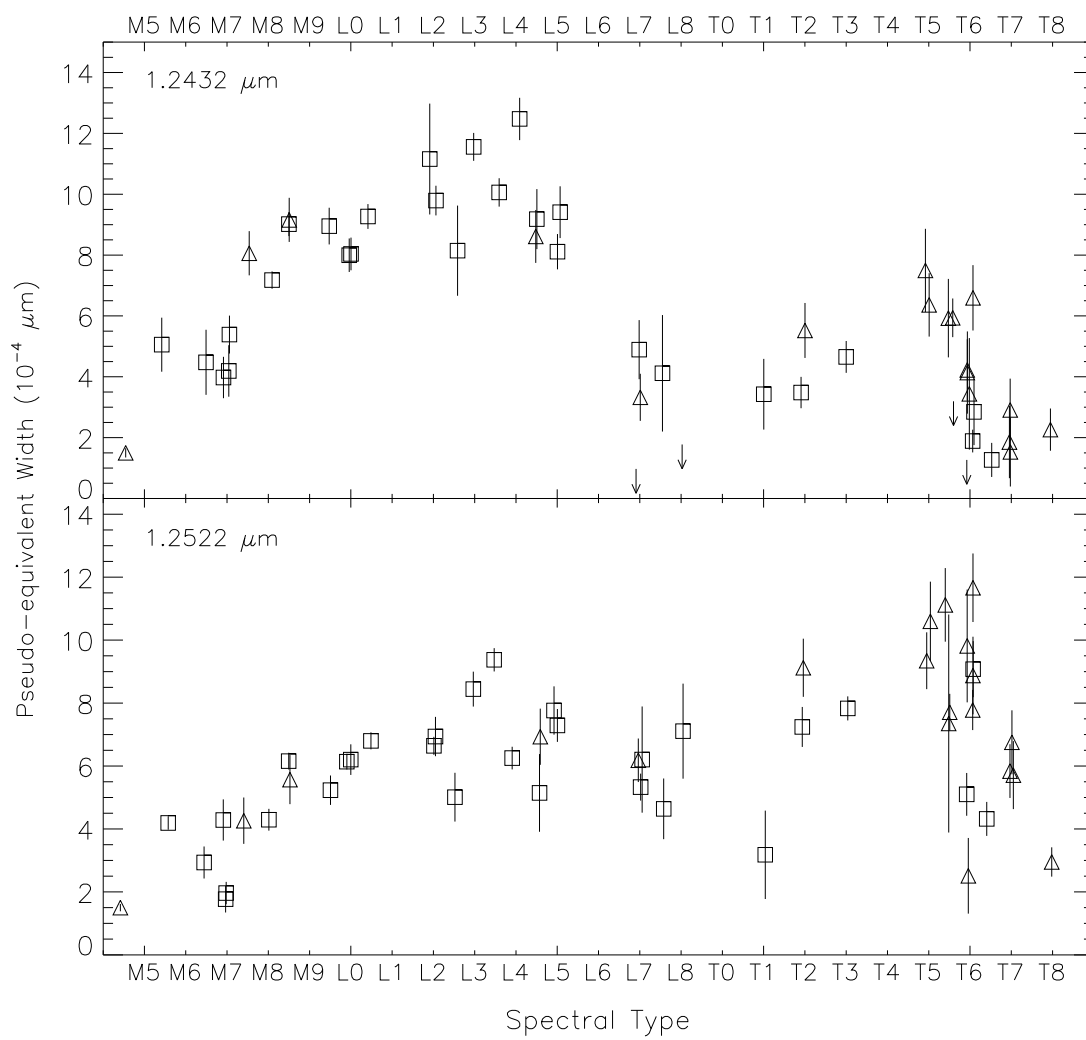


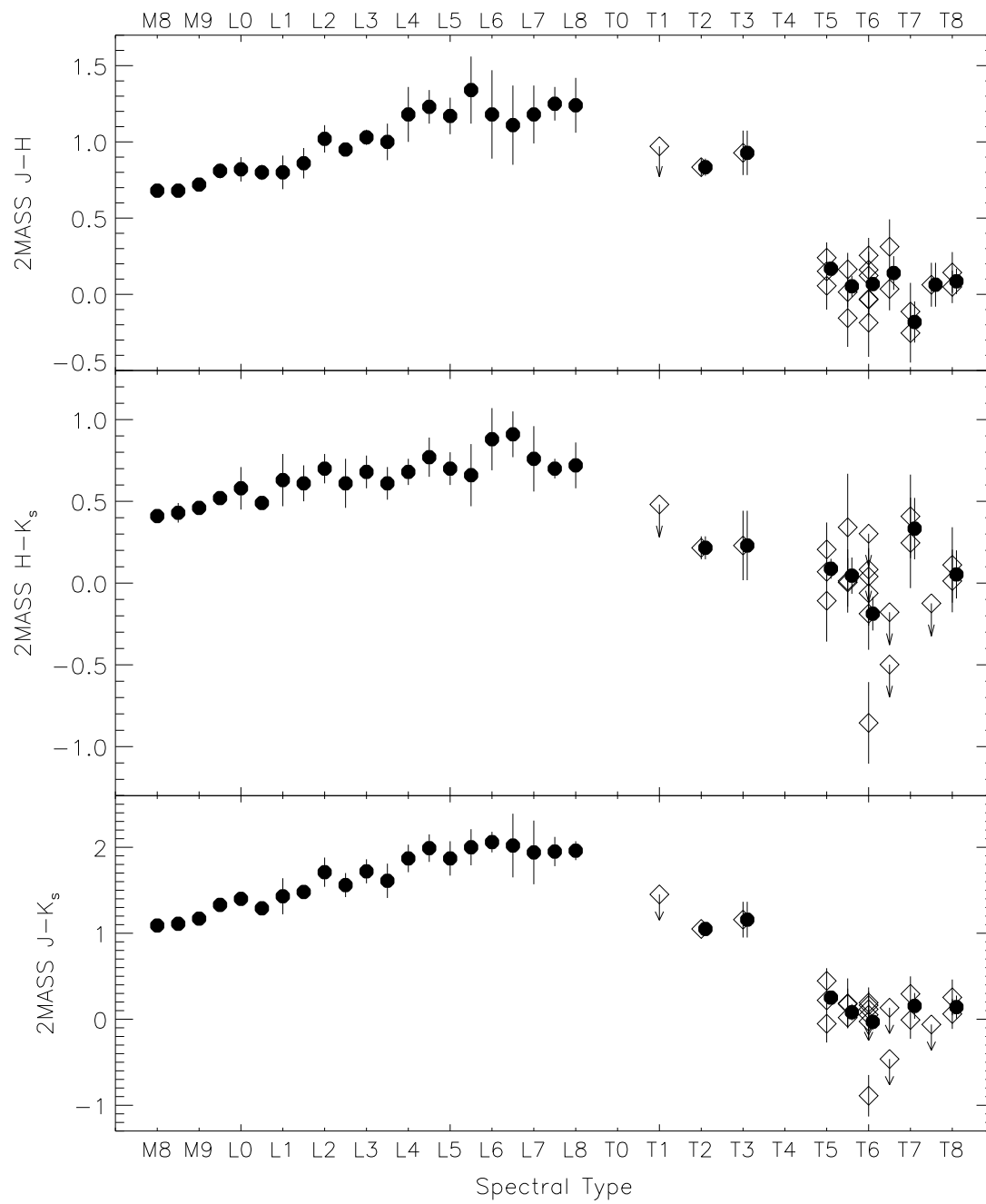


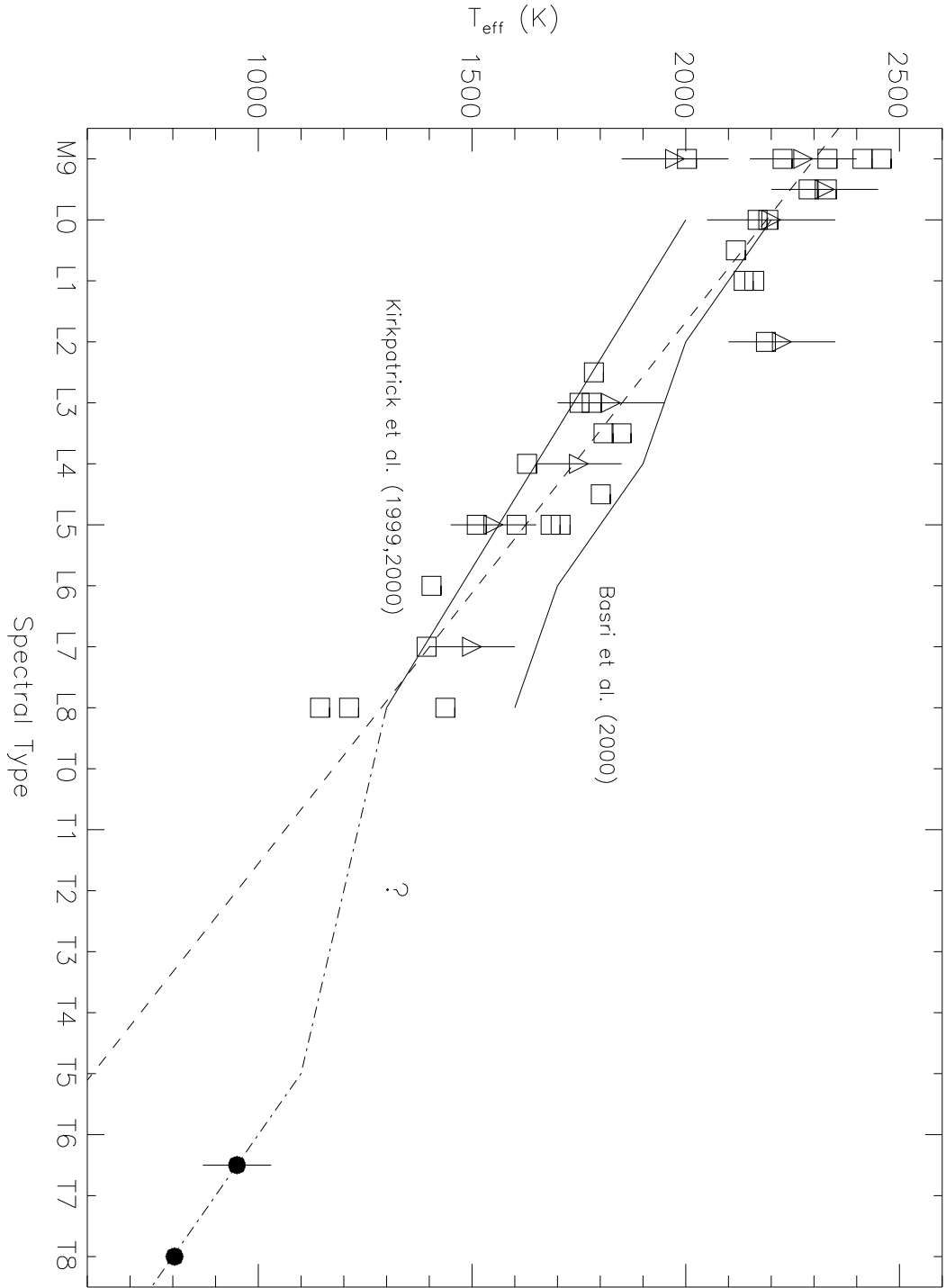


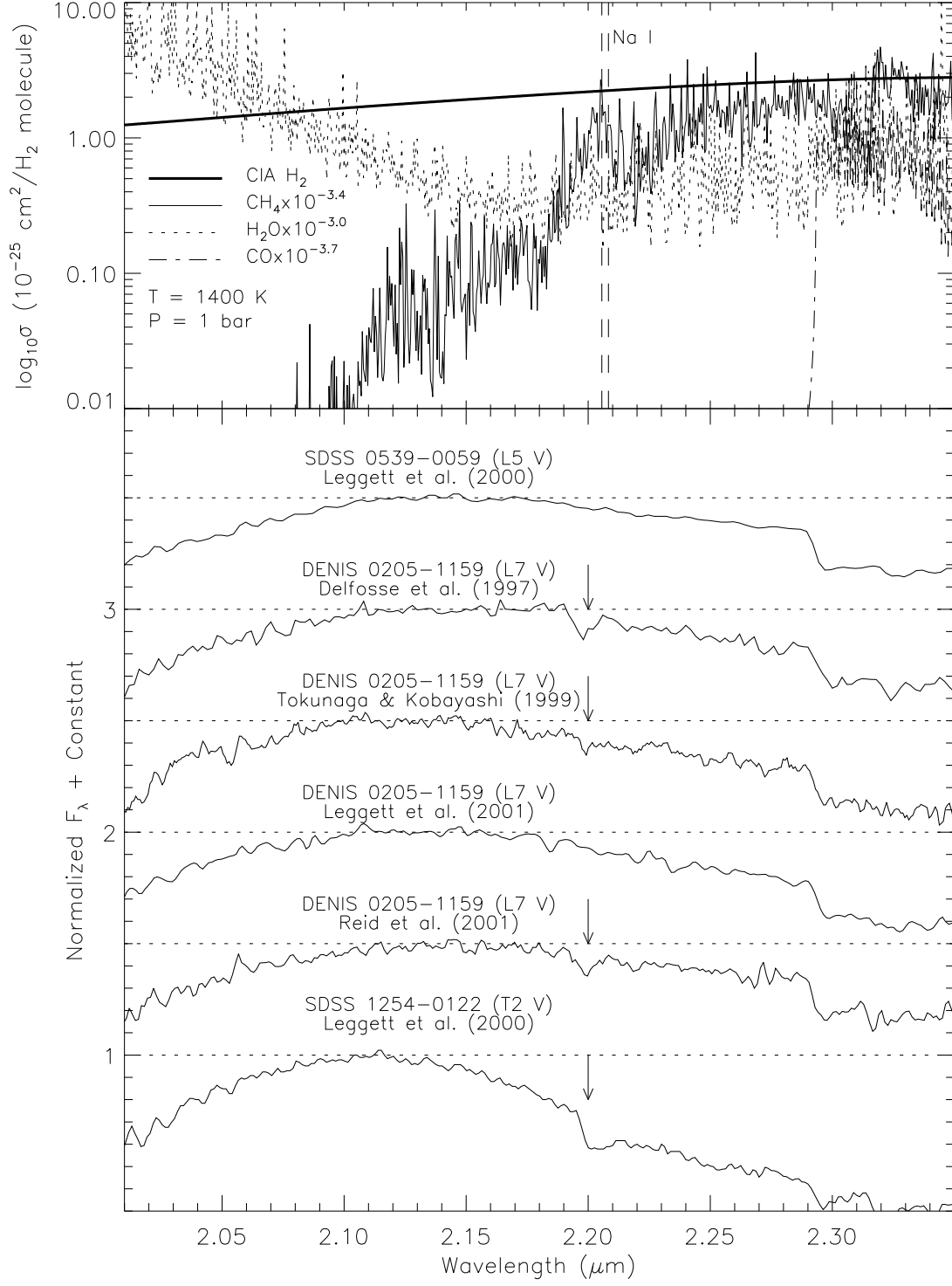


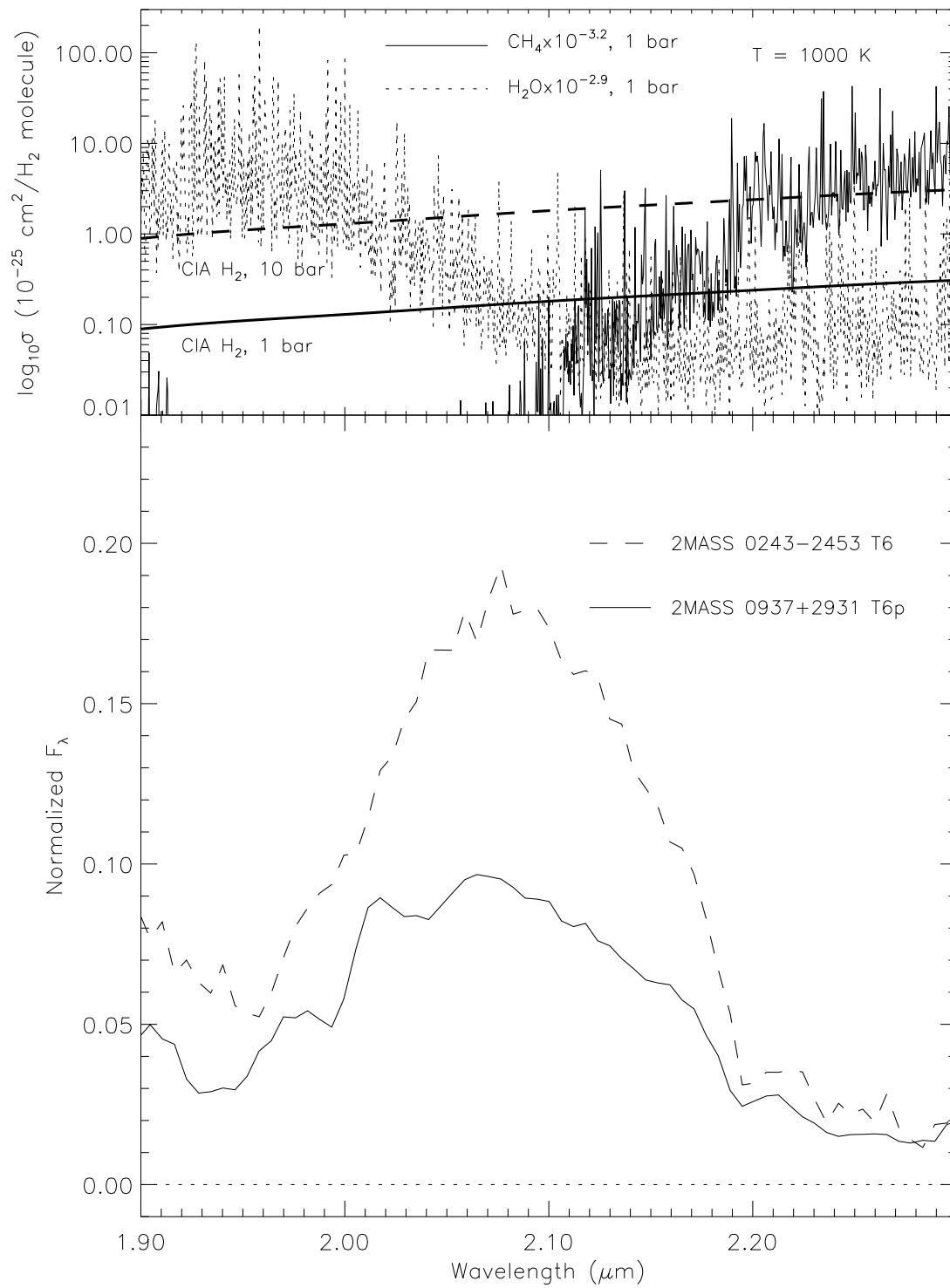












This figure "f2.jpg" is available in "jpg" format from:

<http://arxiv.org/ps/astro-ph/0108452v1>

This figure "f10a.jpg" is available in "jpg" format from:

<http://arxiv.org/ps/astro-ph/0108452v1>

This figure "f10b.jpg" is available in "jpg" format from:

<http://arxiv.org/ps/astro-ph/0108452v1>

This figure "f10c.jpg" is available in "jpg" format from:

<http://arxiv.org/ps/astro-ph/0108452v1>

This figure "f10d.jpg" is available in "jpg" format from:

<http://arxiv.org/ps/astro-ph/0108452v1>